Final Report

Development of FDOT SERF and RETA Design Equations for Coastal Scour When a Single Vertical Pile is Subjected to Wave Attack

FDOT Contract No. BDV34-977-12

Submitted To:

Project Manager, Tim Holley, P.E.
Florida Department of Transportation

Submitted By:

Principal Investigator, Raphael Crowley, Ph.D., P.E.
Research Assistants, Ian Gstalder, Matthew Davies, Dillon Sypula
University of North Florida
Taylor Engineering Research Institute
School of Engineering
Building 4, Room 1501
Jacksonville, FL 32224

August 2021

DISCLAIMER

APPROXIMATE CONVERSIONS TO SI UNITS

SYMBOL	**WHEN YOU KNOW**	**MULTIPLY BY**	**TO FIND**	**SYMBOL**
LENGTH				
in	inches	25.4	millimeters	mm
ft	feet	0.305	meters	m
yd	yards	0.914	meters	m
mi	miles	1.61	kilometers	km
SYMBOL	**WHEN YOU KNOW**	**MULTIPLY BY**	**TO FIND**	**SYMBOL**
AREA				
in^2	square inches	645.2	square millimeters	mm^2
ft^2	square feet	0.093	square meters	m^2
yd^2	square yard	0.836	square meters	m^2
ac	acres	0.405	hectares	ha
mi^2	square miles	2.59	square kilometers	km^2
SYMBOL	**WHEN YOU KNOW**	**MULTIPLY BY**	**TO FIND**	**SYMBOL**
VOLUME				
fl oz	fluid ounces	29.57	milliliters	mL
gal	gallons	3.785	liters	L
ft^3	cubic feet	0.028	cubic meters	m^3
yd^3	cubic yards	0.765	cubic meters	m^3
NOTE: volumes greater than 1000 L shall be shown in m^3				
SYMBOL	**WHEN YOU KNOW**	**MULTIPLY BY**	**TO FIND**	**SYMBOL**
MASS				
oz	ounces	28.35	grams	g
lb	pounds	0.454	kilograms	kg
T	short tons (2000 lb)	0.907	megagrams (or "metric ton")	Mg (or "t")
SYMBOL	**WHEN YOU KNOW**	**MULTIPLY BY**	**TO FIND**	**SYMBOL**
TEMPERATURE (exact degrees)				
°F	Fahrenheit	5 (F-32)/9 or (F-32)/1.8	Celsius	°C
SYMBOL	**WHEN YOU KNOW**	**MULTIPLY BY**	**TO FIND**	**SYMBOL**
ILLUMINATION				
fc	foot-candles	10.76	lux	lx
fl	foot-Lamberts	3.426	candela/m^2	cd/m^2
SYMBOL	**WHEN YOU KNOW**	**MULTIPLY BY**	**TO FIND**	**SYMBOL**
FORCE and PRESSURE or STRESS				
lbf	pound force	4.45	newtons	N
lbf/in^2	pound force per square inch	6.89	kilopascals	kPa

APPROXIMATE CONVERSIONS TO ENGLISH UNITS

SYMBOL	WHEN YOU KNOW	MULTIPLY BY	TO FIND	SYMBOL
LENGTH				
mm	millimeters	0.039	inches	in
m	meters	3.28	feet	ft
m	meters	1.09	yards	yd
km	kilometers	0.621	miles	mi
SYMBOL	**WHEN YOU KNOW**	**MULTIPLY BY**	**TO FIND**	**SYMBOL**
AREA				
mm^2	square millimeters	0.0016	square inches	in^2
m^2	square meters	10.764	square feet	ft^2
m^2	square meters	1.195	square yards	yd^2
ha	hectares	2.47	acres	ac
km^2	square kilometers	0.386	square miles	mi^2
SYMBOL	**WHEN YOU KNOW**	**MULTIPLY BY**	**TO FIND**	**SYMBOL**
VOLUME				
mL	milliliters	0.034	fluid ounces	fl oz
L	liters	0.264	gallons	gal
m^3	cubic meters	35.314	cubic feet	ft^3
m^3	cubic meters	1.307	cubic yards	yd^3
SYMBOL	**WHEN YOU KNOW**	**MULTIPLY BY**	**TO FIND**	**SYMBOL**
MASS				
g	grams	0.035	ounces	oz
kg	kilograms	2.202	pounds	lb
Mg (or "t")	megagrams (or "metric ton")	1.103	short tons (2000 lb)	T
SYMBOL	**WHEN YOU KNOW**	**MULTIPLY BY**	**TO FIND**	**SYMBOL**
TEMPERATURE (exact degrees)				
^{o}C	Celsius	1.8C+32	Fahrenheit	^{o}F
SYMBOL	**WHEN YOU KNOW**	**MULTIPLY BY**	**TO FIND**	**SYMBOL**
ILLUMINATION				
lx	lux	0.0929	foot-candles	fc
cd/m^2	candela/m^2	0.2919	foot-Lamberts	fl
SYMBOL	**WHEN YOU KNOW**	**MULTIPLY BY**	**TO FIND**	**SYMBOL**
FORCE and PRESSURE or STRESS				
N	newtons	0.225	pound force	lbf
kPa	kilopascals	0.145	pound force per square inch	lbf/in^2

*SI is the symbol for the International System of Units. Appropriate rounding should be made to comply with Section 4 of ASTM E380. (Revised March 2003)

TECHNICAL REPORT DOCUMENTATION

1. Report No.	2. Government Accession No.	3. Recipient's Catalog No.	
4. Title and Subtitle Development of FDOT SERF and RETA Design Equations for Coastal Scour When a Single Vertical Pile is Subjected to Wave Attack		5. Report Date August 2021	
		6. Performing Organization Code	
7. Author(s) R.W. Crowley		8. Performing Organization Report No.	
9. Performing Organization Name and Address University of North Florida Taylor Engineering Research Institute Building 4, Room 150 Jacksonville, FL 32224		10. Work Unit No.	
		11. Contract or Grant No. BDV34-977-12	
12. Sponsoring Agency Name and Address Florida Department of Transportation 605 Suwannee Street, MS 30 Tallahassee, FL 32399		13. Type of Report and Period Covered Draft Final Report, May 2019-March 2021	
		14. Sponsoring Agency Code	
15. Supplementary Notes			
16. Abstract Computational fluid dynamic (CFD) modeling was used to simulate several piles under water wave attack. First, the CFD models were tested at small scale using meshes that were functions of wave geometry (i.e., wave height, wavelength, wave period) to verify that the models could accurately reproduce previously reported experimental data. Once verified, the models were scaled up to typical field scales using the same relative mesh parameters. Maximum bed stress data near the piles were recorded, and a relatively simple parametric model was fit to these data that reproduced modeled results with reasonable accuracy. In addition, a more sophisticated parametric model was developed that reproduced results almost perfectly. This parametric model allows one to use FDOT's erosion rate testing instruments – the Sediment Erosion Rate Flume (SERF) and the Rotating Erosion Testing Apparatus (RETA) – for wave scour design for the single vertical pile design situation.			
17. Keywords. Wave Scour; Coastal Erosion		18. Distribution Statement No restrictions	
19. Security Classif. (of this report) Unclassified	20. Security Classif. (of this page) Unclassified	21. Pages 86	22. Price

EXECUTIVE SUMMARY

The current Florida Department of Transportation (FDOT) method for estimating maximum scour depth around bridge foundations is considered the state-of-the-art when designing for steady flow sand scour. However, it is unclear how to utilize this method when bridge foundations are subjected to wave action, and the FDOT scour design method is only applicable to non-cohesive (i.e., sandy) bed materials. Over the past several years, the FDOT has devoted significant resources toward developing a scour design method for all bed materials, including cohesive sediments and rock. The FDOT's Sediment Erosion Rate Flume (SERF) and Rotating Erosion Testing Apparatus (RETA) both may be used to develop cost-effective scour design solutions for cohesive sediments under steady flow conditions. Solutions from the SERF and RETA tend to be more accurate than applying the steady flow sand scour equations to cohesive materials because the SERF and RETA method take sediment conditions into account. The goal of this project was to begin a framework for utilizing the SERF and RETA under coastal scour conditions.

The result of any series of SERF or RETA tests are called "erosion functions," which are relationships between sediment erodibility and water-induced shear stress. Once erosion functions are computed for a given bed material, a conservative hydrograph is developed to simulate water flow over a bridge's lifespan. Then, the maximum near-foundation bed stress associated with each flow condition is computed. For steady flows, this conversion from flow velocity to bed stress is relatively straightforward. When bridge foundations are subjected to wave action, it is much less clear how one computes design bed stress. This project was designed to fill this knowledge gap.

During this project, several simulations of piles under wave attack were conducted using computational fluid dynamics (CFD). First, small-scale models were run using mesh parameters relative to wave parameters and pile geometry to verify that CFD could accurately reproduce previously reported experimental data. Once this was verified, models were upscaled to typical field scales using the same relative mesh parameters. Maximum near-pile shear stress data were recorded for each model run. Finally, a relatively simple parametric model that is a function of wave parameters and structural geometry was fit to these data. While this model reproduced CFD data with reasonable accuracy, results were somewhat skewed at lower stresses and inaccurate for higher stresses. A more sophisticated model was then developed, and this new model reproduces CFD data almost perfectly. This model may be used as a design tool for the single pile under wave attack condition. While it is likely incorrect to use this parametric model for more complex bridge geometries, it is likely that this model could be expanded in the future to account for typical complex bridge pier structures such as pile caps and pile clusters.

TABLE OF CONTENTS

Page

CHAPTER

LIST OF TABLES

LIST OF FIGURES

CHAPTER 1
INTRODUCTION

1.1 Background Statement

When Hydraulic Engineering Circular No. 18 (Arneson et al., 2012), the national design guideline for bridge scour, was developed in the early 1990s, it instructed design engineers to assume that all bed materials – i.e., sands, cohesive sediments, and rock – erode to the same depth over a structure's lifespan based upon free-stream velocity and to use the maximum sand scour depth as the design criterion for bridge foundations. Maximum equilibrium local sand scour depth equations based upon free-stream velocity were developed over several years by both Colorado State University, called the "CSU Equations," (Arneson et al., 2012) and the Florida Department of Transportation (FDOT), called the "FDOT Method" (FDOT, 2005). Both methods are similar in the sense that they use empirical data fitting to estimate equilibrium scour depth based upon several dimensionless parameters.

The FDOT Method has provided more accurate predictions historically, partly because it takes the ratio between structure size and grain size into account. Several FDOT-funded studies showed that this method was a critical component associated with accurately computing equilibrium scour depth (Sheppard, 2004; Sheppard and Miller, 2006; Sheppard et al., 2004). The FDOT Method yields conservative predicted equilibrium scour depths when steady flow causes scour in non-cohesive sediments. However, there are two issues with both the FDOT and CSU methods. First, neither the FDOT Method nor the CSU Equations take cohesion into account when computing scour depth. As such, both methods may produce overly conservative designs when bridges are founded on rock or cohesive sediments. Secondly, these methods are for steady flow only. Neither will produce accurate design information in a coastal environment where wave action causes scour.

1.1.1 Predicting Scour Depth Using Erosion Functions

In response to the cohesion issue, the FDOT sponsored much research associated with testing bed materials' erosion rates. From the late 1990s through 2013, FDOT funded several projects involving development of and testing with two erosion rate testing devices – the Sediment Erosion Rate Flume (SERF) and the Rotating Erosion Testing Apparatus (RETA). Examples include Bloomquist and Crowley (2010); Bloomquist et al. (2012); Bloomquist et al. (2007); Crowley et al. (2012a); Crowley et al. (2012b); Crowley et al. (2012c); Crowley et al. (2014a). Because of the success of the RETA, the FDOT State Materials Office (SMO) in Gainesville, FL, built several of these devices and often uses them to test erosion rates of erodible rock and stiff sediment. Under steady flow conditions, results from the RETAs and SERF are often used to design for scour. This method, dubbed the SERF/RETA Method, is described as follows:

1. Using the SERF or the RETA, an erosion function – i.e., an erosion rate versus shear stress relationship – is developed for a given bed material.

2. Based upon field estimations and a conservative hydrograph, the bed shear stress in the field is estimated.

3. Using the relationships developed in (1), each shear stress from (2) is converted to an erosion rate for a specified length of time based upon each flow event. This results in total erosion for a given flow event.

4. The total erosion over the structure's lifespan is computed by adding the values from (3) for all erosion events.

The principal investigator, with FDOT support, spent several years perfecting testing with the SERF and the RETA by conducting a series of field tests and developing computational models of the devices that showed how to measure erosion functions correctly and conservatively. As a result of this work, it is believed that the mechanics associated with laboratory testing component of this scour prediction method is now well understood.

1.1.2 Predicting Scour Depth in a Coastal Environment

Over the years, the Fredsoe and Sumer research group at the Technical University of Denmark has developed predictive equations for equilibrium scour depth due to wave action in non-cohesive sediment (Sumer and Fredsoe, 1998; Sumer and Fredsoe, 2001; Sumer et al., 1990; Sumer et al., 1992). Like the FDOT Method and the CSU Equations for predicting non-cohesive scour under steady flow conditions, the method is based upon empirical results from laboratory testing. Results showed that under wave conditions, equilibrium scour depth is a function of Keuligan-Carpenter Number, *KC*:

$$KC = \frac{U_m T}{D} \tag{1-1}$$

where U_m is the maximum upstream flow velocity due to wave action at the bed; T is the wave period; and D is the structure (pile) width. Values for U_m may be converted to a more useful form via the following expression:

$$U_{fm} = \sqrt{\frac{f_w}{2}}\,U_m \tag{1-2}$$

where U_{fm} is the maximum friction velocity and f_w that is obtained by solving the following set of expressions numerically (Fredsoe, 1984):

$$\frac{dz}{d(\omega t)} = \frac{\beta \sin(\omega t)}{e^z(z-1)+1} - \frac{z(e^z-z-1)}{e^z(z-1)+1}\left(\frac{1}{U_o}\right)\left(\frac{dU_o}{d(\omega t)}\right) \tag{1-3}$$

$$\beta = 30\kappa^2\left(\frac{a}{k}\right) = \frac{30\kappa}{k}\left(\frac{U_m}{\omega}\right) \tag{1-4}$$

$$z = \frac{U_o}{U_{fm}}\kappa \tag{1-5}$$

in which k is the wave number; a is the free stream particle amplitude; ω is $\frac{2\pi}{T}$; κ is von Karmann's constant; and U_o is the velocity at the top of the boundary layer.

The nondimensional Shields (1936) parameter is often used to describe critical shear stress – the stress required for sediment incipient motion. It is defined as:

$$\Theta = \frac{U_{fm}^2}{(SG-1)gD_{50}} \tag{1-6}$$

where SG is the sediment's specific gravity; g is the acceleration due to gravity; and D_{50} is the mean sediment diameter. Nondimensionalized scour depth is given by the following expression:

$$\frac{y_s}{D} = 1.3\{1 - \exp[-0.03(KC - 6)]\} \tag{1-7}$$

Substituting Equations 1-1, 1-2, and 1-6 into Equation 1-7 yields:

$$\frac{y_s}{D} = 1.3\left\{1 - \exp\left[-0.03\left(T\frac{\sqrt{D_{50}}}{D}\sqrt{\frac{2(SG-1)g\Theta}{f_w}} - 6\right)\right]\right\} \tag{1-8}$$

It is interesting to note (and not yet published) that this substitution shows that scour is a function of the ratio between grain size and structure size. This supports FDOT's steady-flow scour equations and show why their results are more accurate than the CSU method.

Upon first glance, it would appear that Sumer and Fredsoe solved the wave scour problem. However, further examination shows that, more research is required due to two issues. First this method has only been validated in sand and has yet to be used with cohesive materials or rock. In addition, results show that as *KC* approaches infinity (i.e., current becomes steady), scour depth is always the same regardless of free-stream velocity (Figure 1-1). Based upon the FDOT Method and CSU Equations, this cannot be correct. As a first step at resolving this issue, Sumer et al. (2013) examined backfilling around piles in waves and current. However, no one has yet completely unified wave scour with steady flow equilibrium scour depth prediction. And, as stated, no one has yet effectively examined wave scour in cohesive sediments or rock. Solving the unification issue would be of little practical value. However, solving the wave scour in cohesive sediment and rock issue could lead to significant overdesign cost savings. In addition, it should be possible to adapt the erosion function scour prediction method to both the cohesive and non-cohesive scour cases

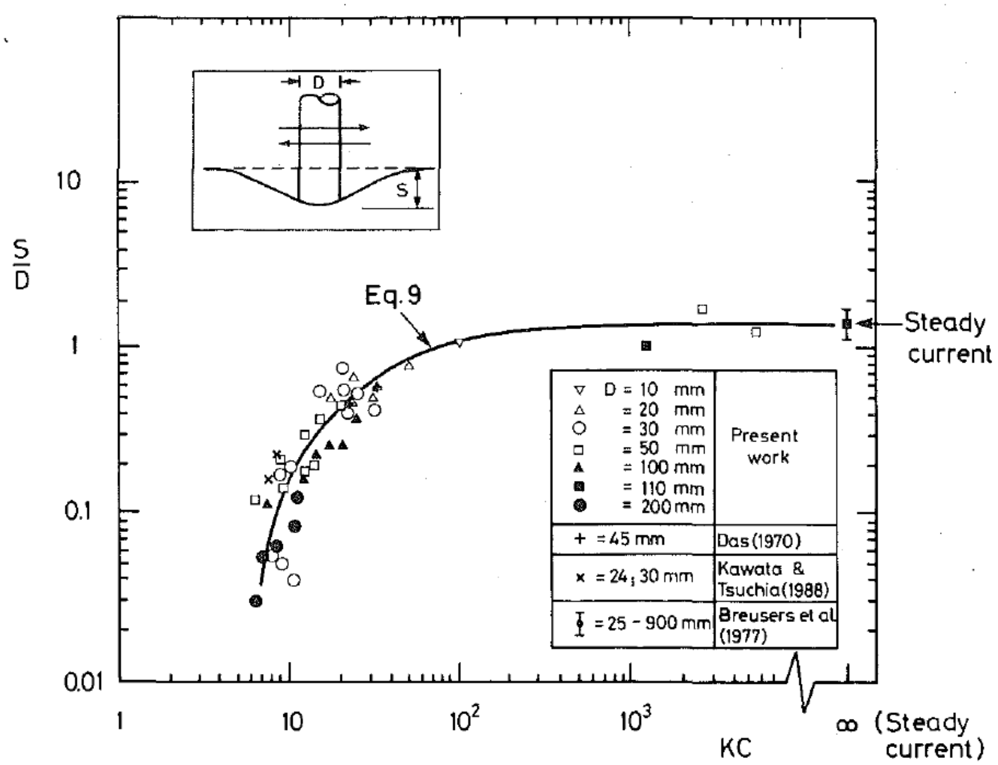

Figure 1-1. Nondimensionalized scour depth as a function of *KC* (adapted from Sumer et al., 1992); note that this figure is for scour due to wave action only

1.2 Goals and Objectives

The objective of the research proposed herein is to adapt the FDOT SERF/RETA method so that it may be used in a coastal environment. To do this, a better understanding of bottom stresses around piles and pile groups subjected to wave action was required. Put another way, the only step necessary for adapting the SERF/RETA method for use in a coastal environment was to better understand the third step from Section 1.1.1 – finding shear stresses in the field. This project focused on single-pile configurations. In the future, it should be possible to adjust results to account for more complex pier geometries.

Under steady flow conditions, two methods have been used to estimate bottom stress near a pile. The first method is relatively simple and involves coupling boundary layer theory with potential flow theory. From the late 1990s through 2010, the J-L. Briaud research group at Texas A&M University (TAMU) developed a more-sophisticated method that is much more accurate. This method is discussed in detail by Briaud et al. (2001); Briaud et al. (2004); Briaud et al. (2006); Oh et al. (2010) among others. To summarize, the method was developed by running several computational fluid dynamic (CFD) models for various pile group/pile cap/bridge pier configurations. Based upon these models, parametric equations were developed for maximum bed stress near the structures that are a function of structure size and velocity around the structure. Under steady flow conditions, maximum stress may be approximated as:

$$\tau_{max} = k_w k_{sp} k_{sh} k_\alpha \left\{ 0.094 \rho V^2 \left[\frac{1}{\log\left(\frac{VD'}{\nu}\right)} - \frac{1}{10} \right] \right\} \tag{1-9}$$

in which k_w, k_{sp}, k_{sh}, and k_α are correction factors for pier width, pile group spacing, pile length, and attack angle respectively; D' is the effective structure width; and V is the free-stream velocity. Ultimately, a similar expression should be developed for waves. The goal of this project was to develop a similar equation or equations for a single pile subjected to wave attack. As a corollary, because an infinite KC implies a steady current, investigators further sought to develop an expression that would revert to Equation 1-6 under steady flow conditions.

1.3 Research Tasks

To accomplish this project's objectives, several simulations of piles subjected to wave attack were developed using CFD. Results from these models were used to develop a parametric model for maximum bed stress as a function of easily computable wave and structural parameters. Specific tasks associated with this research were:

1. Task 1 – Conduct several small-scale simulations using mesh parameters relative to wave and structural geometry. Results were to be compared with previously reported data to verify that CFD could accurately reproduce experimental results. For each model, record maximum near-pile shear stress.

2. Task 2 – Upscale these small-scale models to typical field-scale conditions using the same relative mesh parameters associated with Task 1. For each model, record maximum near-pile shear stress.

3. Task 3 – Use maximum stress data from Task 1 and Task 2 to develop a parametric model for maximum near-pile shear stress that is a function of wave and/or structural dimensions.

4. Task 4 and Task 5 – Develop Draft Final and Final Reports.

1.4 Report Organization

This report details each of the research tasks enumerated in Section 1.3. In particular:

1. Details about the CFD methodology are presented in Chapter 2.

2. Results are presented in Chapter 3 along with analysis that indicated that data had been sufficiently matched.

3. Detailed data analysis including details about the parametric design models are presented in Chapter 4.

4. Chapter 5 presents a summary, conclusions from this study, and recommendations for future work.

CHAPTER 2
METHODOLOGY

2.1 Governing Equations

Siemens' Simcenter Star-CCM+ (2020) was used for all CFD modeling during this study. The discussion below details the governing equations associated with this model as well as the model conditions used throughout this study.

2.1.1 The Turbulence Model

Originally, investigators had thought that a k-epsilon RANS model would also be appropriate for this study. Investigators developed several models using k-epsilon RANS closure, but these models consistently become numerically unstable as the wave approached the vertical piles. In hindsight, this probably should have been expected. The premise behind the k-epsilon closure method is that turbulent production is somewhat balanced by turbulent dissipation (i.e., turbulence is more-or-less conserved) via the typical turbulent energy cascade. In the case of a large wave approaching a structure, significant turbulence is created because the wave tends to break against the structure. A breaking wave represents an almost-instantaneous turbulent production event that is not accurately described using a traditional energy cascade. As such, the k-epsilon approach fails to accurately describe the problem, and the model will fail to converge.

Several attempts were made to correct this issue. First, k-omega closure was attempted, but similar issues were encountered. Because k-omega closure is very similar to k-epsilon closure, this was somewhat expected. Next, several different k-epsilon variations were modeled. The governing equations behind most k-epsilon variations are similar; their differences lie in the way walls are treated in terms of describing wall stress/associated turbulent dissipation at the walls. Most of these models failed as well for large waves. Eventually, investigators ran a series of models using large eddy simulation (LES) and detached eddy simulation (DES). A LES model solves directly for flow associated with larger eddies and therefore is not plagued by the turbulent dissipation issues associated with RANS closure. The downside to an LES model is that its associated wall stresses may be inaccurate. DES models combine the best aspects of both LES and RANS. Close to a wall, DES models use RANS assumptions that yield relatively accurate wall stresses. Further from the walls, DES models utilize LES-style computations. As such, DES should yield relatively accurate wall stresses and should also be able to handle highly turbulent waves.

Performance of the LES and DES models was mixed. The LES model appeared to accurately reproduce the first wave that approached the pile but produced anomalous results near the water surface for subsequent waves. The DES models functioned well when coupled to a k-epsilon RANS model but poorly when coupled with a k-omega RANS model. Ultimately, the DES-k-epsilon model was chosen for computations because it appeared to perform well under a variety of wave conditions and scales.

The DES-k-epsilon model consisted of an Elliptic Blending DES that combined the features of the Elliptic Blending RANS model in the boundary layers, with LES model in unsteady regions. The transport equations associated with this model for the four unknown variables, turbulent kinetic energy, k; turbulent dissipation rate, ϵ; normalized wall-normal stress component, φ; and the elliptic blending factor, α, are as follows:

$$\frac{\partial}{\partial t}(\rho k) + \nabla\cdot(\rho k\bar{\boldsymbol{v}}) = \nabla\cdot\left[\left(\frac{\mu}{2}+\frac{\mu_t}{\sigma_k}\right)\nabla k\right] + P_k - \rho(\epsilon-\epsilon_0) + S_k \tag{2-1}$$

$$\frac{\partial}{\partial t}(\rho\epsilon) + \nabla\cdot(\rho\epsilon\bar{\boldsymbol{v}}) = \nabla\cdot\left[\left(\frac{\mu}{2}+\frac{\mu_t}{\sigma_\epsilon}\right)\nabla\epsilon\right] + \frac{1}{T_e}C_{\epsilon1}P_\epsilon - C^*_{\epsilon2}\rho\left(\frac{\epsilon}{T_\epsilon}-\frac{\epsilon_o}{T_o}\right) + S_\epsilon \tag{2-2}$$

$$\frac{\partial}{\partial t}(\rho\varphi) + \nabla\cdot(\rho\varphi\bar{\boldsymbol{v}}) = \nabla\cdot\left[\left(\frac{\mu}{2}+\frac{\mu_t}{\sigma_\varphi}\right)\nabla\varphi\right] + P_\varphi + S_\varphi \tag{2-3}$$

$$\nabla\cdot(L^2\nabla\alpha) = \alpha - 1 \tag{2-4}$$

In these equations, $\bar{\boldsymbol{v}}$ is the mean velocity; μ is the dynamic viscosity; P_k, P_ϵ, and P_φ are production terms; $C_{\epsilon1}$, $C^*_{\epsilon2}$, σ_k, σ_ϵ, and σ_φ are model coefficients; and S_k, S_ϵ, and S_φ are user-specified source terms. L is the turbulent length scale given by:

$$L = C_L\sqrt{\frac{k^3}{\epsilon^2} + C_\eta^2\sqrt{\frac{\nu^3}{\epsilon}}} \tag{2-5}$$

where C_L and C_η are model coefficients. ϵ_o is the ambient turbulence value in the source terms that counteracts turbulence decay. If an ambient source term is specified, then a specific time-scale, T_o is also required that is defined as:

$$T_o = \max\left(\frac{k_o}{\epsilon_o}, C_t\sqrt{\frac{\nu}{\epsilon_o}}\right) \tag{2-6}$$

where $\bar{\boldsymbol{v}}$ is the mean velocity; μ the dynamic viscosity; P_k is a production term; and S_k is a user-specified source term. Of course, these are the same equations that would be used for any elliptic blending RANS model. For our case, where DES was used, the typical turbulent dissipation rate, ϵ is replaced by $\bar{\epsilon}$. Dissipation is then described by:

$$\bar{\epsilon} = \frac{k^{\frac{3}{2}}}{\bar{d}} \tag{2-7}$$

where $\overline{d}$ is given by:

$$\overline{d} = \frac{k^{\frac{3}{2}}}{\epsilon} - f_d \max\left(0, \frac{k^{\frac{3}{2}}}{\epsilon} - \psi C_{DES}\Delta\right) \tag{2-8}$$

in which

$$\Delta = \max(\Delta_x, \Delta_y, \Delta_z) \tag{2-9}$$

Δ is known as the filter width in which Δ_x, Δ_y, and Δ_z are characteristic mesh spacing in all three spatial directions. C_{DES} is a model coefficient that is equal to 0.2. f_d is given by:

$$f_d = 1 - \tanh[(8r_d)^3] \tag{2-10}$$

$$r_d = \frac{\nu_t + \nu}{\sqrt{U_{i,j}U_{i,j}}\kappa^2 d^2} \tag{2-11}$$

where ν_t is the kinematic viscosity; ν is the molecular viscosity; $U_{i,j}$, the velocity gradients; κ the von Karman constant; and d the distance to the wall. The parameter ψ is a low-Reynolds number correction function that prevents activation of the low-Reynolds number terms when the model is in “LES mode.” It is given by:

$$\psi^2 = \min\{100, (1 - \frac{C_{b1}([f_{t2}+(1-f_{t2})f_{v2}]/f_w^* \kappa^2 C_{w1}))}{(1-f_{t2})f_{v1}} \tag{2-12}$$

C_{b1} and C_{w1} are modeling coefficients that are equal to 0.1355 and 0.2 respectively. f_{t2} is a damping function given by:

$$f_{t2} = C_{t3}\exp(-C_{t4}\chi^2) \tag{2-13}$$

and

$$\chi = \frac{\nu_t + \nu}{\nu} \tag{2-14}$$

2.1.2 VOF Model Formulation

The Volume of Fluid (VOF) multiphase model predicts the distribution and movement of the interface of immiscible phases. The distribution of phases and the position of the interface are described by the fields of phase volume fraction, α_i. The volume fraction of phase i is defined as:

$$\alpha_i = \frac{V_i}{V} \tag{2-24}$$

where V_i is the volume of phase i in the cell and V is the volume of the cell. The volume fractions of all phases in a cell must sum to one:

$$\sum_{i=1}^{N} \alpha_i = 1 \tag{2-25}$$

where *N* is the total number of phases. Depending on the value of the volume fraction, the different fluids in a cell can be distinguished as one of three categories: α_i = 0 when a cell is completely void of phase i, α_i = 1 when a cell is completely filled with phase i, and $0 < \alpha_i < 1$ values between the two limits indicate the presence of an interface between phases.

The material properties calculated in the cells containing the interface depend on the material properties of the present fluids. The fluids present in an interface-containing cell are treated as a mixture:

$$\rho = \sum_i \rho_i \alpha_i \tag{2-26}$$

$$\mu = \sum_i \mu_i \alpha_i \tag{2-27}$$

$$C_p = \sum_i \frac{(C_p)_i \rho_i}{\rho} \alpha_i \tag{2-28}$$

2.1.3 The Wave Models

Two wave models were used throughout this study. As shown below in Figure 2-1, as water depth and steepness change, various wave models become more or less applicable.

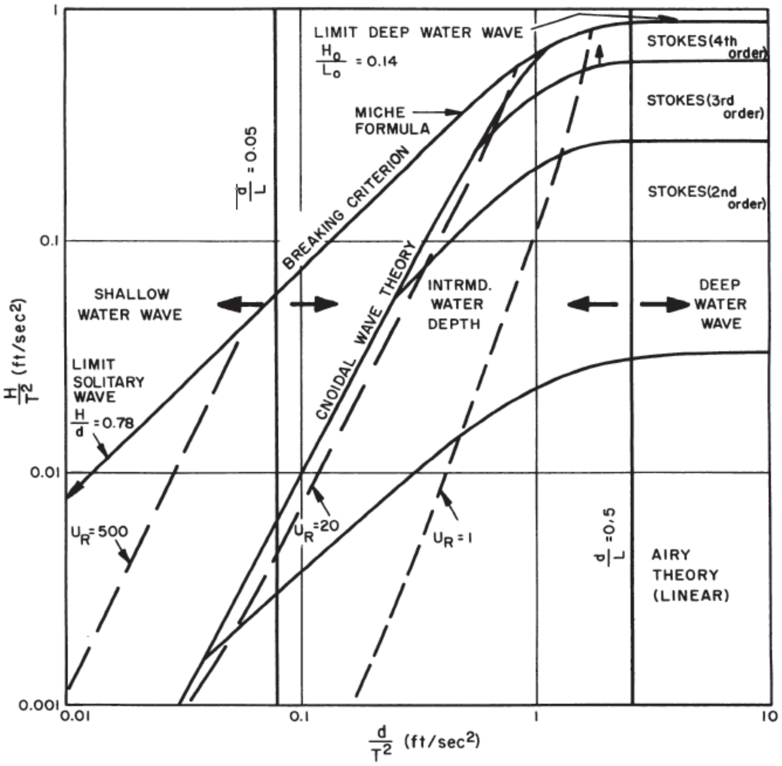

Figure 2-1. Applicability of different wave theories (adapted from Le Méhauté, 1976)

Figure 2-1 shows that in shallow water and for steeper waves, cnoidal theory is more appropriate while for deeper water and less steep waves, Airy (i.e., linear) wave theory is more appropriate. The small-scale simulations were conducted using relatively deep water and waves with relatively low steepness. As such, linear wave theory was used for small-scale simulations. During large-scale simulations, water was relatively shallow, and the waves were relatively steep. Therefore, cnoidal wave theory was used during the large-scale simulations.

2.1.3.1 First Order Waves

First order waves utilize simple trigonometric profiles to approximate water surface elevation, η:

$$\eta = a\cos(||K||x - \omega t) \tag{2-30}$$

A velocity potential is found by linearly solving the Laplacian and used to define vertical and horizontal orbital velocities:

$$v_h = a\omega\cos(||\mathrm{K}||\mathrm{x} - \omega t)\, e^{Kz} \tag{2-31}$$

$$v_v = a\omega \sin(||K||x - \omega t)\, e^{Kz} \tag{2-32}$$

In these equations, a is the wave amplitude; ω is the wave frequency; K is the wave number vector and z is the vertical distance downward from the still water level. The wave period is:

$$T = \frac{2\pi}{\omega} \tag{2-33}$$

And the wavelength is:

$$L = \frac{2\pi}{||K||} \tag{2-34}$$

Note that in these expressions, ||(some variable)|| represents the variable's magnitude (for example, $||K||$ is the magnitude of the wave number vector, K). The dispersion relationship provides the relationship among wave period, water depth, and wavelength and is given below in Eq. 2-35:

$$T = [\frac{g}{2\pi L}\tanh\left(\frac{2\pi d}{L}\right)]^{-1/2} \tag{2-35}$$

2.1.3.2 Cnoidal Waves

A cnoidal wave is nonlinear with an exact periodic wave solution. Cnoidal waves are used to describe gravity waves that have considerably long wavelengths compared to their respective depths; these conditions usually occur in shallow water. The solutions to cnoidal waves is the well-known Korteweg-de Vries (KDV) equation where surface elevation is proportional to the square of the Jacobian elliptic function, cn( ). The KDV equation is usually expressed as a function of ϵ which is the ratio between the wave height, H relative to the water depth, d. The solution to the KDV equation for water surface elevation is given below in Eq. 2-36:

$$\frac{\eta}{d} = 1 + \left(\frac{\epsilon}{m}\right) m\mathrm{cn}^2 + \left(\frac{\epsilon}{m}\right)^2 \left(-\frac{3}{4}m^2\mathrm{cn}^2 + \frac{3}{4}m^2\mathrm{cn}^4\right) + \left(\frac{\epsilon}{m}\right)^3 \left[\left(-\frac{61}{80}m^2 + \frac{111}{80}m^3\right)\mathrm{cn}^2 + \left(\frac{61}{80}m^2 - \frac{53}{20}m^3\right)\mathrm{cn}^4 + \frac{101}{80}m^3\mathrm{cn}^6\right] \tag{2-36}$$

The solution to the KDV equation for velocity is very complicated, but similar in form to Eq. 2-36 in the sense that it is also a function of ϵ and cn( ). For details, please refer to Korteweg and de Vries (1895).

2.1.4 Wave Forcing

Wave forcing allows the coupling of the simulation with a theoretical solution or simplified numerical solution specified by the VOF waves. By implementing the wave forcing function, the computing effort is reduced by using a reduced-size solution domain. Any problems associated with reflections of surface waves at the boundaries is eliminated resulting in a dampening feature and gradual forcing. Wave forcing is only applied to momentum and therefore is achieved by adding a source term to the momentum equations of the form:

$$q_\phi = -\gamma\rho(\phi - \phi^*) \tag{2-37}$$

where γ is the forcing coefficient; ϕ is the current solution of the transport equation; and ϕ^* is the value towards which the solution is forced. The source term is applied with a variable forcing coefficient over a specified forcing zone. The width of the forcing zone can be different depending on the boundaries, but the optimal width of the forcing zone depends on the modeled problem. The forcing coefficient relationship is derived from a smooth variation from zero at the inner edge of the forcing zone to the maximum value γ at the boundary in the form:

$$\gamma = -\gamma_o cos^2(\frac{\pi x^*}{2}) \tag{2-38}$$

Forcing was used one wavelength upstream and downstream from the flow domains' inlets and outlets.

2.1.5 Eulerian Phases

The Eulerian approach uses equations for multiple fluid elements making up a region fixed in space. Like the mass conservation equation, the rate of change per unit volume for a fluid is considered. The rate of change of property ϕ per unit volume for a fluid particle is given through the product of $\frac{D\emptyset}{Dt}$ and density, ρ as stated below:

$$\rho\frac{D\emptyset}{Dt} = \rho(\frac{\partial\emptyset}{\partial t} + \mathbf{u}\cdot\nabla\emptyset) \tag{2-39}$$

Two fluid phases were defined: water and air. Water was assumed to have a constant density of $998\frac{kg}{m^3}$; dynamic viscosity of 8.89 x 10^{-4} Pa·s; and molecular weight of $18\frac{kg}{mol}$. Air was assumed to have a constant dynamic viscosity of 1.85 x 10^{-5}Pa· and molecular weight of $29\frac{kg}{mol}$. The air's compressibility was modeled using a simple ideal gas law:

$$\rho = \frac{p}{RT} \tag{2-40}$$

Where the specific gas constant, R, is defined as:

$$R = \frac{R_u}{M} \tag{2-41}$$

Where R_u is the universal gas constant and M is the molecular weight.

2.2 Test Conditions, Geometry, and Meshing

2.2.1 Test Conditions

Test conditions associated with each model are shown below in Table 2-1 and Table 2-2:

Table 2-1. Large-Scale Test Matrix

Run No	T (s)	H (m)	h (m)	D (m)	L (m)
LS1	8.00	4.50	7.50	1.53	63.16
LS2	12.00	4.50	7.50	1.53	99.46
LS3	16.00	4.50	7.50	1.53	134.57
LS4	8.00	4.50	7.50	1.00	63.16
LS5	12.00	4.50	7.50	1.00	99.46
LS6	16.00	4.50	7.50	1.00	134.57
LS7	8.00	4.50	7.50	0.54	63.16
LS8	12.00	4.50	7.50	0.54	99.46
LS9	16.00	4.50	7.50	0.54	134.57
LS10	8.00	2.25	7.50	1.53	63.16
LS11	12.00	2.25	7.50	1.53	99.46
LS12	16.00	2.25	7.50	1.53	134.57
LS13	8.00	2.25	7.50	1.00	63.16
LS14	12.00	2.25	7.50	1.00	99.46
LS15	16.00	2.25	7.50	1.00	134.57
LS16	8.00	2.25	7.50	0.54	63.16
LS17	12.00	2.25	7.50	0.54	99.46
LS18	16.00	2.25	7.50	0.54	134.57
LS19	8.00	9.00	15.00	1.53	81.70
LS20	12.00	9.00	15.00	1.53	135.45
LS21	16.00	9.00	15.00	1.53	186.32
LS22	8.00	9.00	15.00	1.00	81.70
LS23	12.00	9.00	15.00	1.00	135.45
LS24	16.00	9.00	15.00	1.00	186.32
LS25	8.00	9.00	15.00	0.54	81.70
LS26	12.00	9.00	15.00	0.54	135.45
LS27	16.00	9.00	15.00	0.54	186.32
LS28	8.00	4.50	15.00	1.53	81.70
LS29	12.00	4.50	15.00	1.53	135.45
LS30	16.00	4.50	15.00	1.53	186.32
LS31	8.00	4.50	15.00	1.00	81.70
LS32	12.00	4.50	15.00	1.00	135.45
LS33	16.00	4.50	15.00	1.00	186.32
LS34	8.00	4.50	15.00	0.54	81.70
LS35	12.00	4.50	15.00	0.54	135.45
LS36	16.00	4.50	15.00	0.54	186.32

Table 2-2: Small-Scale Test Matrix

Run Number	T (s)	H (cm)	L (m)	D (m)	d (m)
SS1	3.5	12.0	6.79	1.0	0.40
SS2	3.5	8.6	6.79	1.0	0.40
SS3	3.5	4.9	6.79	1.0	0.40
SS4	2.0	8.2	3.70	1.0	0.40
SS5	3.5	2.5	6.79	1.0	0.40
SS6	3.5	5.7	6.79	1.0	0.40
SS7	3.5	6.4	6.79	0.54	0.40
SS8	3.5	6.9	6.79	0.54	0.40
SS9	3.5	6.9	6.79	0.54	0.40
SS10	3.5	6.9	6.79	0.54	0.40
SS11	3.5	6.4	6.79	0.54	0.40
SS12	3.5	5.6	6.79	0.54	0.40
SS13	3.5	12.0	6.79	1.53	0.40
SS14	3.5	8.7	6.79	1.53	0.40
SS15	3.5	6.9	6.79	1.53	0.40
SS16	3.5	6.4	6.79	1.53	0.40

2.2.2 Geometries and Meshing

Generally, models consisted of vertical piles protruding into hyper-rectangular flow domains. Pile dimensions were dictated by Table 2-1 and Table 2-2. Hyper-rectangular width and length were defined as functions of wavelength, *L*, and pile diameter, *D*, respectively. Hyper-rectangular length, *X*, was specified as 5 wavelengths; heights, *Z*, were specified as 2.5 water depths; and widths, *Y*, were specified as 4 pile diameters + 5 wave heights. Similarly, cell sizes were also specified as functions of wave parameters. First, cell size in the z-direction near the free surface, *dz*, was specified as a function of water depth:

$$dz = \frac{d}{37.5} \tag{2-42}$$

This scale factor of 37.5 was found after some trial-and-error so that a reasonable number of cells (relative to available computational resources) would be generated and results would be relatively accurate. Then, an aspect ratio between *dz* and x- and y-resolution (i.e., *dx* and *dy*) was chosen. As discussed in communications with Siemens, aspect ratios between 2 and 4 are recommended for most wave models. Investigators chose an aspect ratio of 3:

$$dx = dy = 3dz \tag{2-43}$$

In the air and far away from the free surface, cells were isotropic whereby their width, length, and height were given by the result from Eq. 2-43. Two wave heights up from the free surface in the z-direction, Equation 2-42 was used for *dz*, and *dx* and *dy* were scaled using Eq. 2-43. Two wave heights down from the free surface, two times Eq. 2-42 was used for *dz*; and once again, Eq. 2-43 was used to scale *dx* and *dy*. In addition, in all mesh regions, a prism layer was added to improve near-wall resolution. Each prism layer was 6 cells in height, with a minimum cell size of 33% of that region's base cell-size in the z-direction. A schematic of a representative geometry is presented below in Figure 2-2 while representative mesh cross-sections are shown in Figure 2-3 and Figure 2-4.

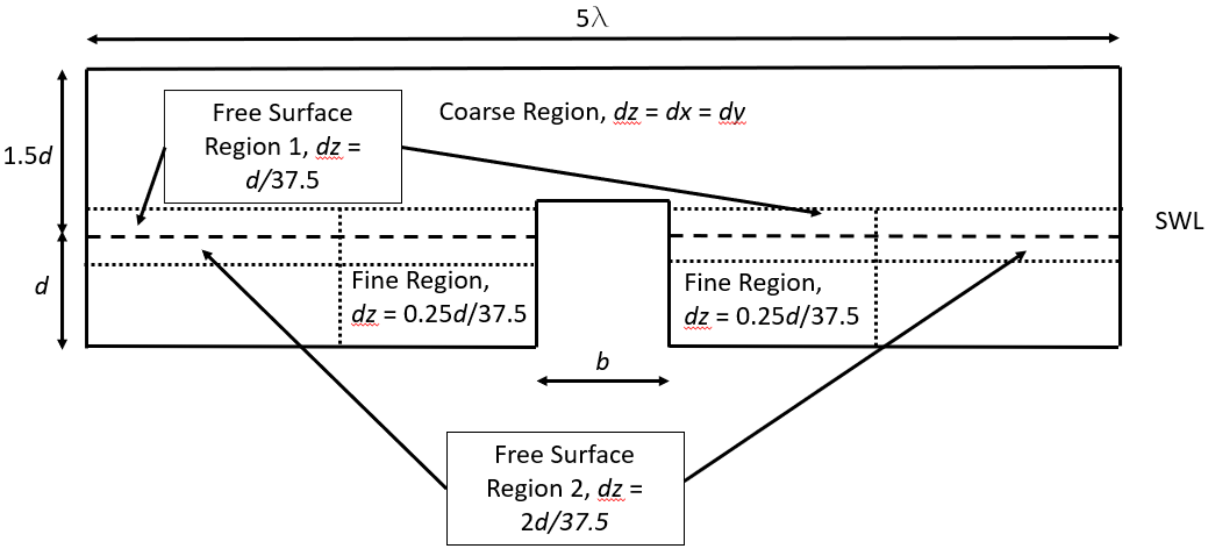

Figure 2-2. Schematic cross-section of flow domain in the x-z direction

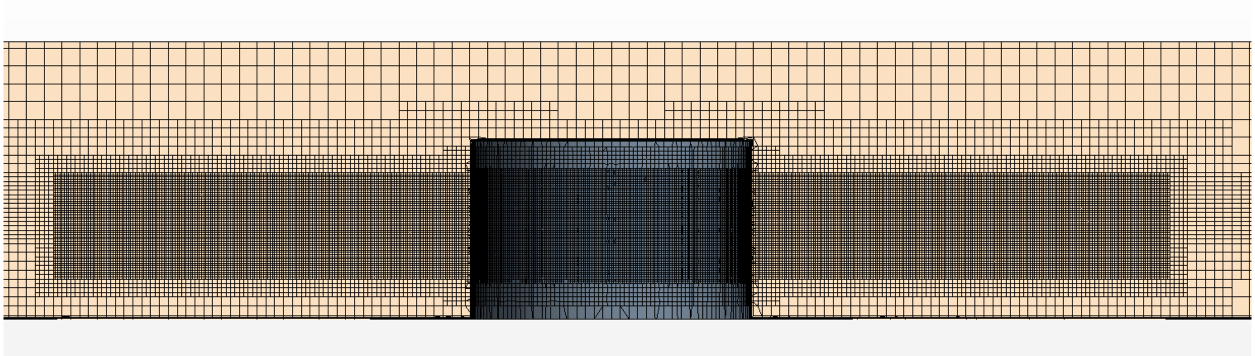

Figure 2-3. Mesh cross-section in x-z direction

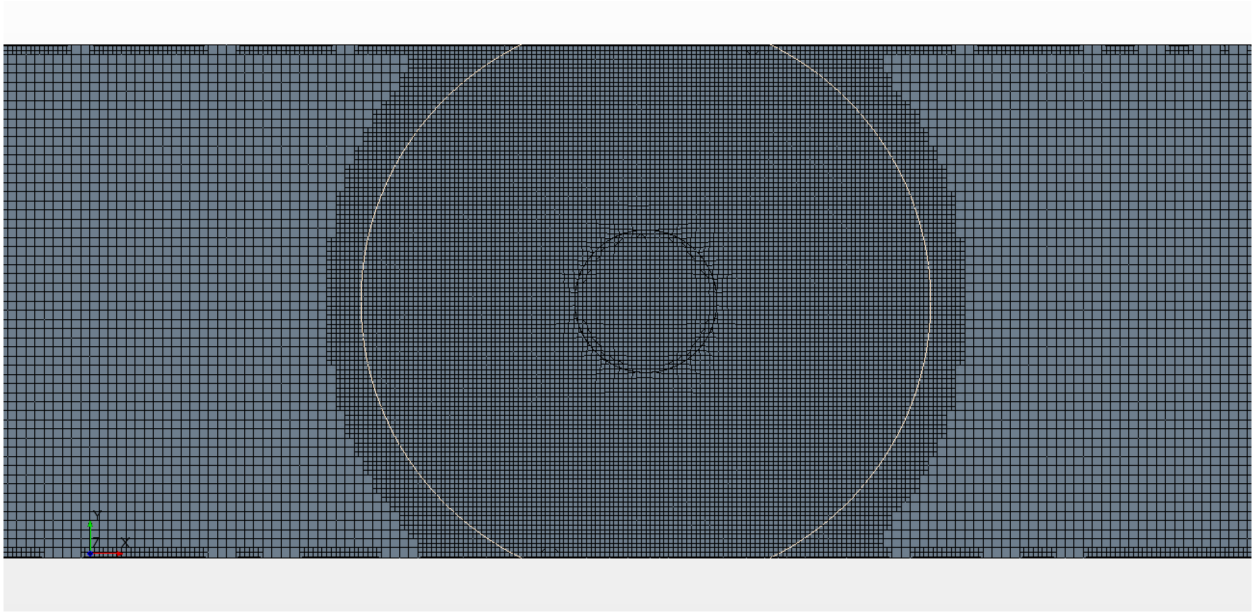

Figure 2-4. Top-down view of the mesh showing bottom of flow domain in x-y direction

2.2.3 Boundary Conditions

Investigators attempted several different combinations of boundary conditions. While numerical results were similar most of the time for most boundary condition combinations, sometimes upscaling led to numerical instability for several boundary configurations. Ultimately, the boundary conditions illustrated below in Figure 2-5 and Figure 2-6 produced the best, numerically stable, and accurate results:

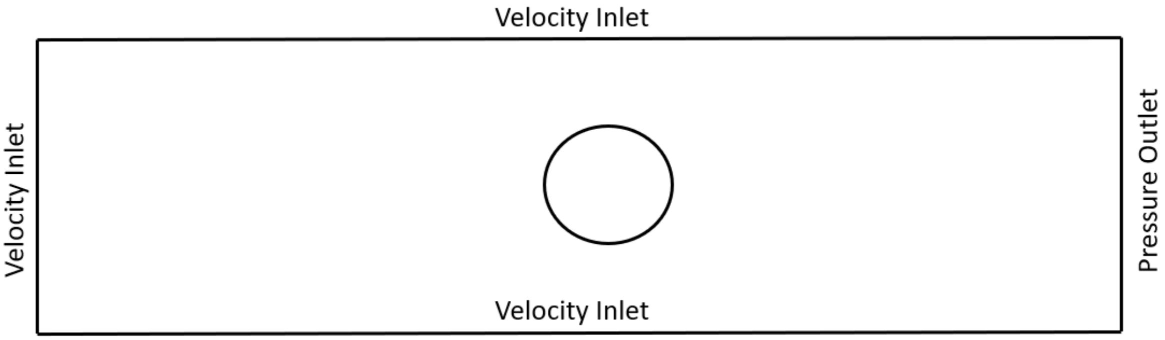

Figure 2-5. Boundary conditions top view (waves propagate from left-to-right)

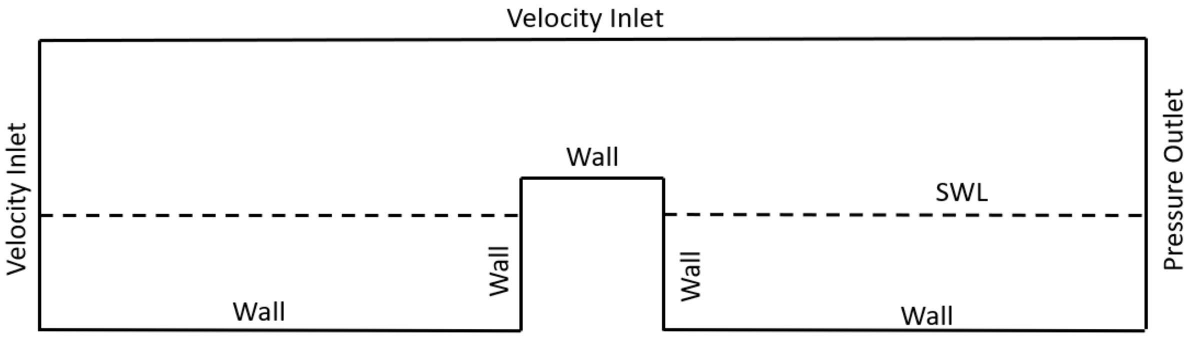

Figure 2-6. Boundary condition side view (waves propagate from left-to-right)

As shown, the piles and bottoms of the flow domains were assumed to be walls. The upstream domain face and lateral domain faces were assumed to consist of velocity inlets. Pressure was released from the models from its downstream edge using a pressure outlet. Details about each of these boundary conditions is presented below:

2.2.3.1 Walls

A wall boundary represents an impermeable surface where wall shear stress, τ_w may be computed via Eq. 2-44:

$$\tau_w = \rho u_\tau^2 \left(\frac{\hat{v}_{tangental}}{|\hat{v}_{tangental}|} \right) \tag{2-44}$$

where ^ indicates a RANS or LES filtered value. μ_τ is the wall friction velocity given by:

$$\mu_\tau = \frac{u_*}{u_+} |\hat{v}_{tangental}| \tag{2-45}$$

in which u_* is the velocity scale; and u_+ is the non-dimensional wall-tangential velocity component of the velocity vector. Both u_* and u_+ are approximated using blended wall functions given in Eqs. 2-46 and 2-47:

$$u_* = \frac{\gamma\mu|v_{tangental}|}{\rho y} + (1-\gamma)C_\mu^{0.25}k^{0.5} \tag{2-46}$$

$$u_+ = \frac{1}{\kappa}\ln(1+\kappa y^+) + C(1 - \exp\left(-\frac{y^+}{y_m^+}\right) - \frac{y^+}{y_m^+}\exp(-by^+) \tag{2-47}$$

in which

$$C = \frac{1}{\kappa}\ln\left(\frac{E}{\kappa}\right) \tag{2-48}$$

$$b = \frac{1}{2}\left(y_m^+ \frac{\kappa}{C} + \frac{1}{y_m^+}\right) \tag{2-49}$$

$$y_m^+ = \max(3{,}267(2.64 - 3.9\kappa)E'^{0.0125}) - 0.987 \tag{2-50}$$

$$E' = \frac{E}{f} \tag{2-51}$$

E is the log law offset; and f is the roughness function:

$$f = \begin{cases} 1 & Re^+ \leq Re^+_{smooth} \\ \left[\frac{B\left(Re^+ - Re^+_{smooth}\right)}{Re^+_{rough} - Re^+_{smooth}} + CR^+\right]^a & Re^+_{smooth} < Re^+ < Re^+_{rough} \\ b + CR^+ & Re^+ > Re^+_{rough} \end{cases} \tag{2-52}$$

where B, C, R^+_{smooth} and R^+_{rough} are model coefficients and a is defined by:

$$a = \sin\left[\frac{\pi}{2}\,\frac{log\left(Re^+/Re^+_{smooth}\right)}{log\left(Re^+_{rough}/Re^+_{smooth}\right)}\right] \tag{2-53}$$

In other words, because of blending, no assumptions are made about viscous sublayer location/resolution, and there is no need for an explicit blending function between the viscous sublayer and the logarithmic region near the wall as shown below in Figure 2-7.

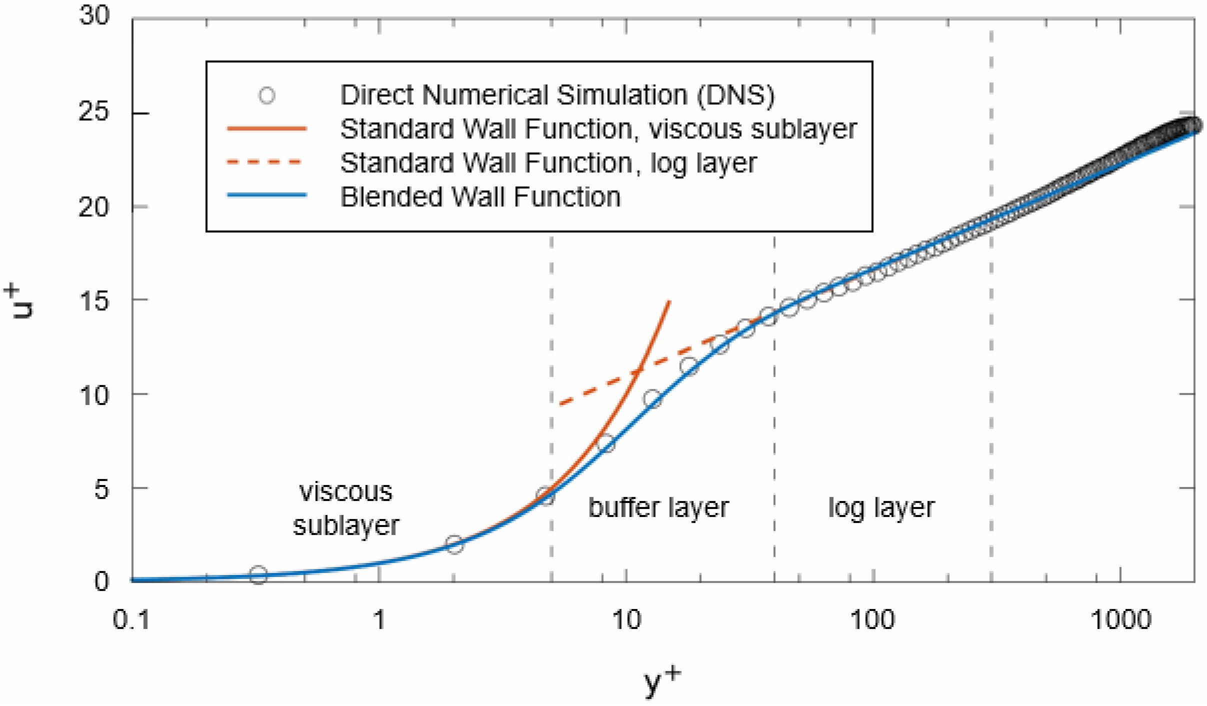

Figure 2-7. Diagram showing blending function near wall (adapted from Siemens, 2020)

2.2.3.2 Velocity Inlets

The velocity inlet boundary was used as an inflow/outflow condition where the velocity (v_{spec}), direction of flow ($\boldsymbol{\theta}_{spec}$), and fluid properties are known within a reference frame. At an inflow boundary, the known conditions are used to calculate the inlet velocity flux as well as the momentum and energy fluxes. The inflow velocity is then determined through these specified variables:

$$\mathbf{v} = \mathrm{v}_{\mathrm{spec}} \cdot \boldsymbol{\theta}_{spec} \tag{2-54}$$

2.2.3.3 Pressure Outlet

At a pressure outlet, the boundary velocity is extrapolated from interior domain cells represented as:

$$\mathbf{v} = \mathbf{v}^{\mathrm{ext}} \tag{2-55}$$

The static pressure at the boundary is calculated as:

$$P_s = \begin{cases} P_{spec} & \text{For subsonic flow} \\ P_s^{ext} & \text{For supersonic flow} \end{cases} \tag{2-56}$$

Where P_{spec} represents the difference between the absolute and reference pressure relative to the reference pressure.

2.3 Run Conditions

Star-CCM+'s implicit unsteady solver was used throughout all computations. Like the meshes, implicit timesteps were also computed relative to wave conditions by setting the Courant Number, *C*, to 0.2. The Courant Number is defined as:

$$C = u_{wave} \frac{\Delta t}{\Delta x} \tag{2-57}$$

Therefore, if *C* = 0.2:

$$\Delta x = u_{wave} \frac{\Delta t}{0.2} \tag{2-58}$$

In which u_{wave} is the wave celerity (i.e, λ/T); and Δt is the implicit time step. Each time step was solved used 10 iterations. As will be shown below in Chapter 3, this appeared to produce relatively accurate results when compared with experimental results and appeared to produce relatively low residuals after 10 iterations. During each run, several wavelengths (usually 10 waves or when not 10 waves, enough for repeatable conditions to develop) were computed.

Data were monitored using two methods. Stress data from Sumer and Fredsoe consisted of undisturbed (i.e., upstream) measurements. As such, a point probe was installed one wavelength upstream from the piles along the bed so that undisturbed shear stress could be measured. In addition, investigators assumed that maximum stress would occur near the pile. As such, a bottom stress monitor was setup whereby maximum bottom stress was tracked as a function of time.

CHAPTER 3
RESULTS

3.1 Small-Scale Results – Matching the Data

Raw upstream wave data from the smooth-bottom results are presented below from Figure 3-1 through Figure 3-16 where stress magnitude at a point one wavelength upstream from the pile is shown. These data were used to match experimental results from Sumer and Fredsoe.

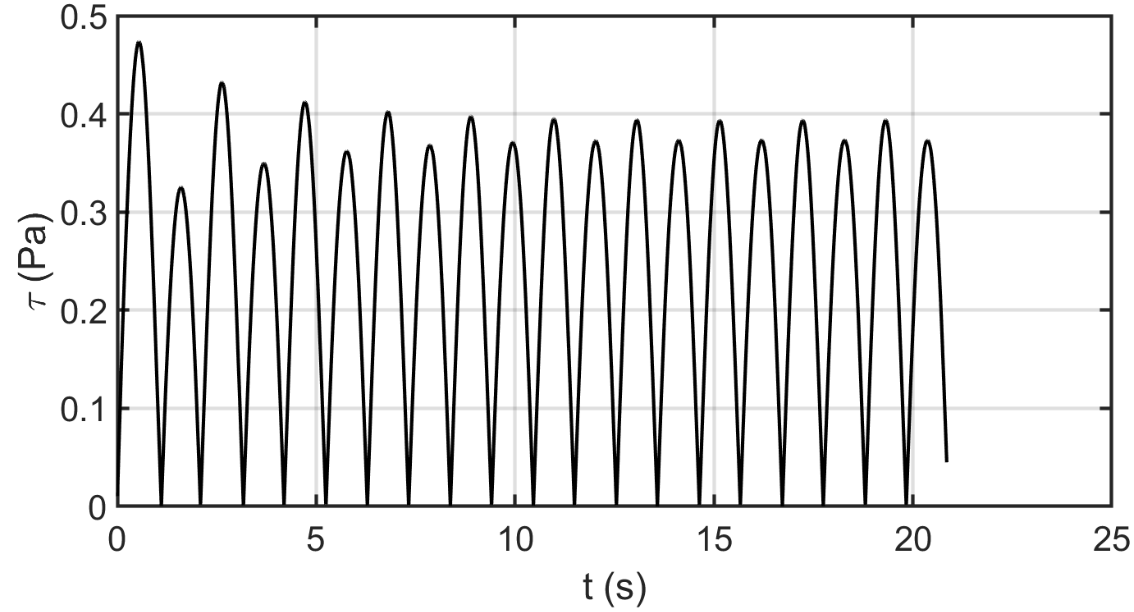

Figure 3-1. Raw upstream wave data from Run SS1 showing bottom stress vs. time

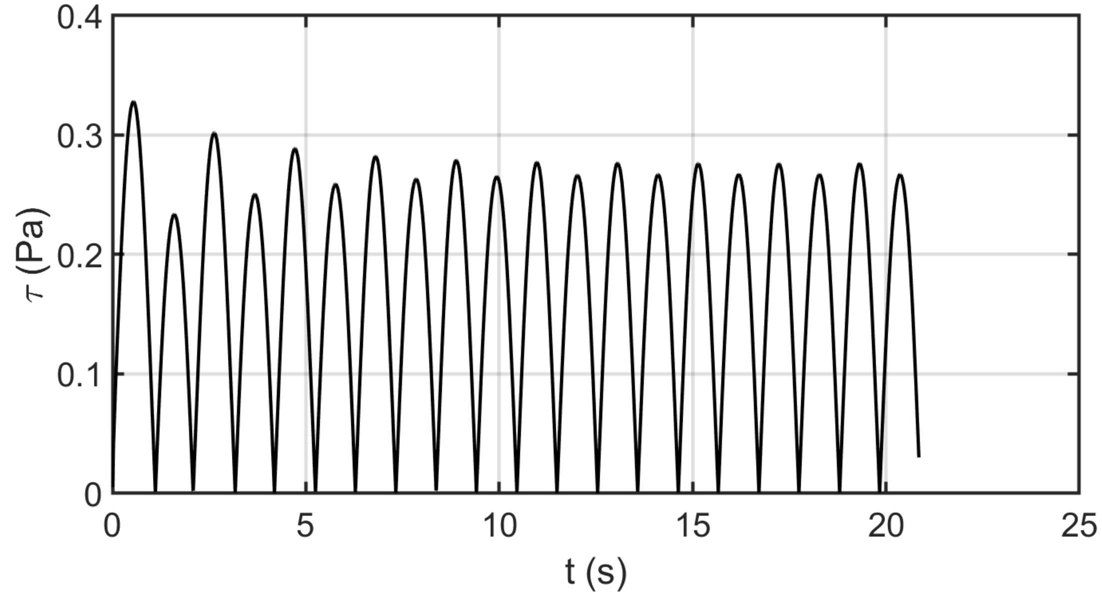

Figure 3-2. Raw upstream wave data from Run SS2 showing bottom stress vs. time

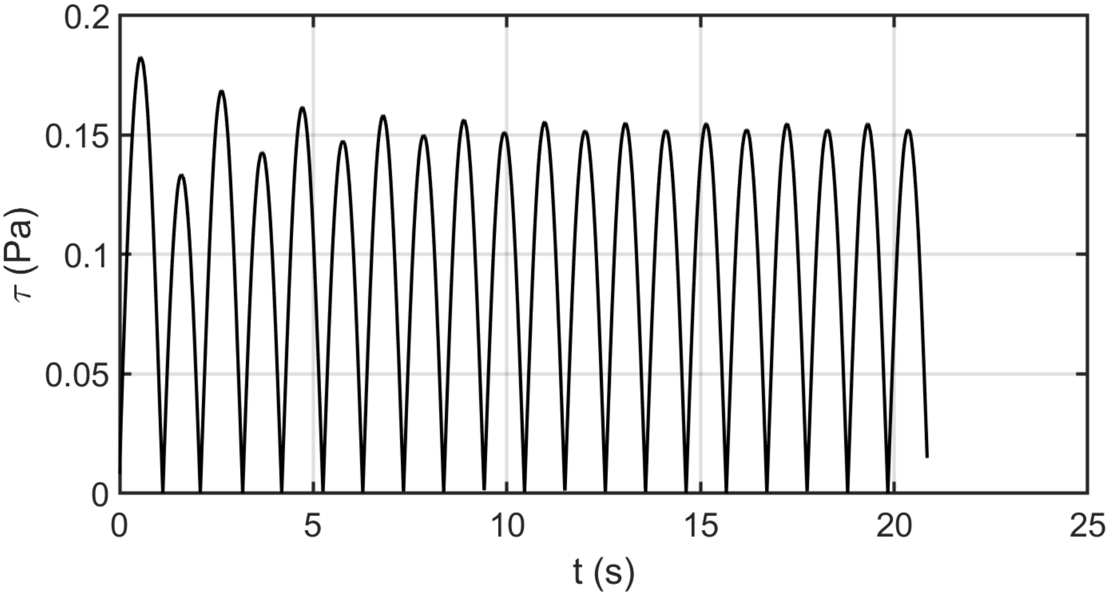

Figure 3-3. Raw upstream wave data from Run SS3 showing bottom stress vs. time

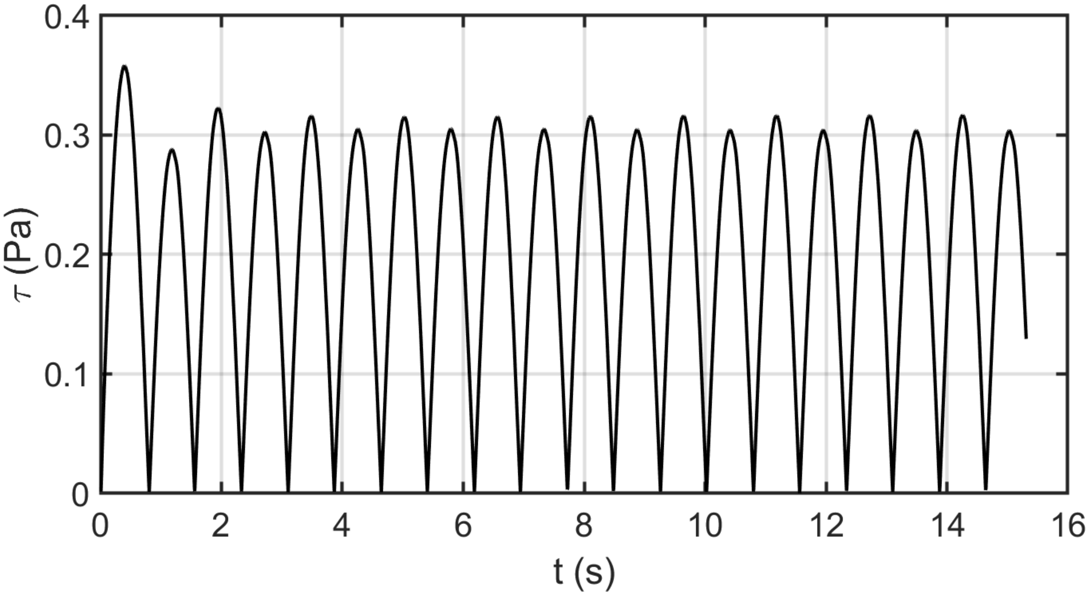

Figure 3-4. Raw upstream wave data from Run SS4 showing bottom stress vs. time

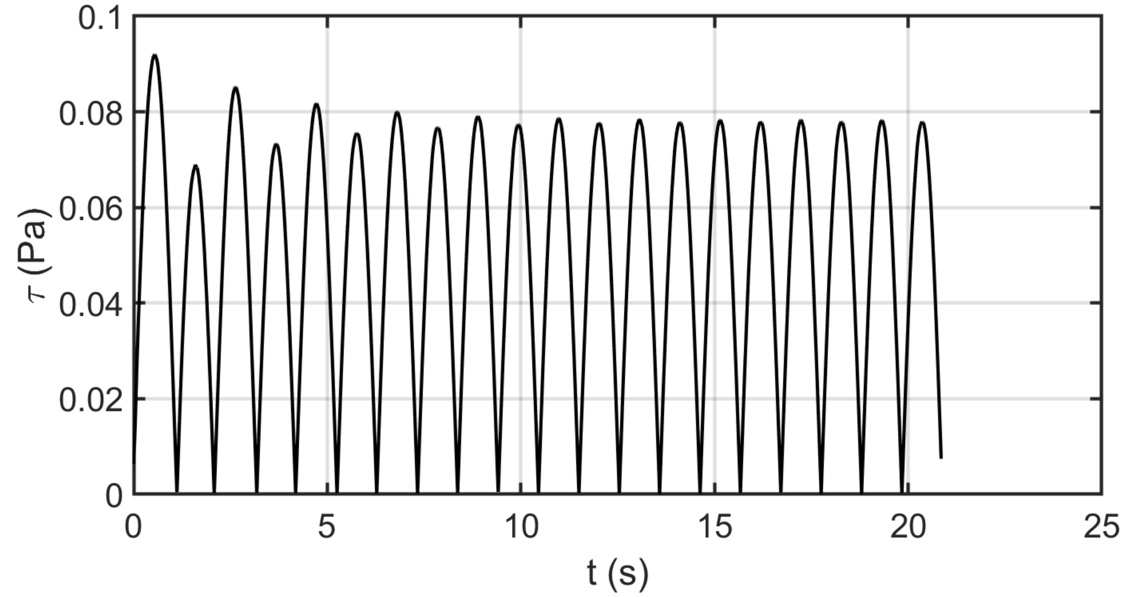

Figure 3-5. Raw upstream wave data from Run SS5 showing bottom stress vs. time

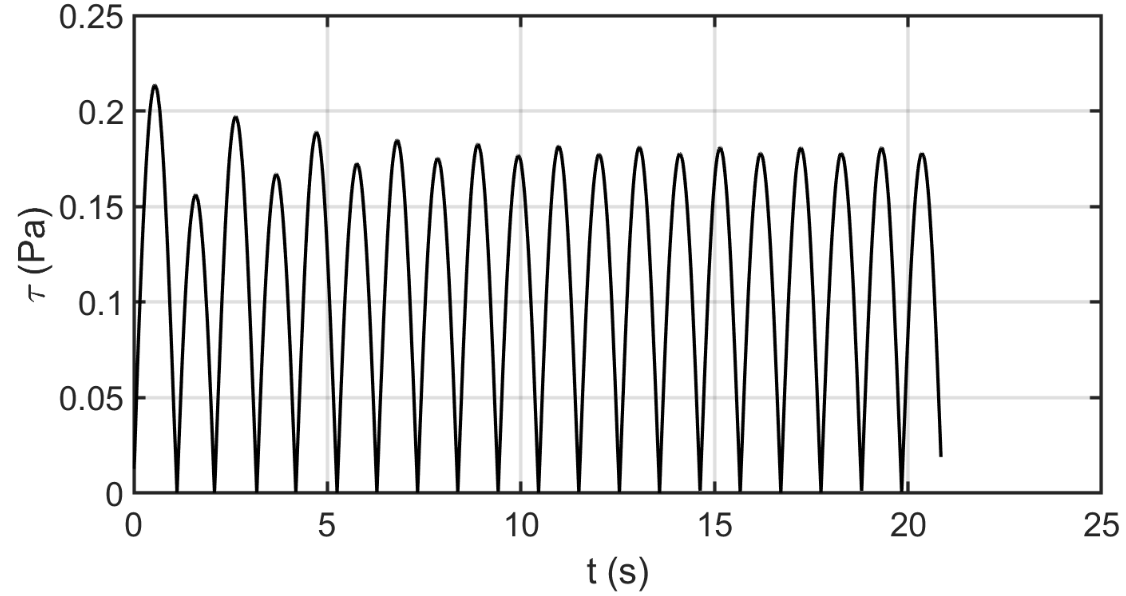

Figure 3-6. Raw upstream wave data from Run SS6 showing bottom stress vs. time

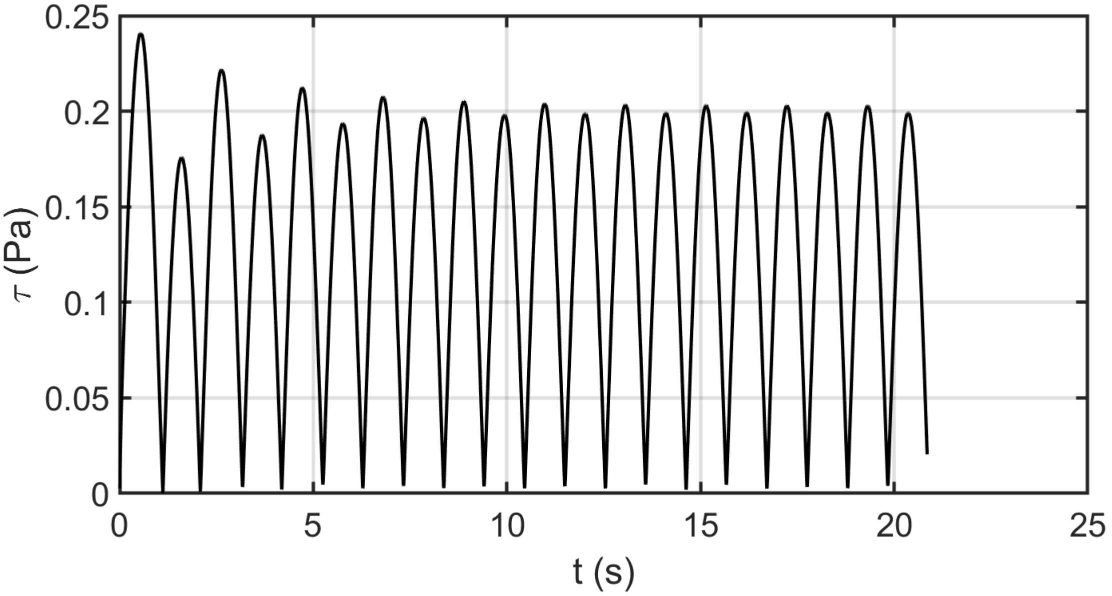

Figure 3-7. Raw upstream wave data from Run SS7 showing bottom stress vs. time

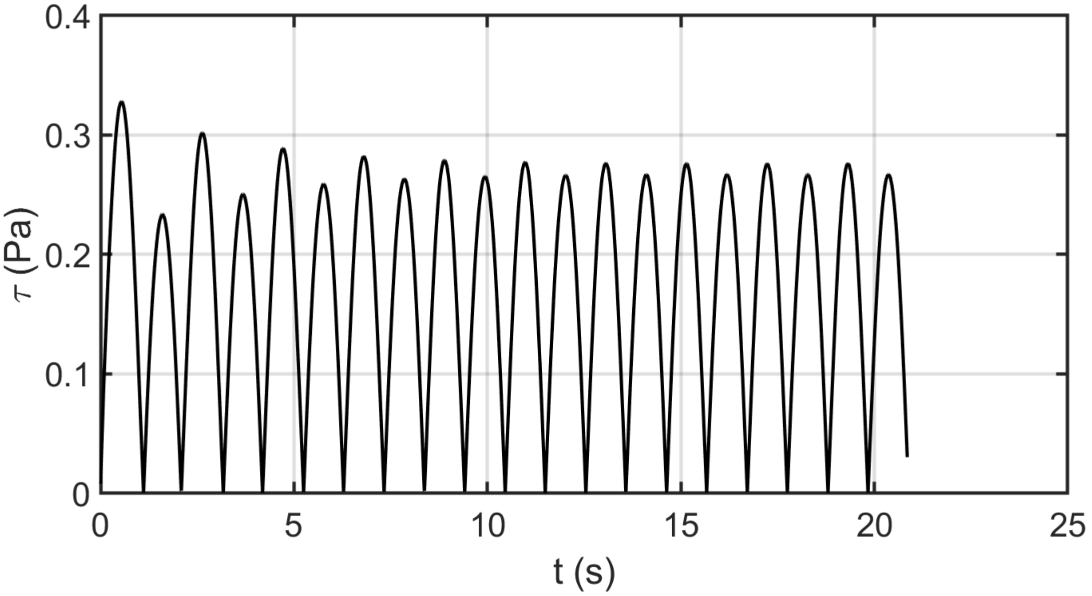

Figure 3-8. Raw upstream wave data from Run SS8 showing bottom stress vs. time

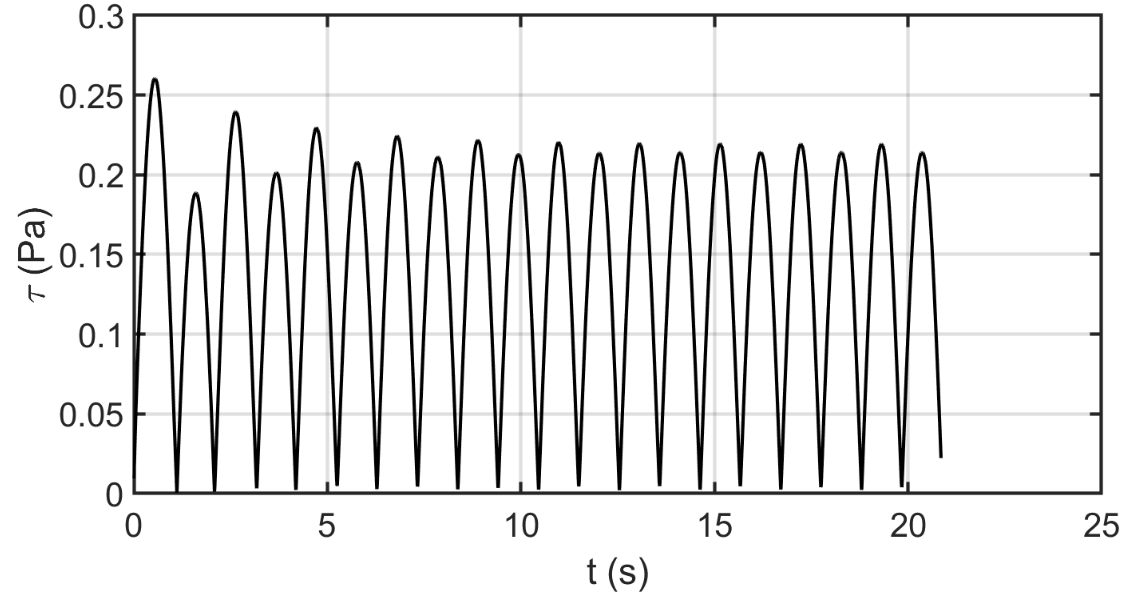

Figure 3-9. Raw upstream wave data from Run SS9 showing bottom stress vs. time

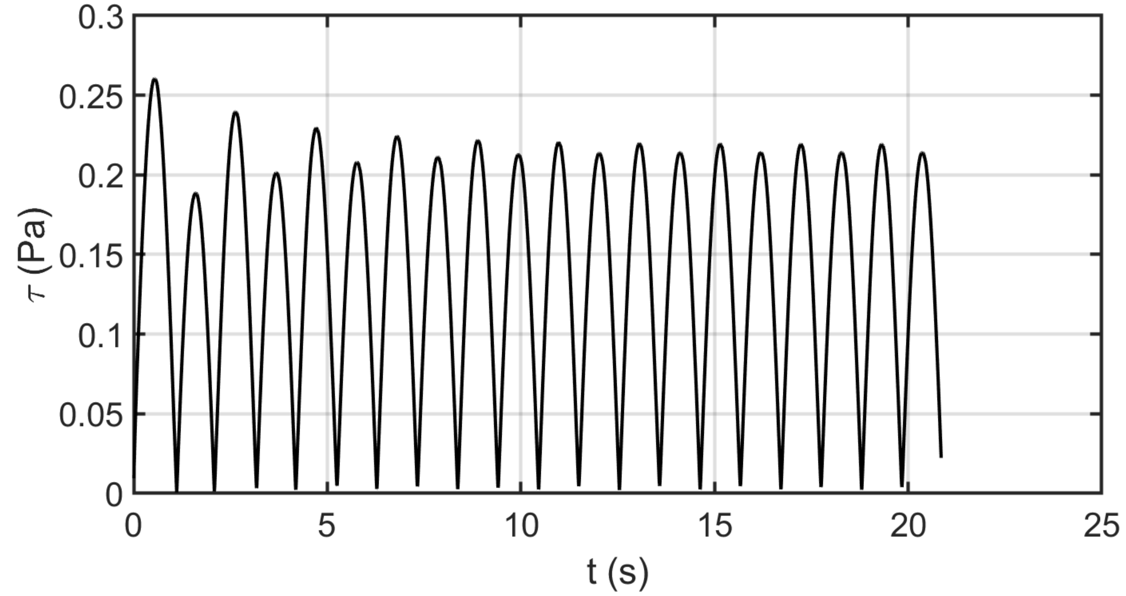

Figure 3-10. Raw upstream wave data from Run SS10 showing bottom stress vs. time

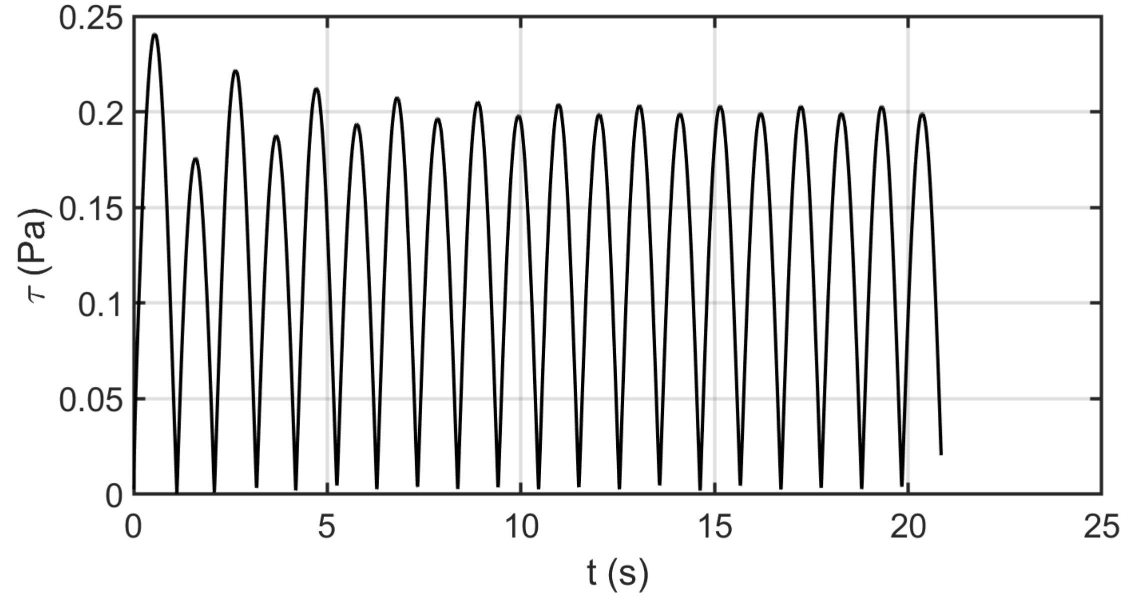

Figure 3-11. Raw upstream wave data from Run SS11 showing bottom stress vs. time

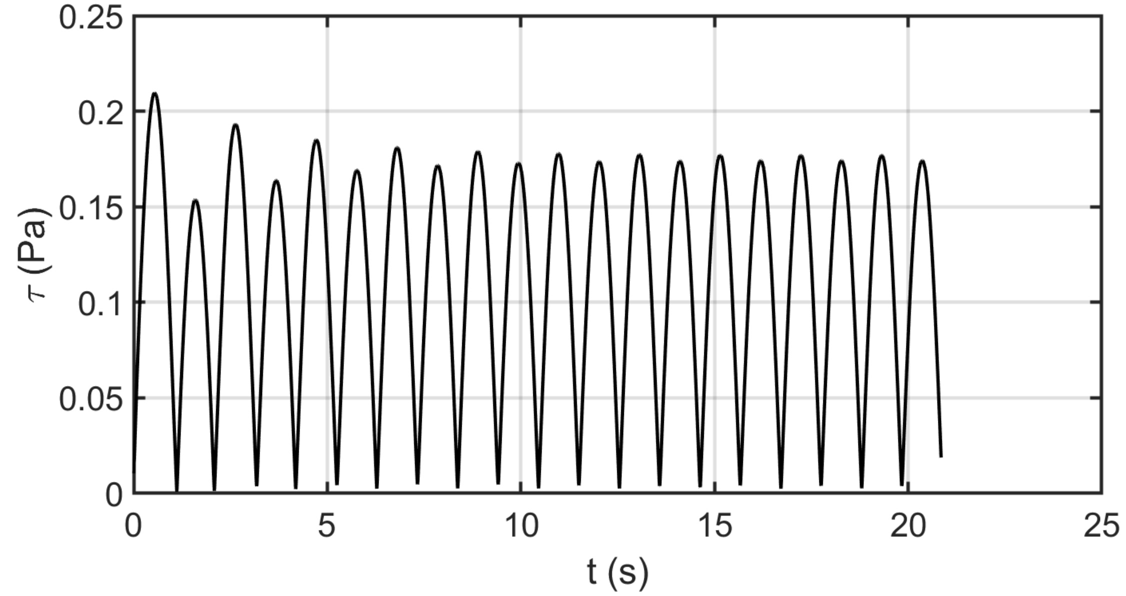

Figure 3-12. Raw upstream wave data from Run SS12 showing bottom stress vs. time

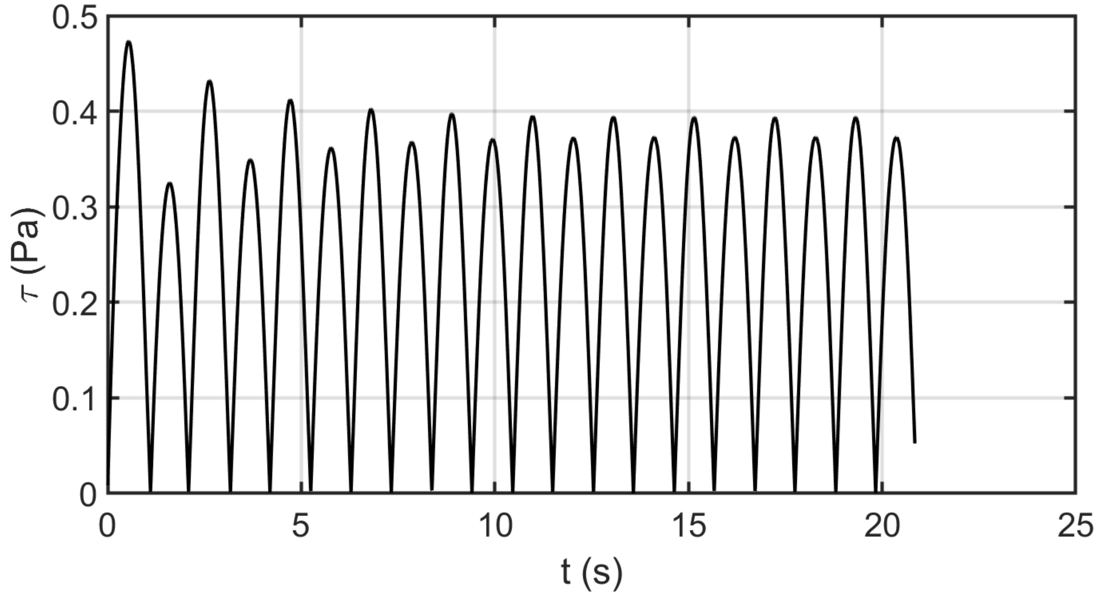

Figure 3-13. Raw upstream wave data from Run SS13 showing bottom stress vs. time

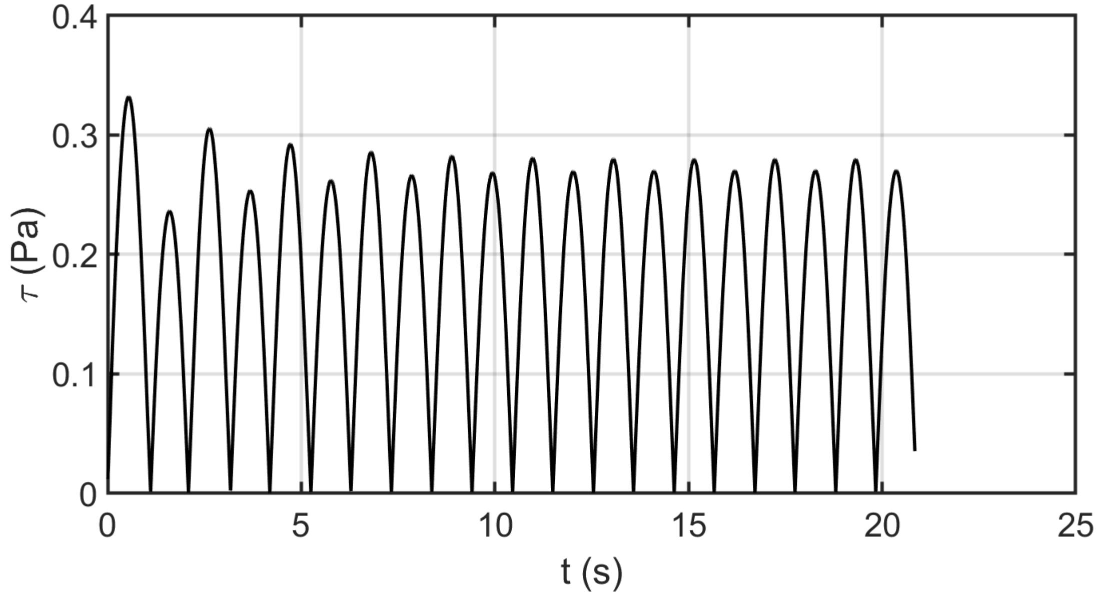

Figure 3-14. Raw upstream wave data from Run SS14 showing bottom stress vs. time

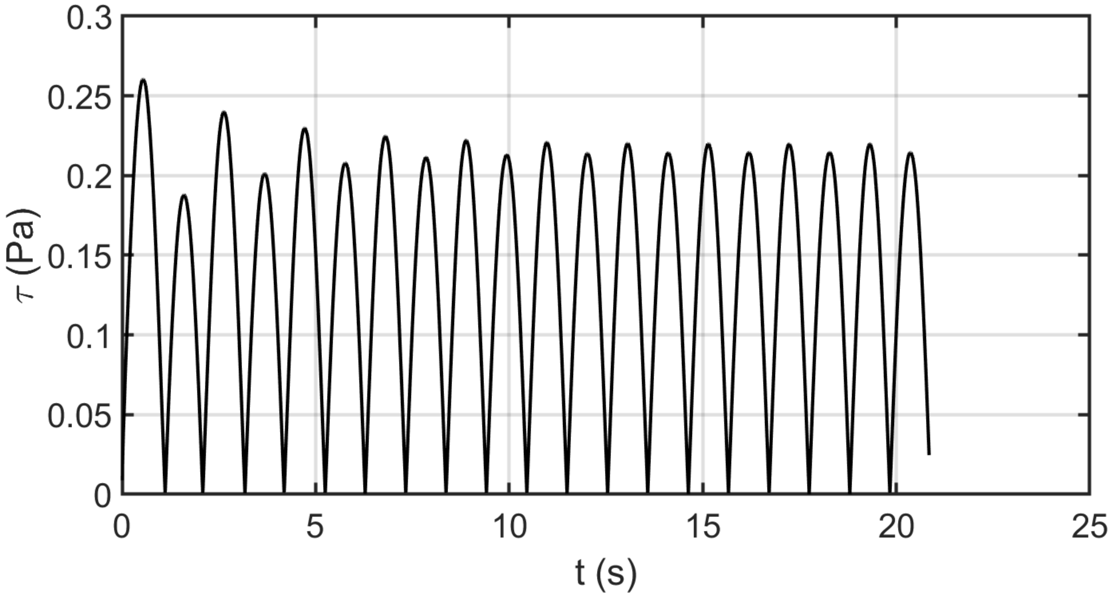

Figure 3-15. Raw upstream wave data from Run SS15 showing bottom stress vs. time

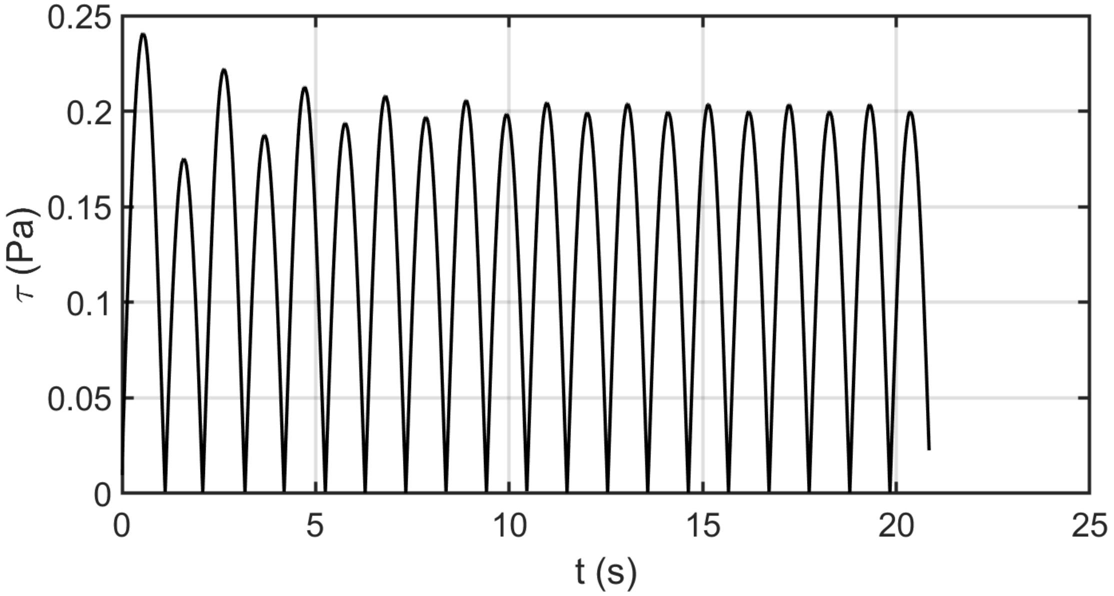

Figure 3-16. Raw upstream wave data from Run SS16 showing bottom stress vs. time

As shown in these figures, upstream wave signals were very stable during each of these runs.

3.2 Small-Scale Data Match Analysis

Maximum stress results from the last five waves crests in each wave train were averaged and plotted against experimental data. A best-fit regression line of the form y=mx+b was fit to these data. Results are shown below in Figure 3-17:

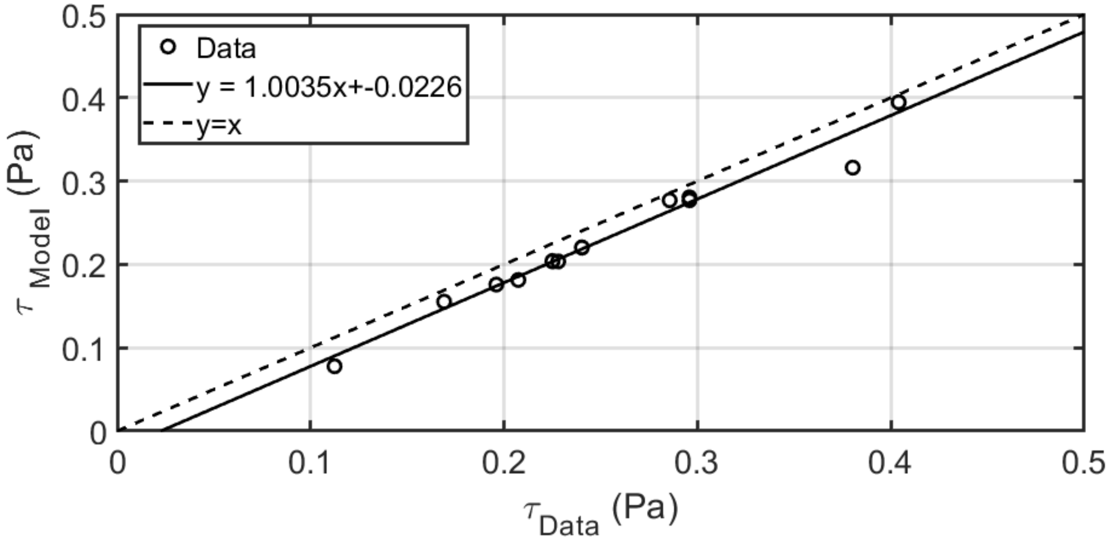

Figure 3-17. Modeled results as a function of experimental results

As shown in Figure 3-17, data were reproduced very accurately with a slope deviation of approximately 0.3% and a stress deviation of negative 0.02 pascals. However, the predicted/modeled stress was consistently lower than the measured stress values. Investigators ran a series of models where roughness coefficients were used along the bottom boundary in an attempt to improve this shift in data. Several roughness values were tried. Previous work from Crowley et al. (2014b) indicated that roughness height should be equal to 1.47 times the mean sediment diameter. Sumer and Fredsoe utilized 0.2 mm sand throughout their experiments. As such, a roughness height of approximately 0.3 mm was first used. Results from this set of runs is shown below in Fig. 3-18:

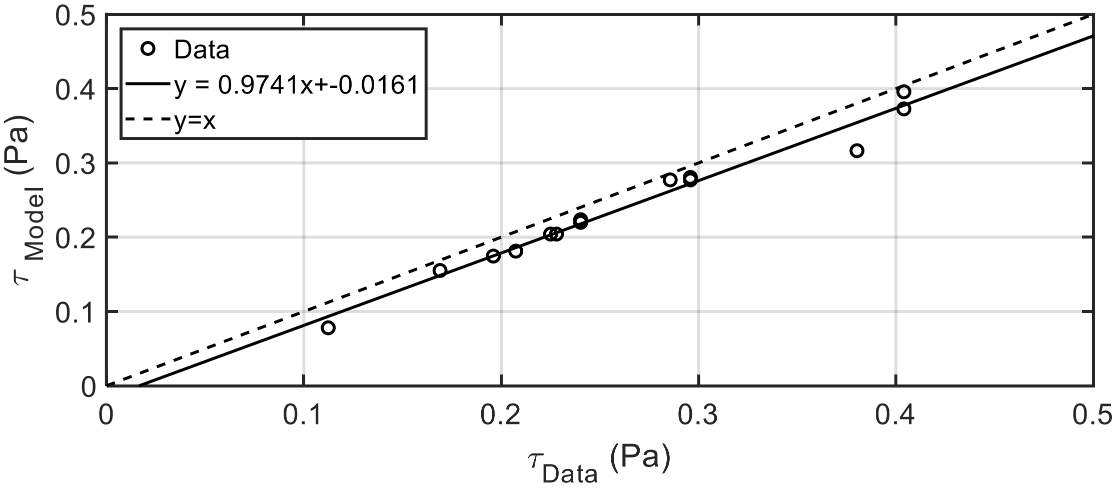

Figure 3-18. Modeled results as a function of experimental results using a roughness height of 0.3 mm

As shown in Fig. 3-18, results were very similar to smooth-walled results. Next, investigators doubled the roughness height to 0.6 mm. Results are presented below in Fig. 3-19:

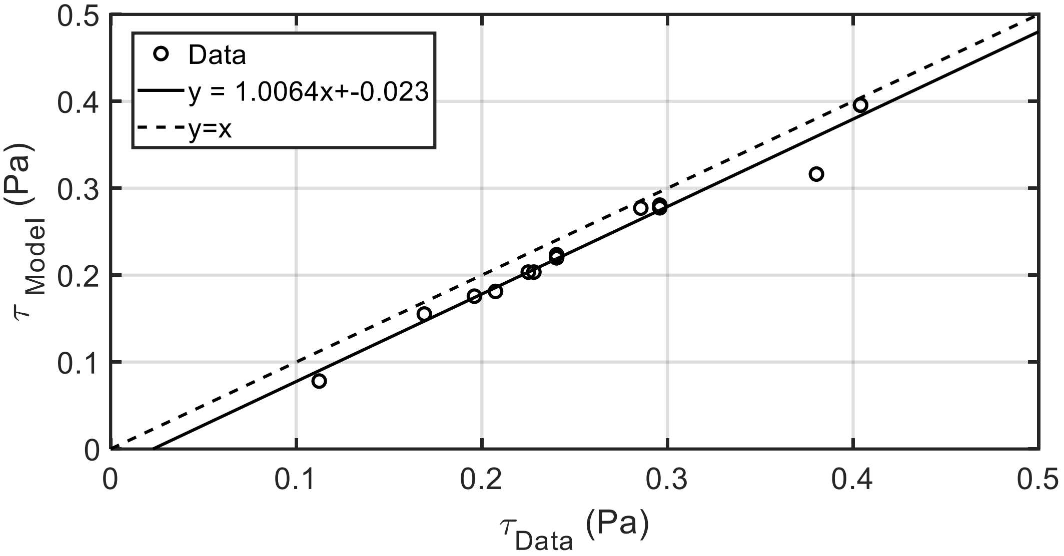

Figure 3-19. Modeled results as a function of experimental results using a roughness height of 0.6 mm

As shown, results were again, almost identical to smooth-walled results – the slope deviation was 0.6% and the stress deviation was approximately 0.02 pascals.

3.3 Sensitivity Analysis

Based upon results investigators concluded that to exactly match the y=x line between experimental and modeled data, it was likely that the model would need to be remeshed and that roughness had little effect on results. However, further analysis of the mechanics associated with erosion function testing indicate that such a reanalysis is not necessary from a practical perspective. Consider a typical RETA dataset – the Jewfish Creek data for example – presented below in Fig. 3-20:

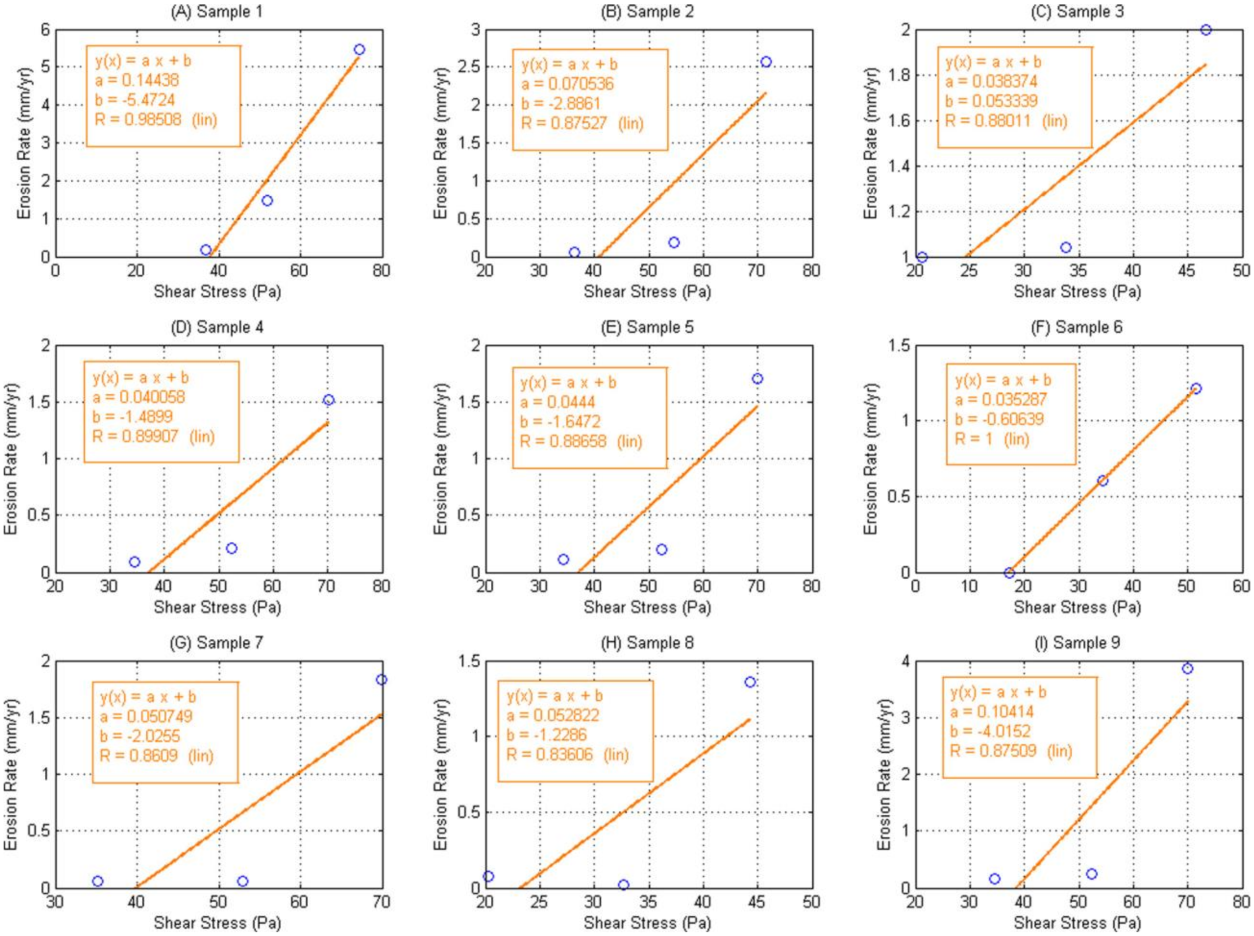

Figure 3-20. RETA-generated erosion functions from Jewfish Creek; from Bloomquist et al. (2012b)

As shown, the slope between the erosion rate/shear stress best-fit line varies between 0.03 mm/year-Pa and 0.14 mm/year-Pa. If one examines the worst-case erosion function from the above (the top-left erosion function with a slope of 0.144 mm/year-Pa), its best-fit regression line is:

$$E = 0.14438\tau - 5.4724 \tag{3-1}$$

where E is erosion and τ is shear stress. Substituting an uncertainty of $\pm 0.02\ Pa$ yields:

$$E = 0.14438(\pm 0.02) - 5.4724 = \pm 0.003 \text{ mm/year} \tag{3-2}$$

This 0.003 mm/year of deviation would appear to be relatively insignificant from a design perspective. Results are even more encouraging for SERF implementation. As Crowley et al. (2014b) showed, there is significant stress variability on a specimen during a SERF test as shown below in Fig. 3-21 and Fig. 3-22:

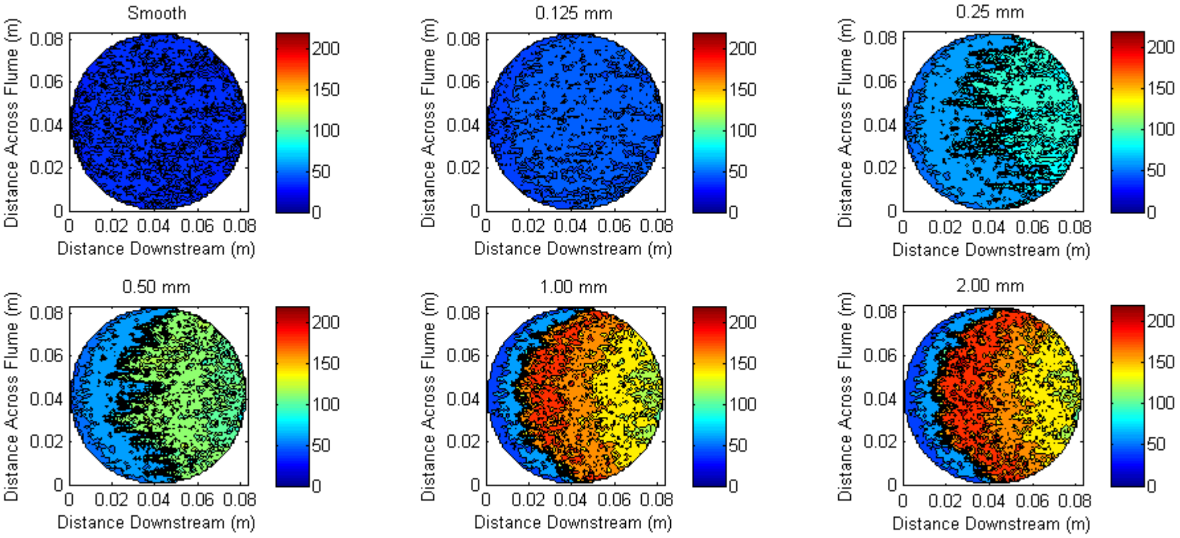

Figure 3-21. Modeled top view of bottom stress on the surface of a SERF specimen for varying roughnesses using a representative worst-case 5 m/s velocity; from Crowley et al. (2014b)

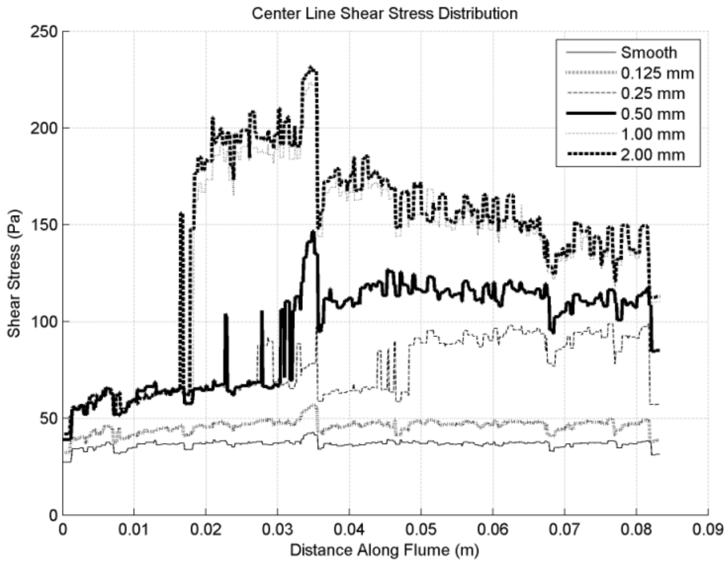

Figure 3-22. Cross-sectional view of velocity through the center of typical SERF specimens using a representative worst-case 5 m/s flow velocity (from Crowley et al. 2012)

As shown in Figure 3-21 and Figure 3-22, when rough specimens (on the order of 0.25 mm mean diameter sediments or greater) are tested in the SERF, shear stress across the specimen surface may vary by as much as 100%. Taking the 0.25 mm roughness specimen, for example, Figure 3-21 and Figure 3-22 show that stress may be as low as ~25 Pa near the upstream edge of the specimen. As one moves downstream, this stress may approach 100 Pa or greater. This variability explains why SERF specimens never erode uniformly and their downstream edges tend to erode faster than their upstream portions.

The implication of these tests is that cohesive specimens, whose surfaces also become very rough as they erode, behave similarly. Over time during a SERF test, this issue tends to continually worsen as specimens become increasingly rough due to differential erosion. As such, the concept of an average shear stress during a SERF test is relatively meaningless. Due to this stress variability, the best practice during SERF testing is to obtain very conservative results by ensuring that the back edge of an eroding specimen is approximately level with the bottom of the flume. Of course, this causes the front edge of the specimen to protrude into the flume where it is subjected to normal flow stresses. Thus, SERF results are very conservative. In this context, an underestimation of 0.02 Pa associated with the parametric data fits above would appear to be relatively unimportant and indicated that the smooth-walled data should be sufficient for analysis.

3.4 Small-Scale Amplified Stress Data

Amplified maximum stress magnitude data from small-scale runs are shown below from Fig. 3-23 through Fig. 3-38:

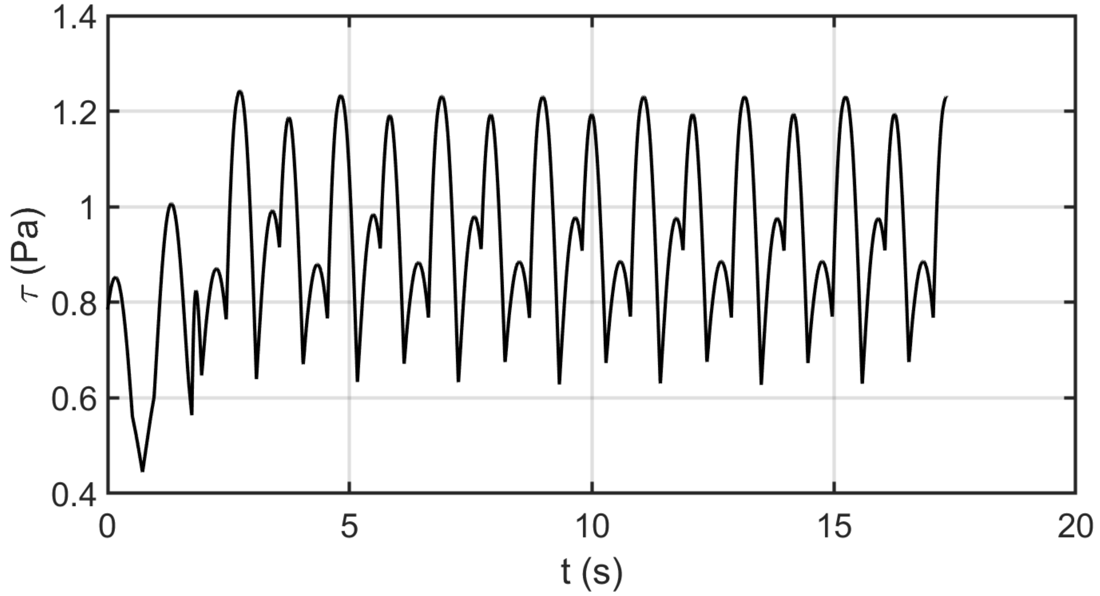

Figure 3-23. Amplified stress data from Run SS1

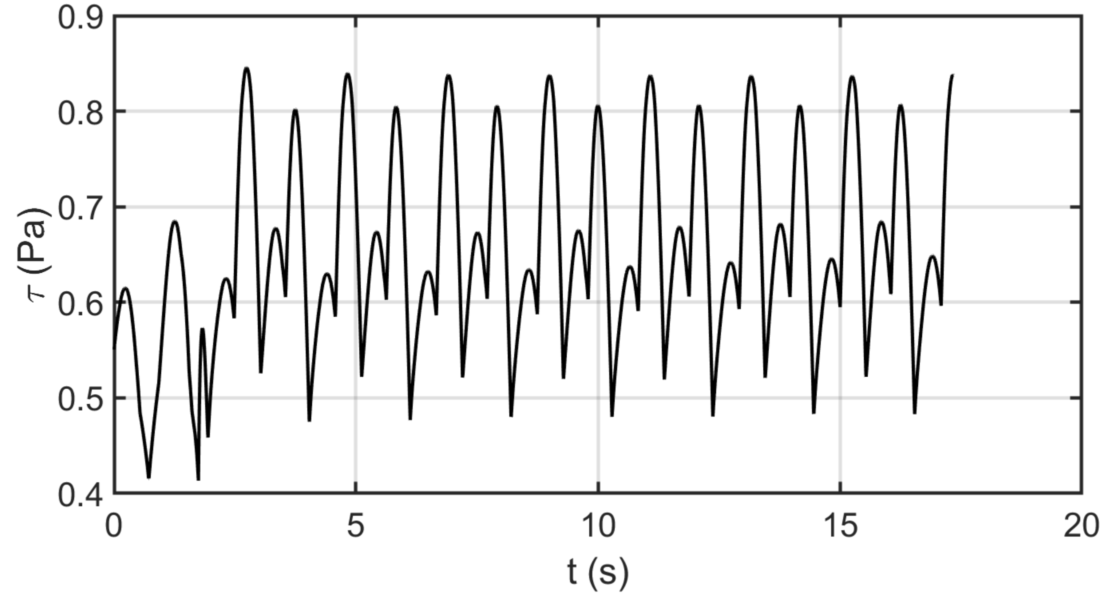

Figure 3-24. Amplified stress data from Run SS2

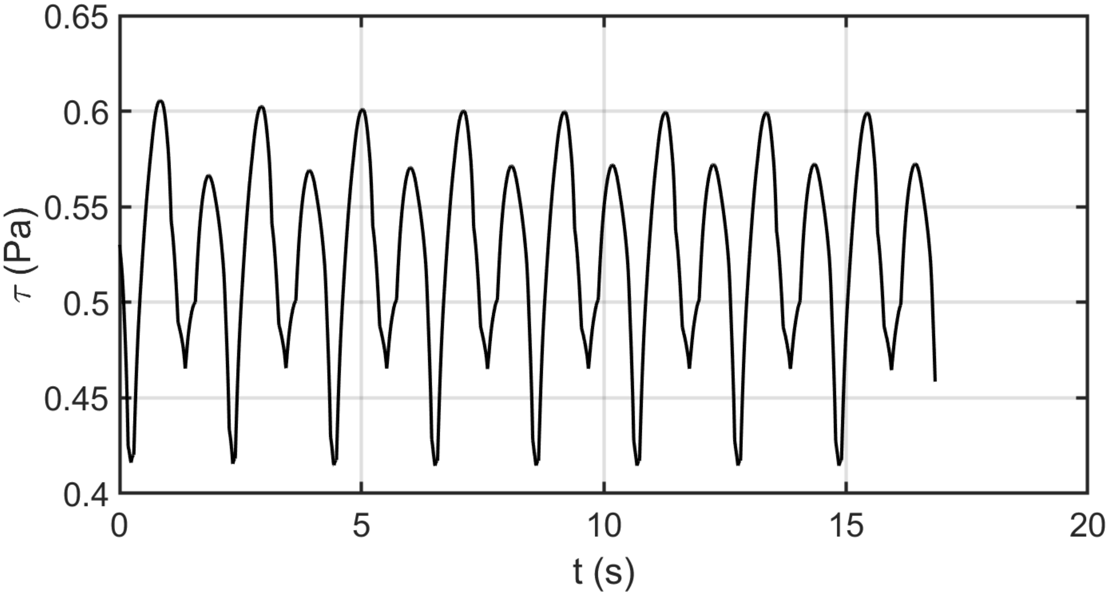

Figure 3-25. Amplified stress data from Run SS3

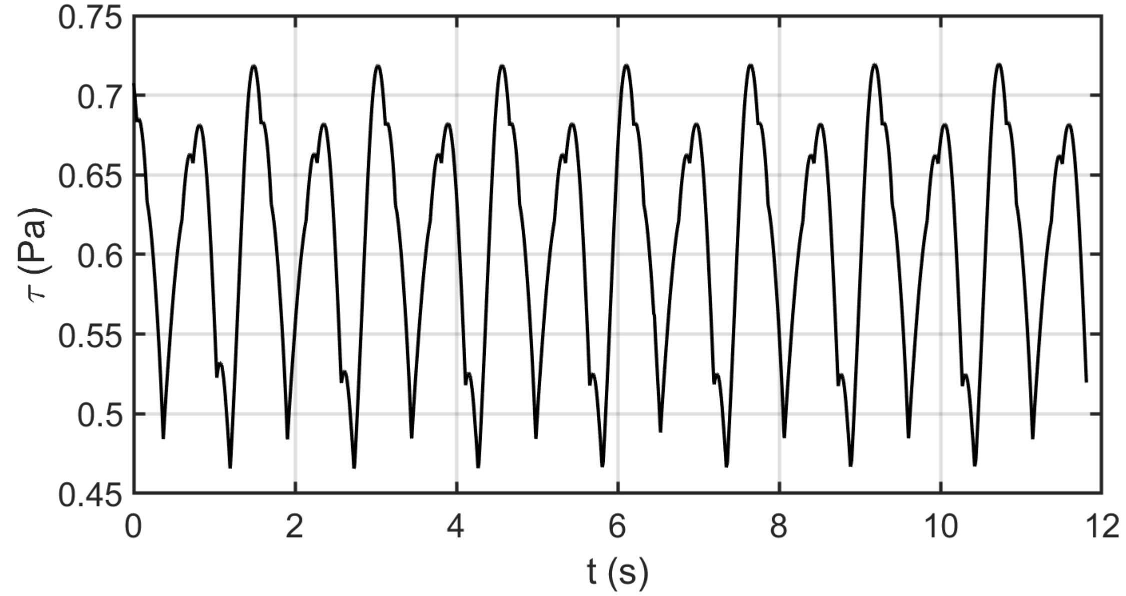

Figure 3-26. Amplified stress data from Run SS4

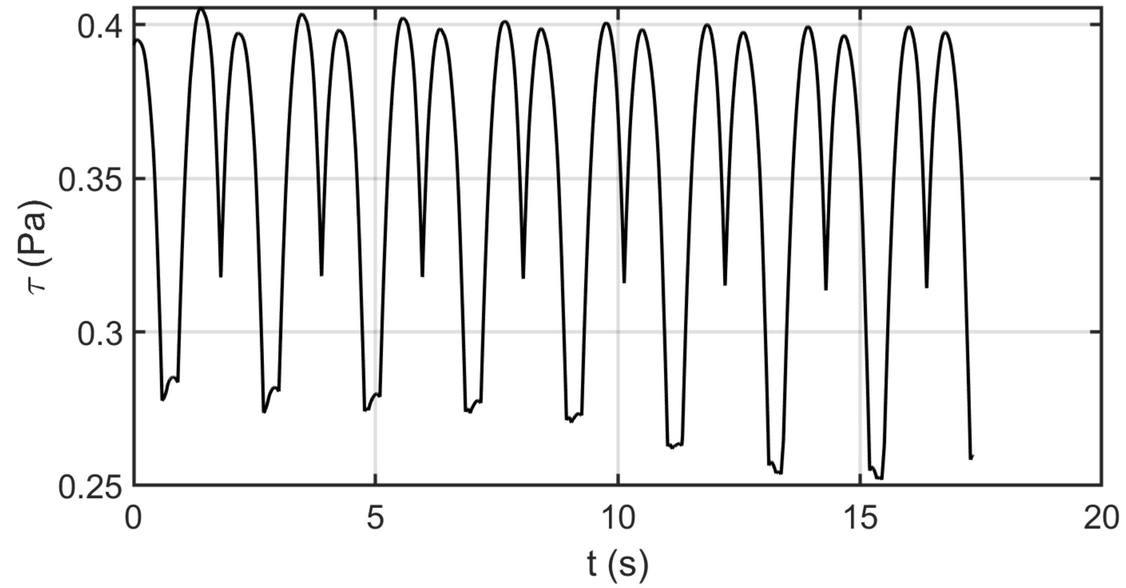

Figure 3-27. Amplified stress data from Run SS5

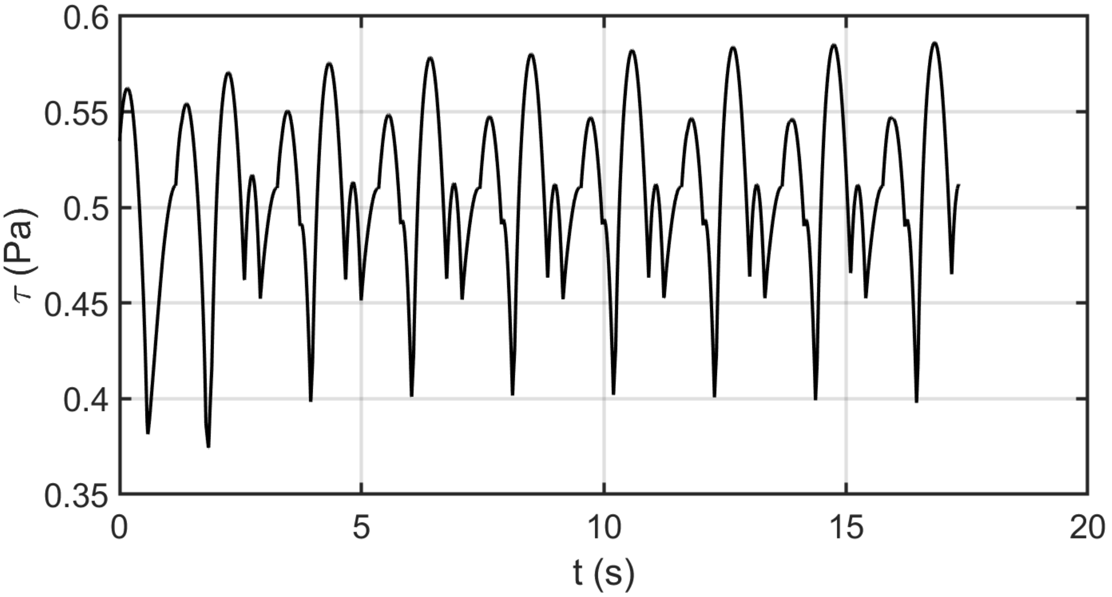

Figure 3-28. Amplified stress data from Run SS6

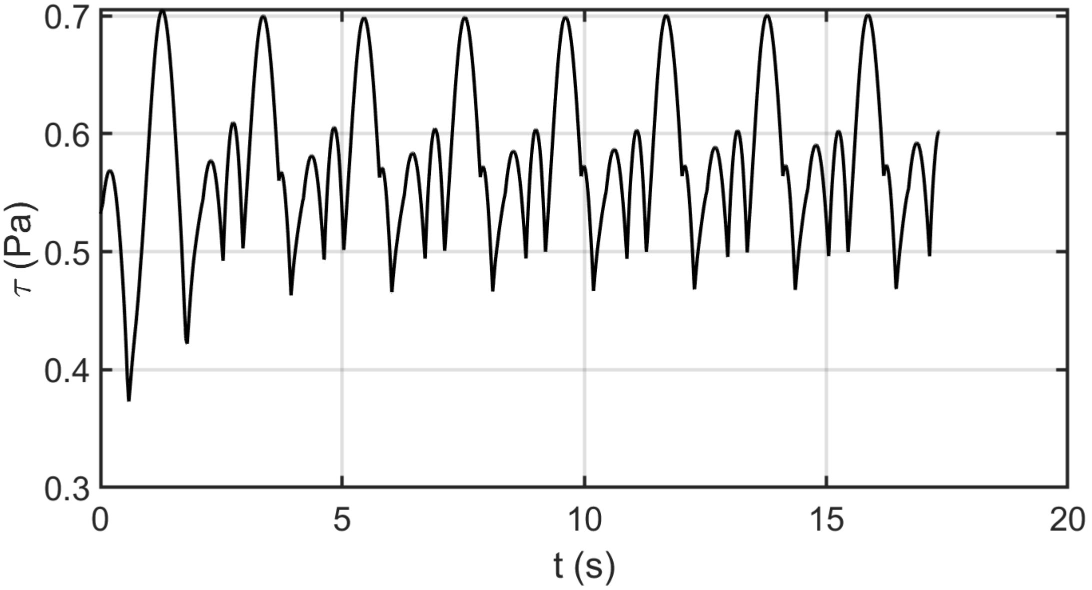

Figure 3-29. Amplified stress data from Run SS7

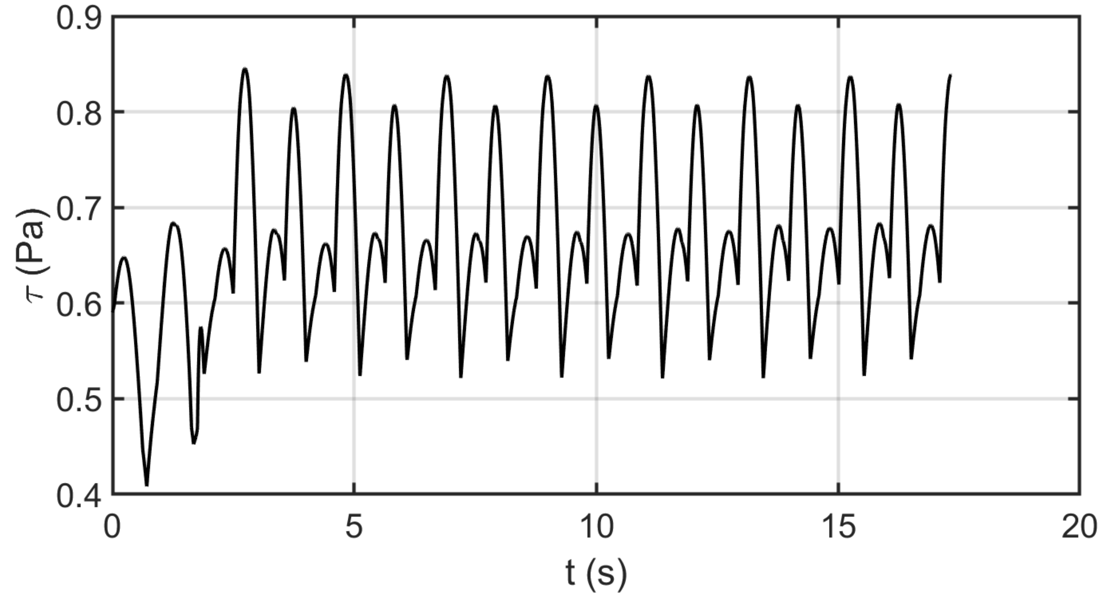

Figure 3-30. Amplified stress data from Run SS8

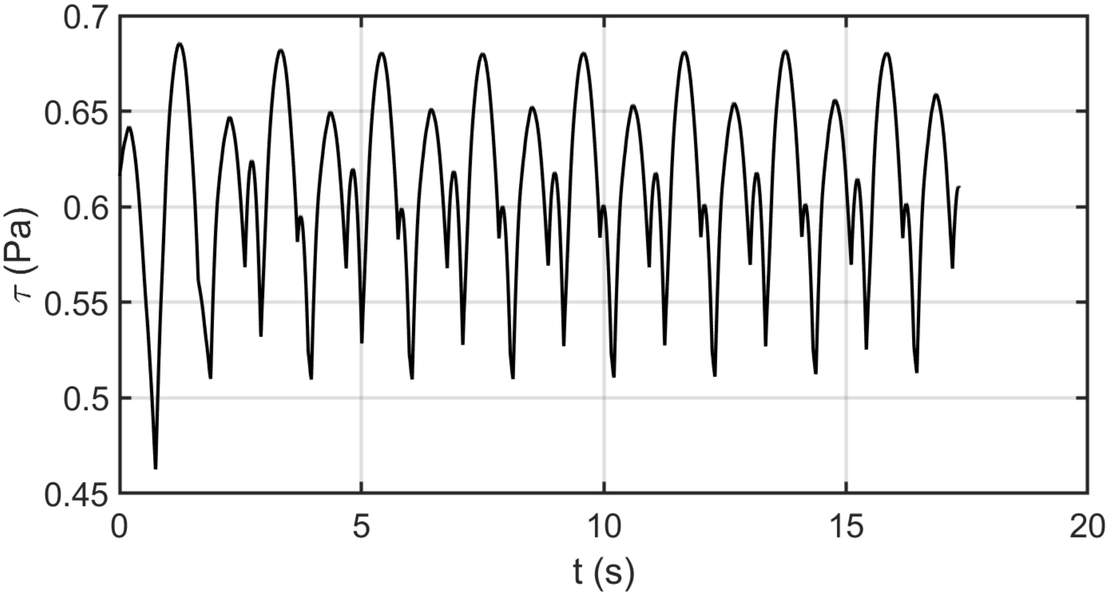

Figure 3-31. Amplified stress data from Run SS9

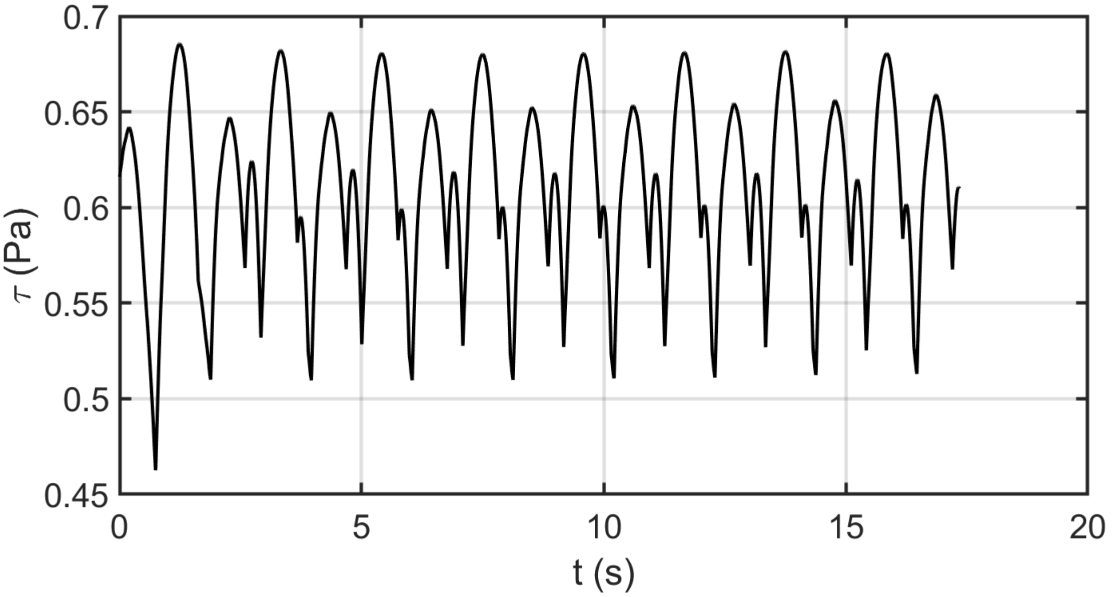

Figure 3-32. Amplified stress data from Run SS10

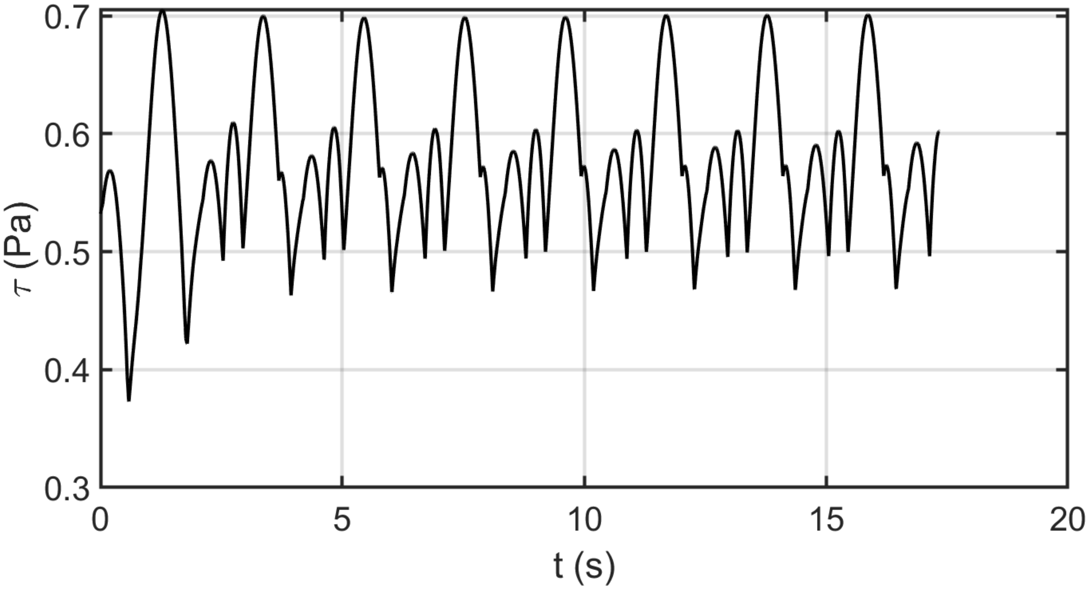

Figure 3-33. Amplified stress data from Run SS11

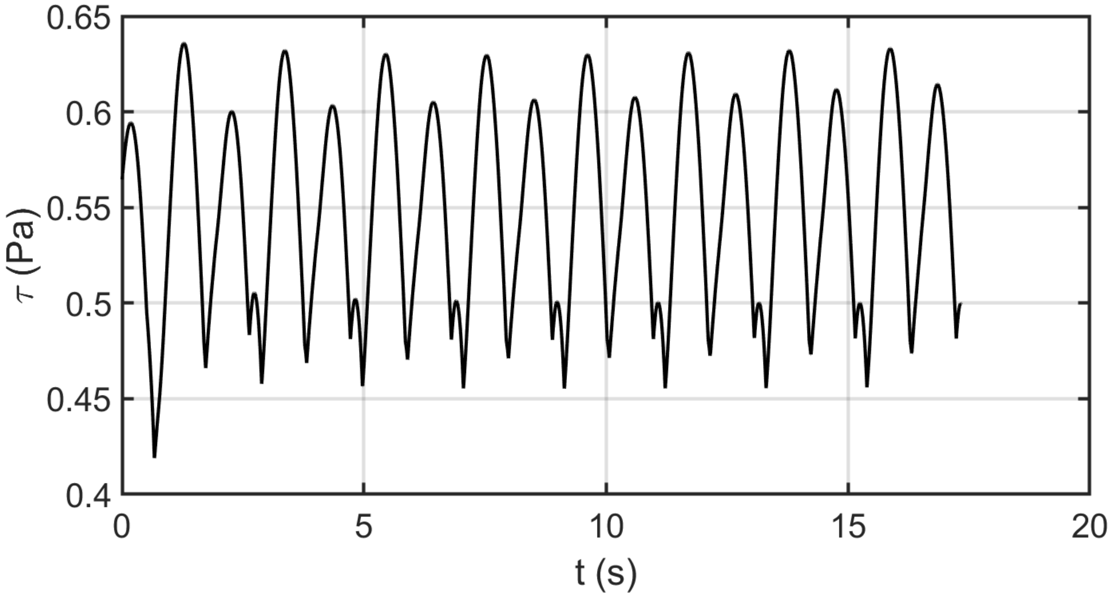

Figure 3-34. Amplified stress data from Run SS12

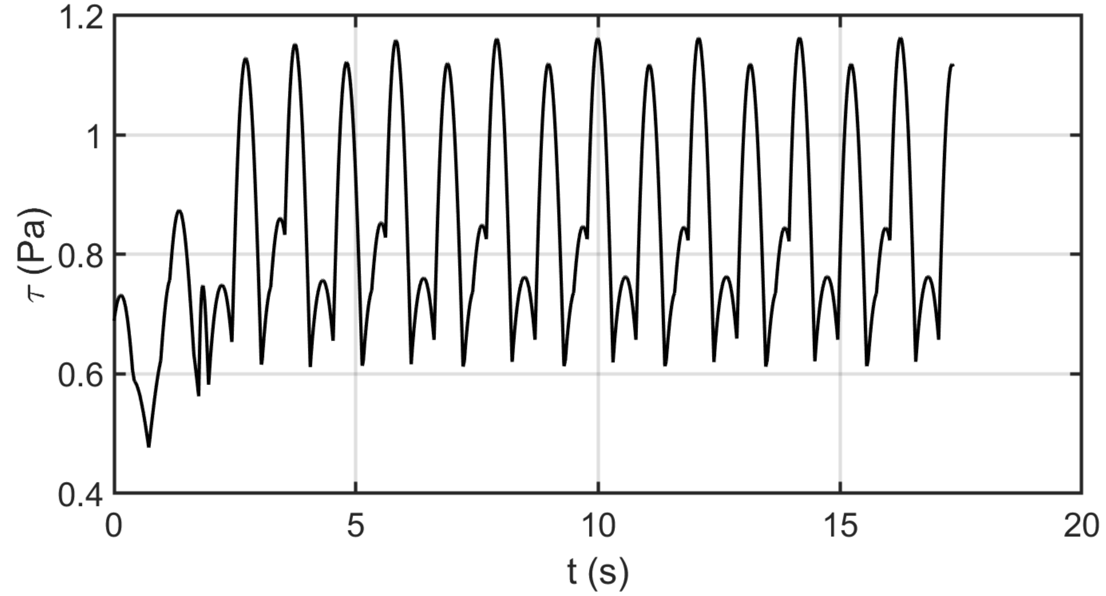

Figure 3-35. Amplified stress data from Run SS13

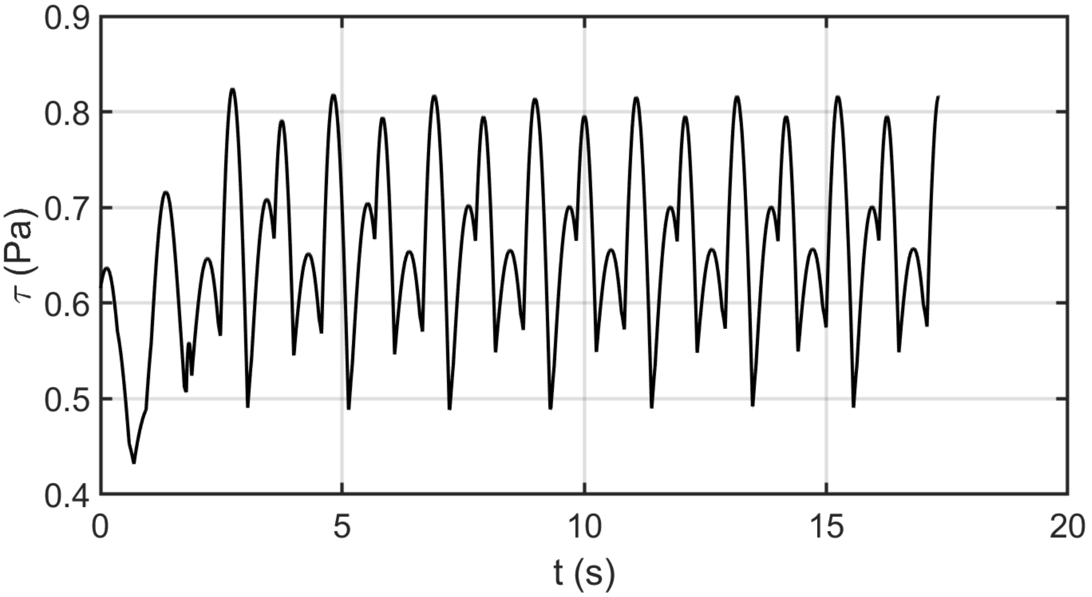

Figure 3-36. Amplified stress data from Run SS14

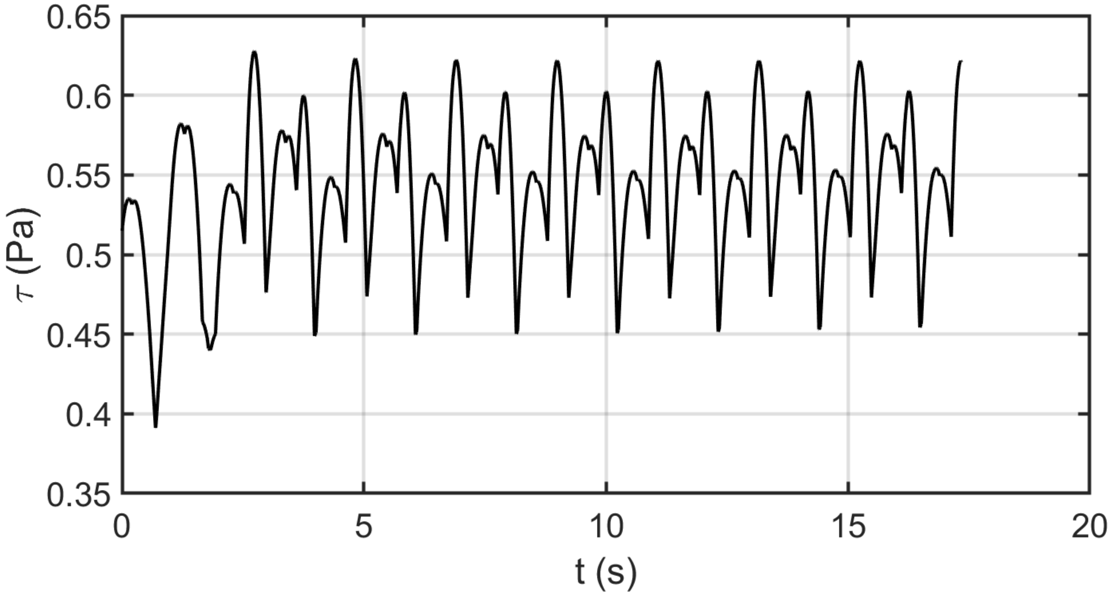

Figure 3-37. Amplified stress data from Run SS15

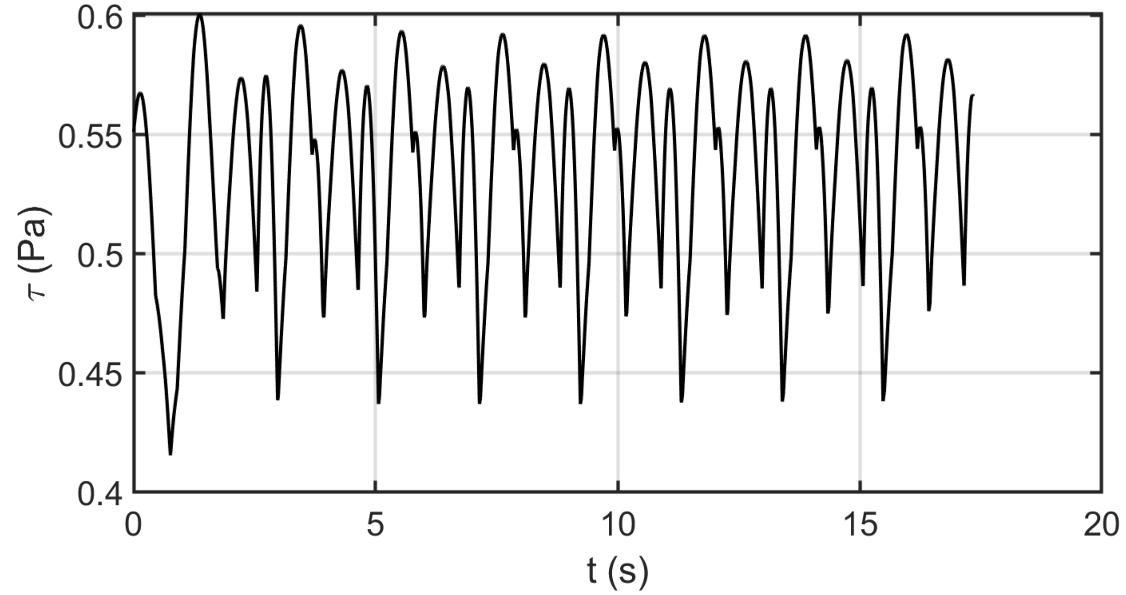

Figure 3-38. Amplified stress data from Run SS16

3.5 Large-Scale Results

Amplified stress data from the large-scale simulations are presented below in Figure 3-39 through Figure 3-74:

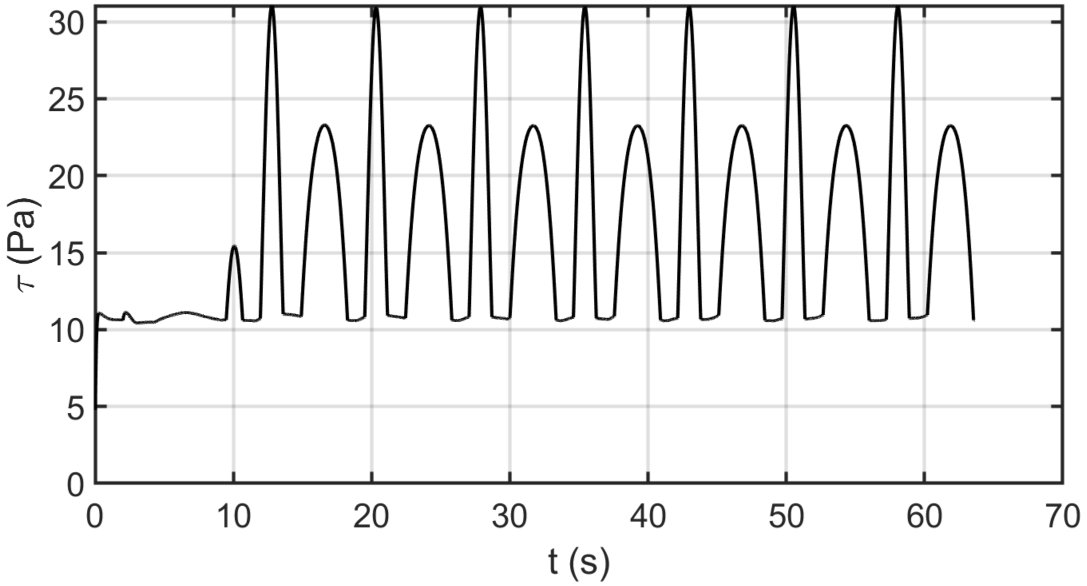

Figure 3-39. Large-scale amplified stress data from Run LS1

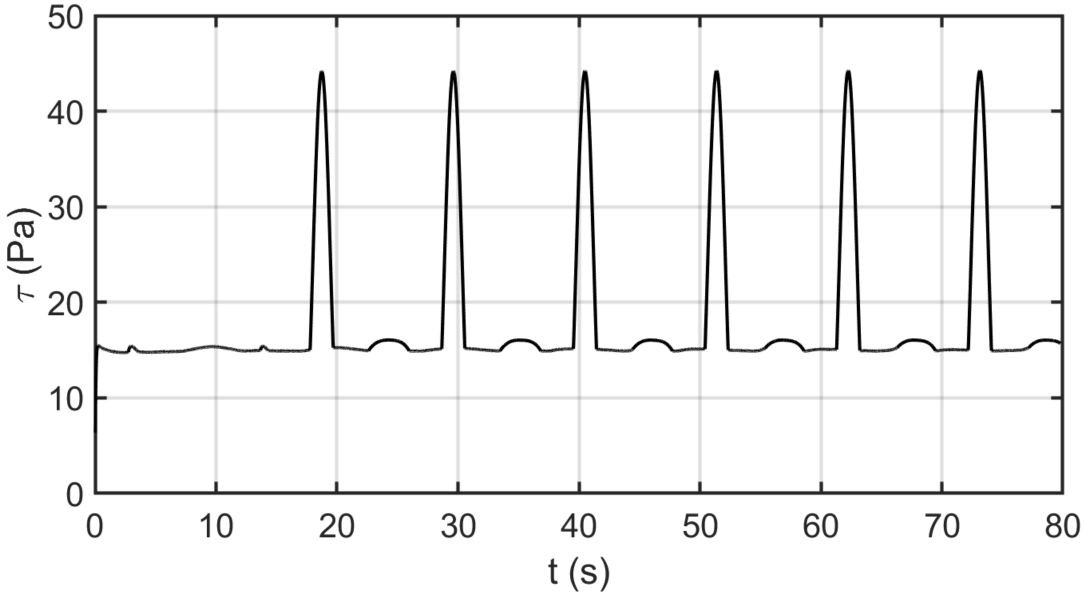

Figure 3-40. Large-scale amplified stress data from Run LS2

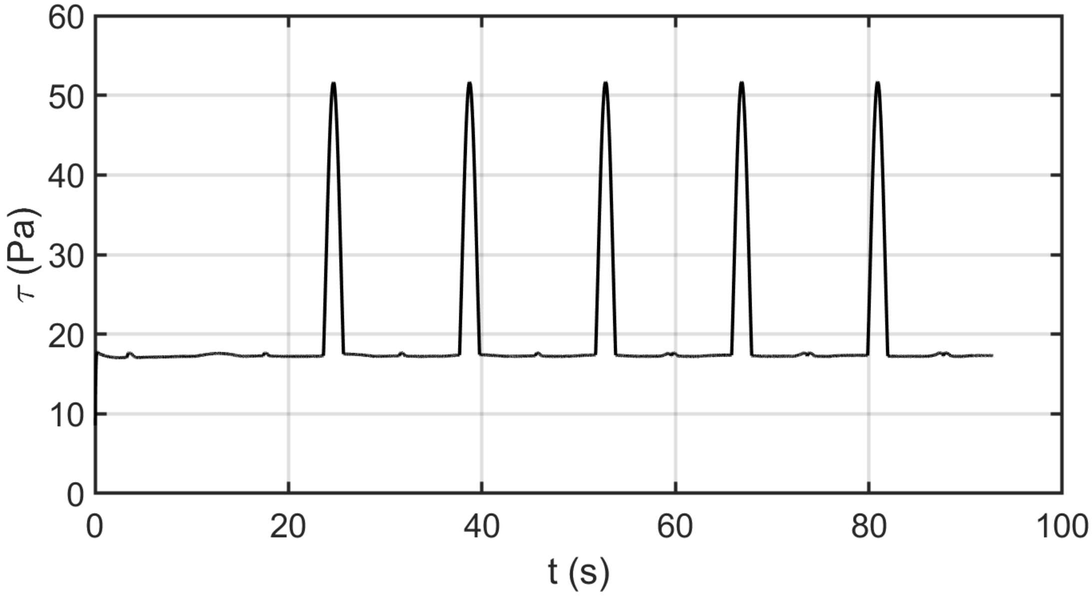

Figure 3-41. Large-scale amplified stress data from Run LS3

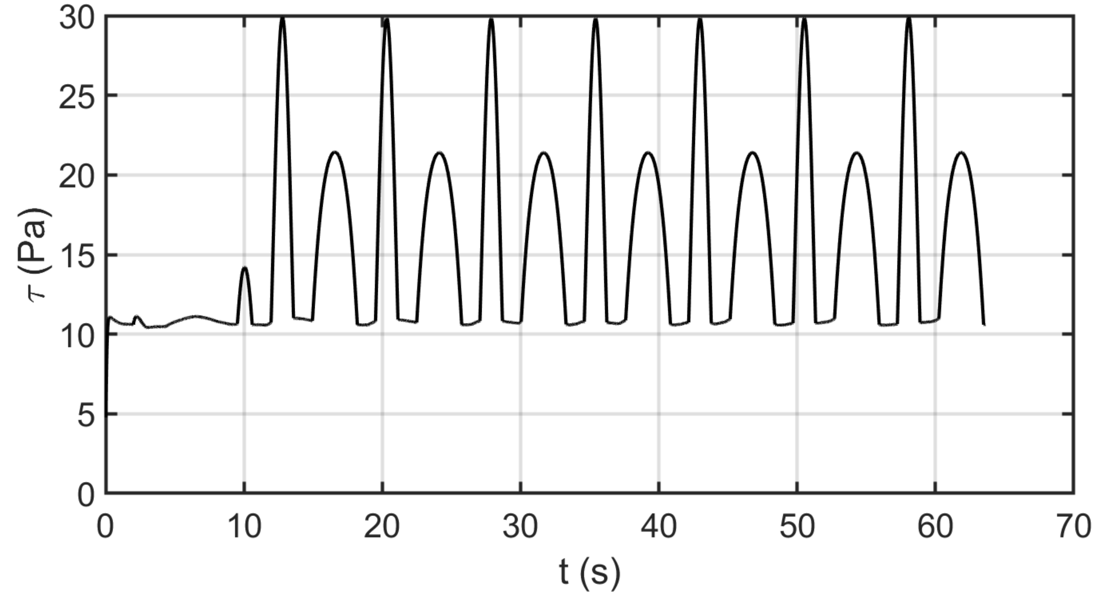

Figure 3-42. Large-scale amplified stress data from Run LS4

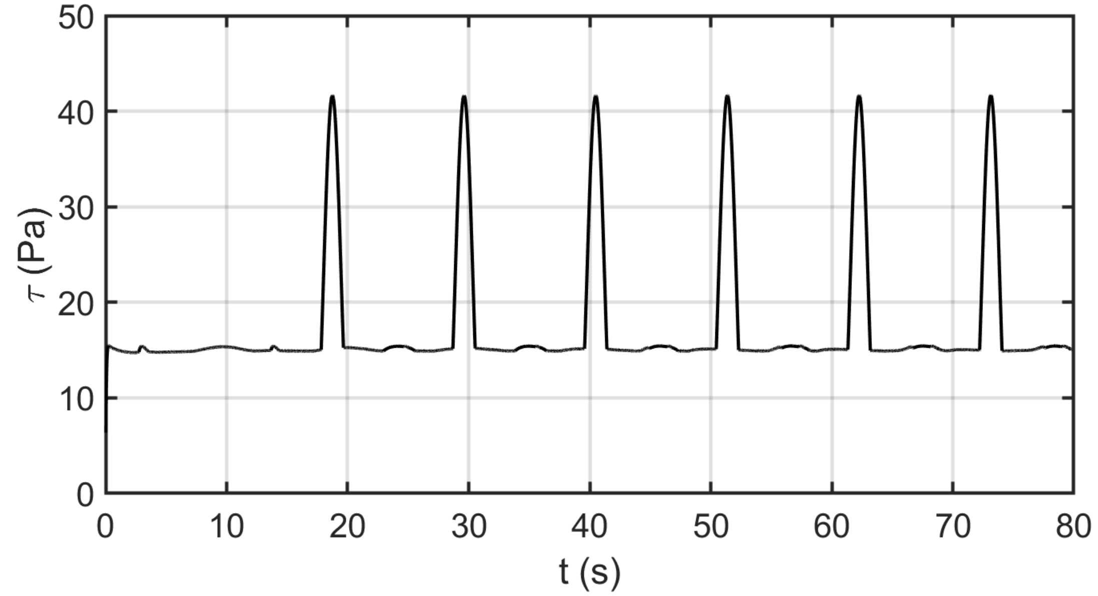

Figure 3-43. Large-scale amplified stress data from Run LS5

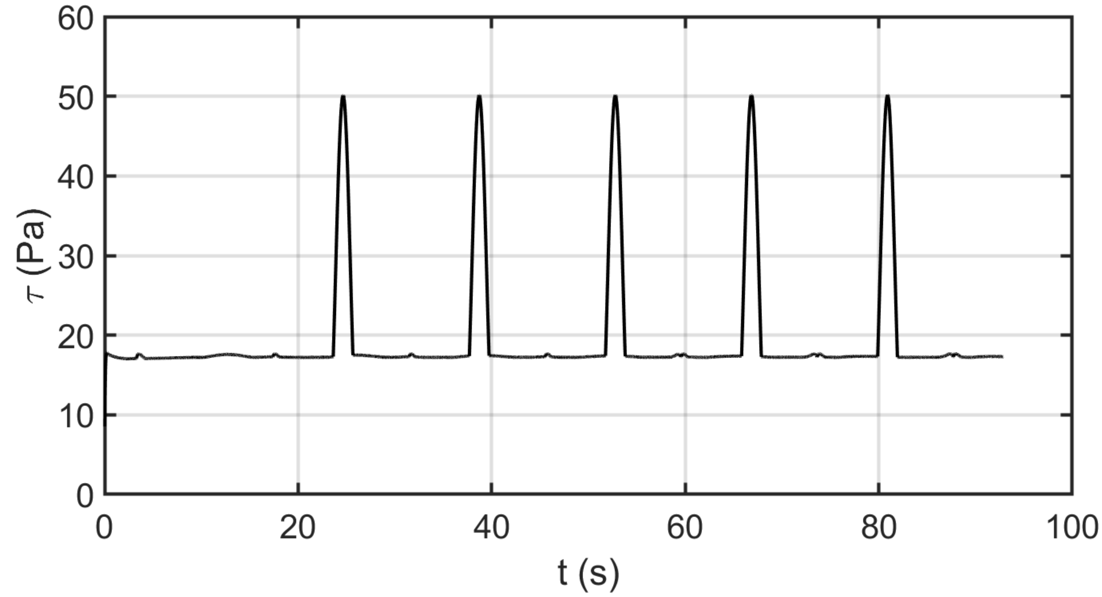

Figure 3-44. Large-scale amplified stress data from Run LS6

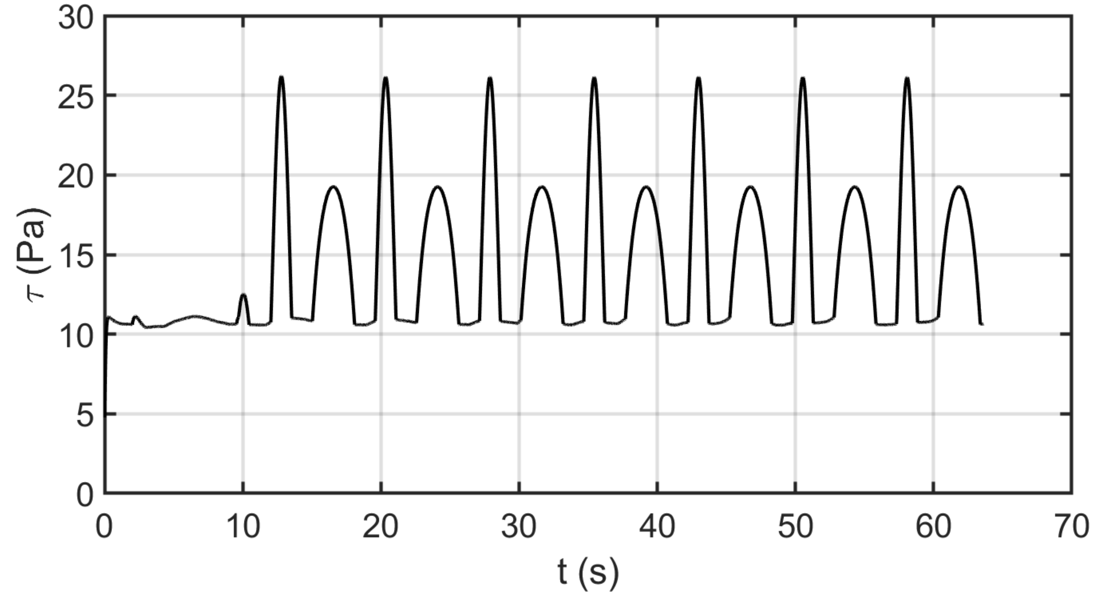

Figure 3-45. Large-scale amplified stress data from Run LS7

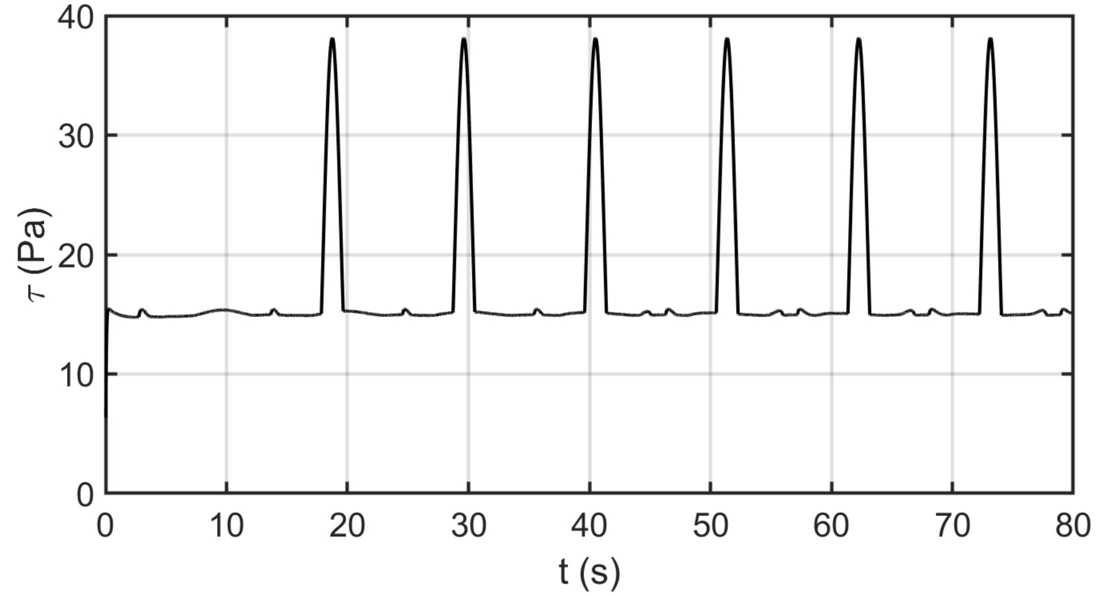

Figure 3-46. Large-scale amplified stress data from Run LS8

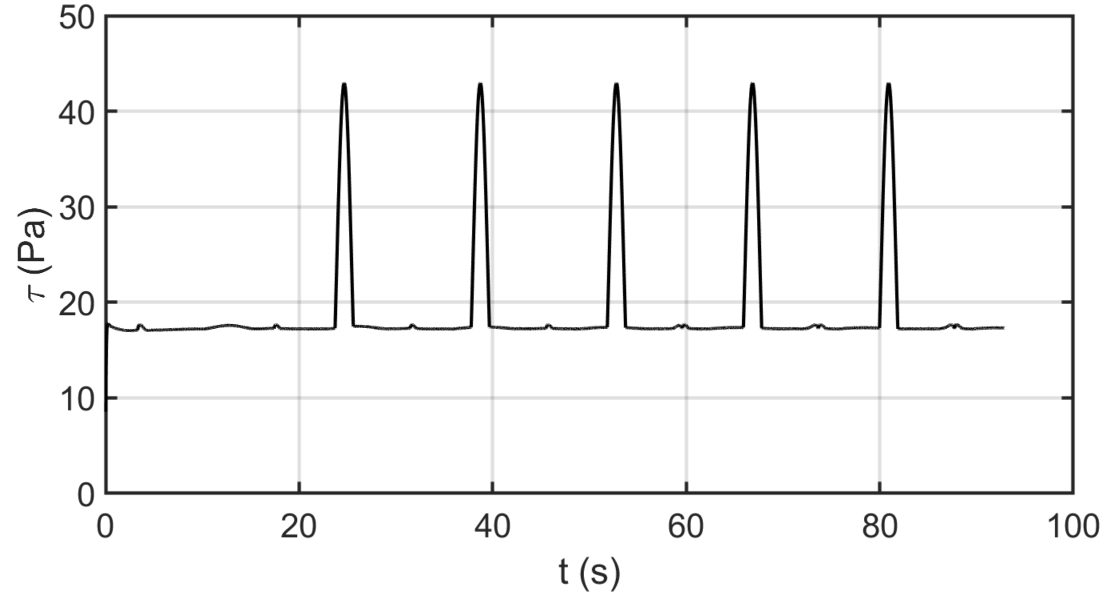

Figure 3-47. Large-scale amplified stress data from Run LS9

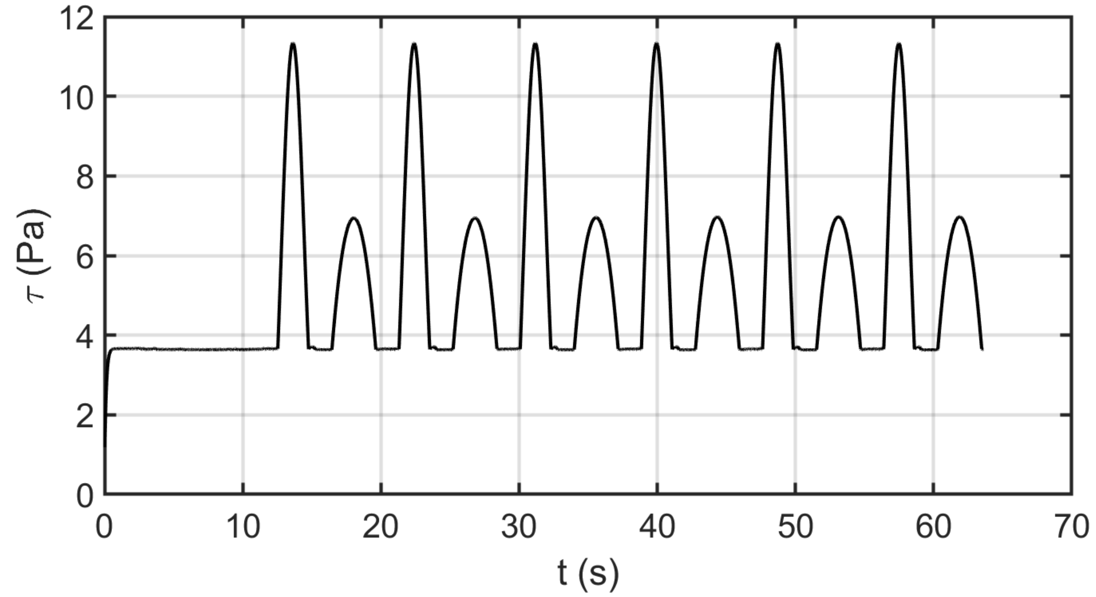

Figure 3-48. Large-scale amplified stress data from Run LS10

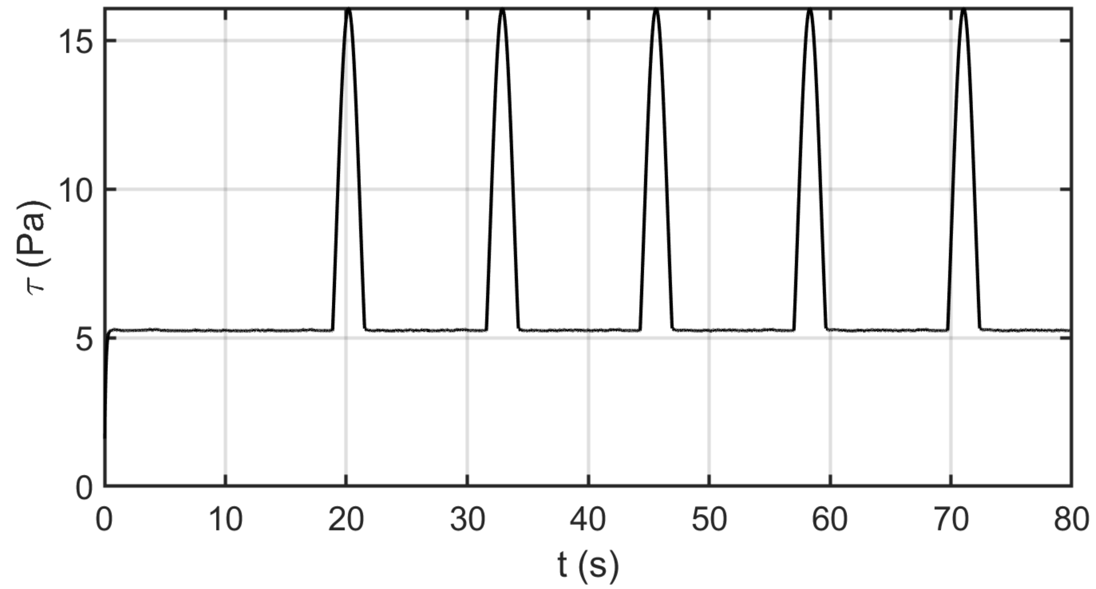

Figure 3-49. Large-scale amplified stress data from Run LS11

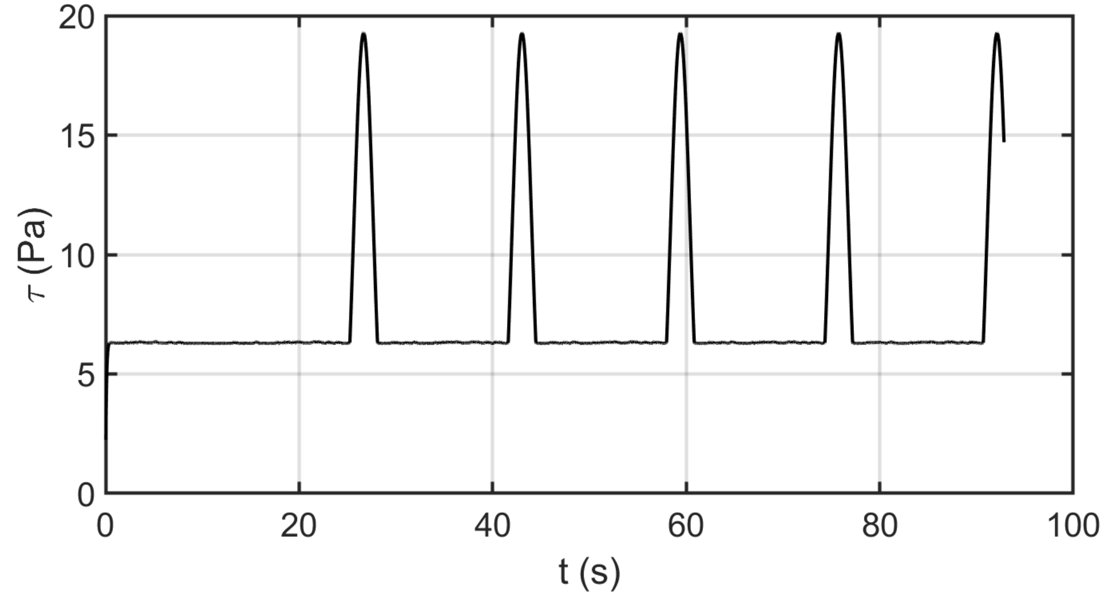

Figure 3-50. Large-scale amplified stress data from Run LS12

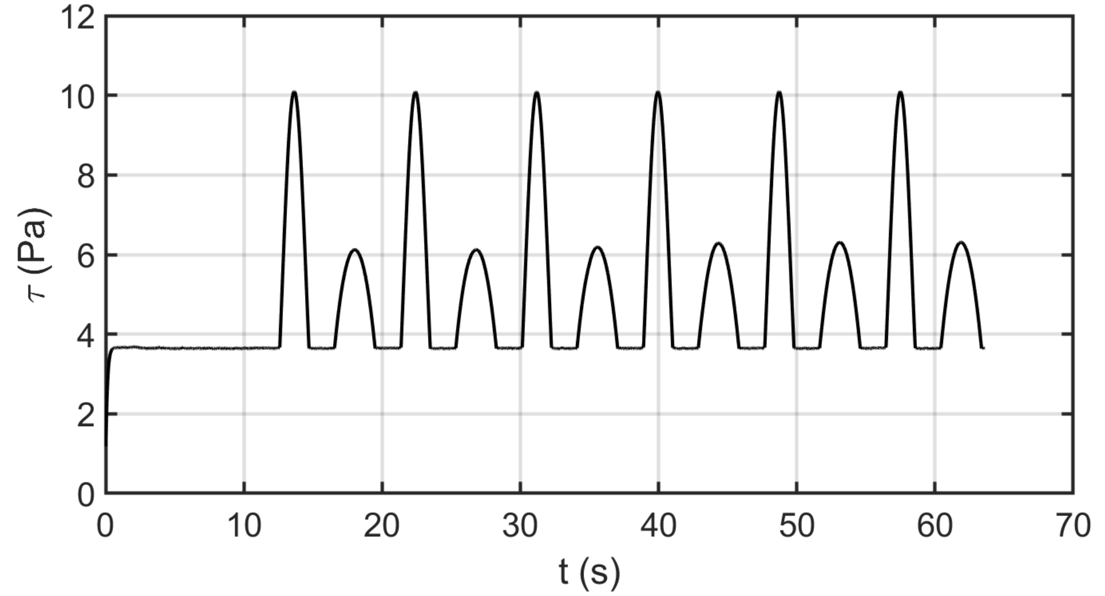

Figure 3-51. Large-scale amplified stress data from Run LS13

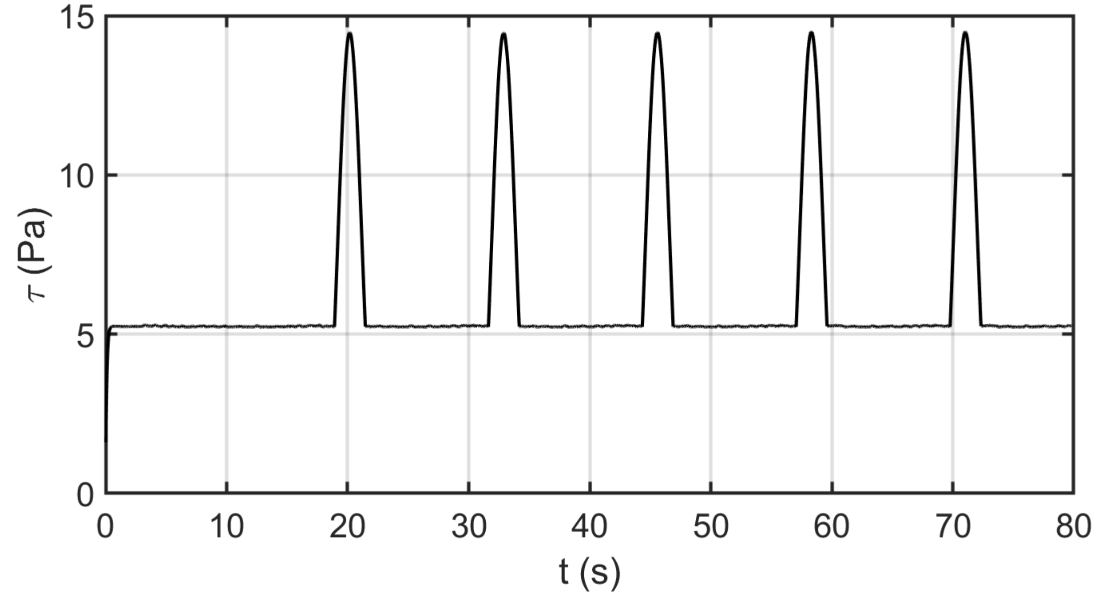

Figure 3-52. Large-scale amplified stress data from Run LS14

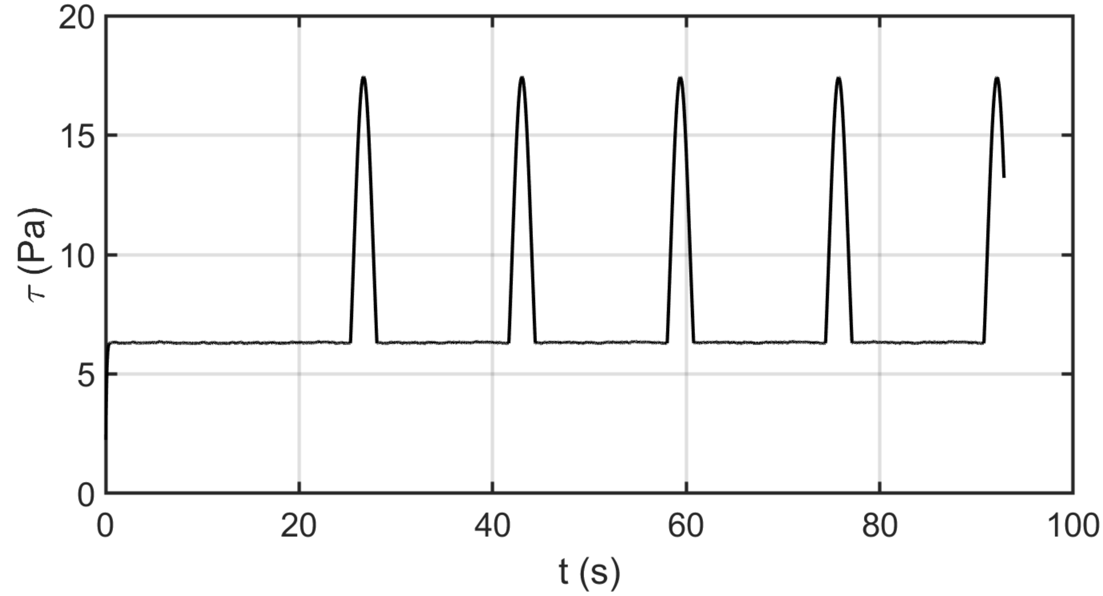

Figure 3-53. Large-scale amplified stress data from Run LS15

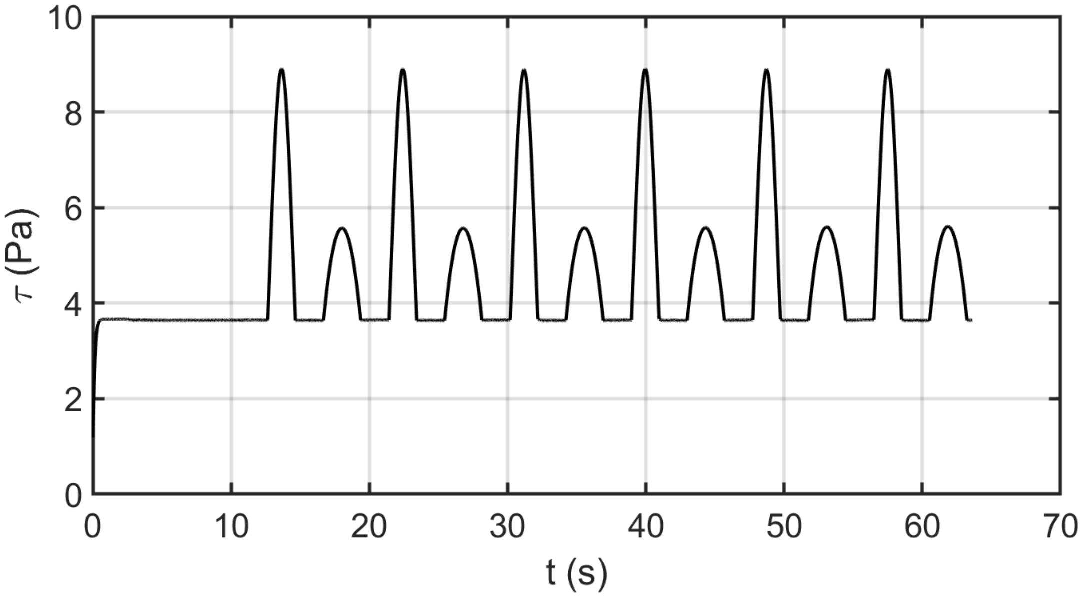

Figure 3-54. Large-scale amplified stress data from Run LS16

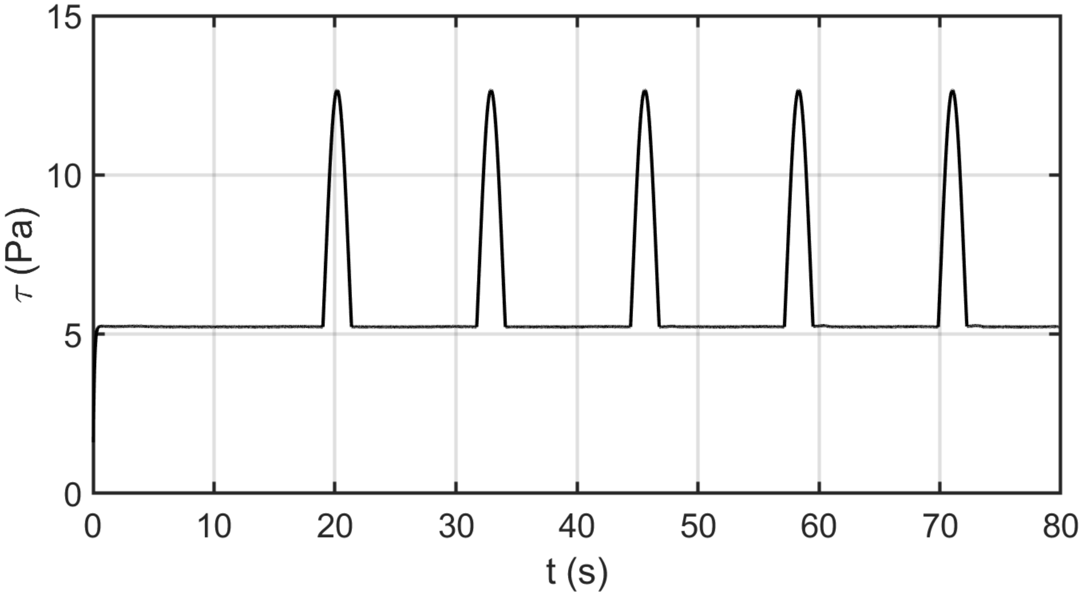

Figure 3-55. Large-scale amplified stress data from Run LS17

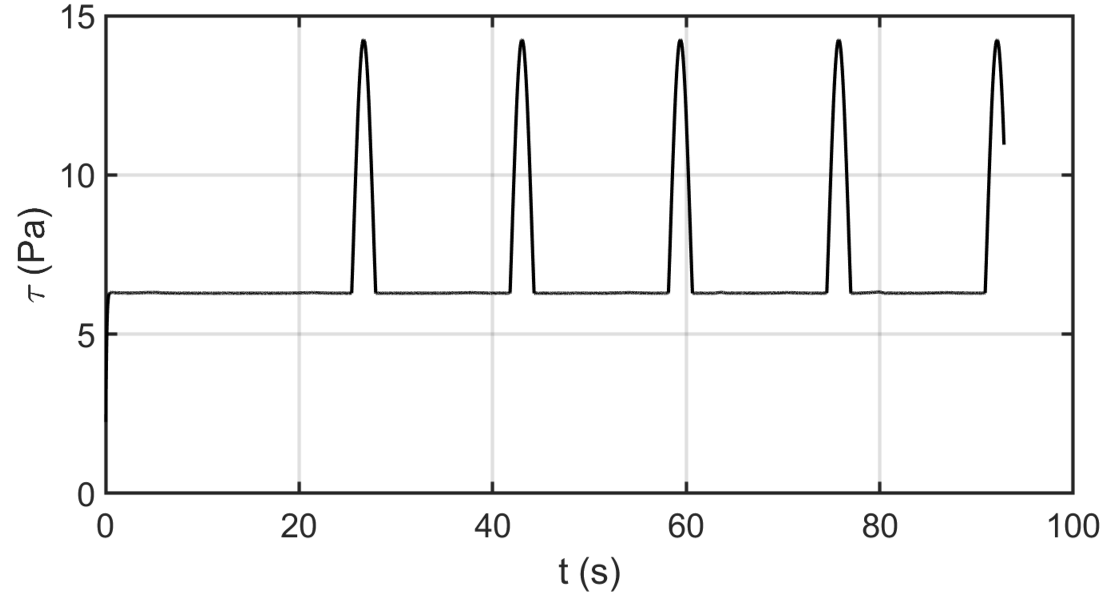

Figure 3-56. Large-scale amplified stress data from Run LS18

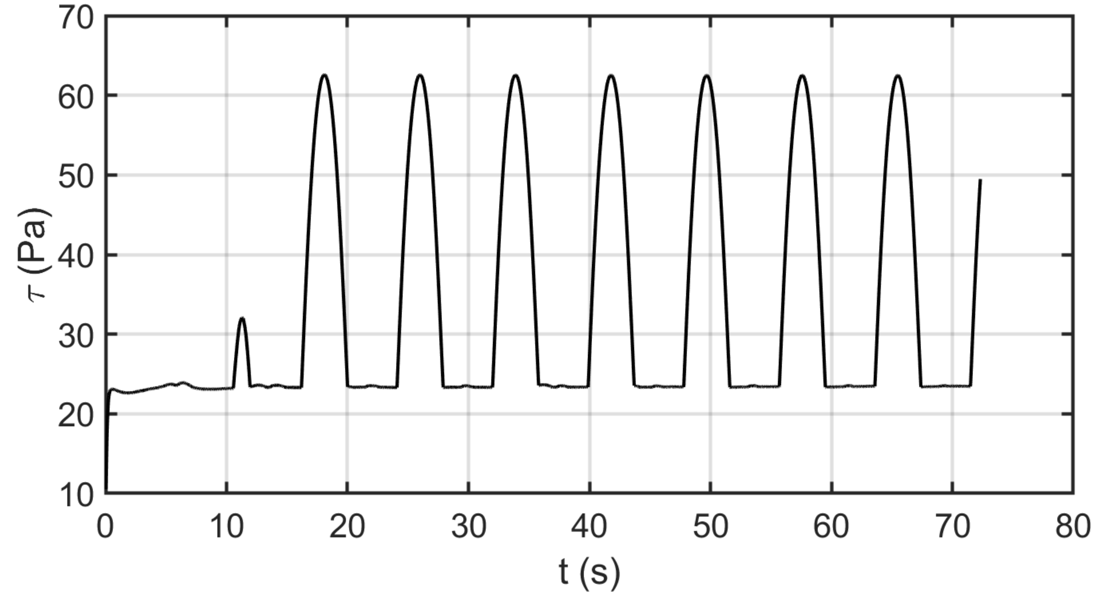

Figure 3-57. Large-scale amplified stress data from Run LS19

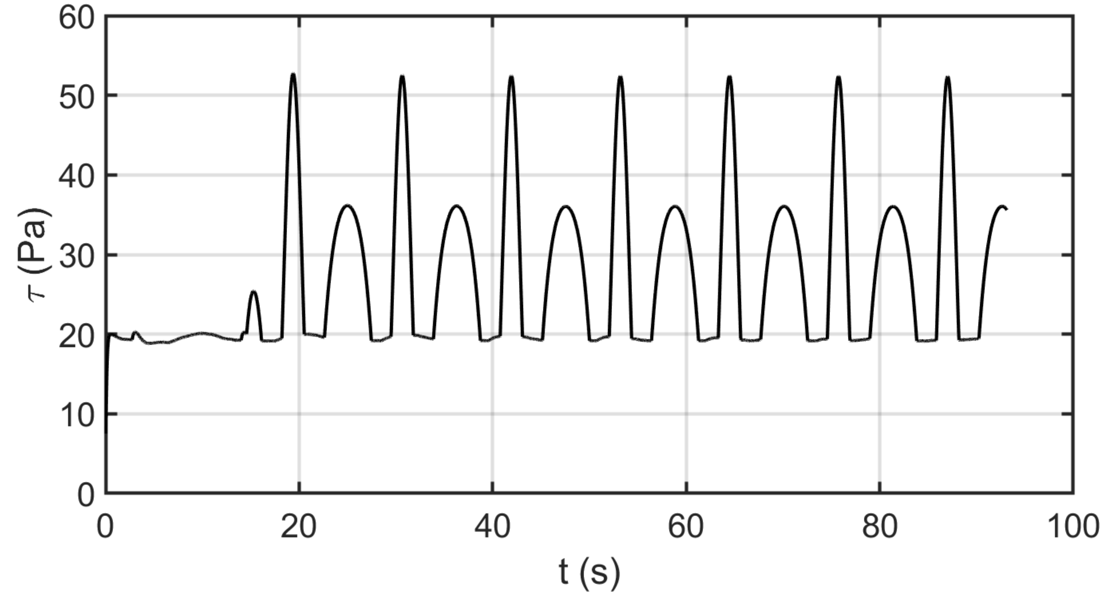

Figure 3-58. Large-scale amplified stress data from Run LS20

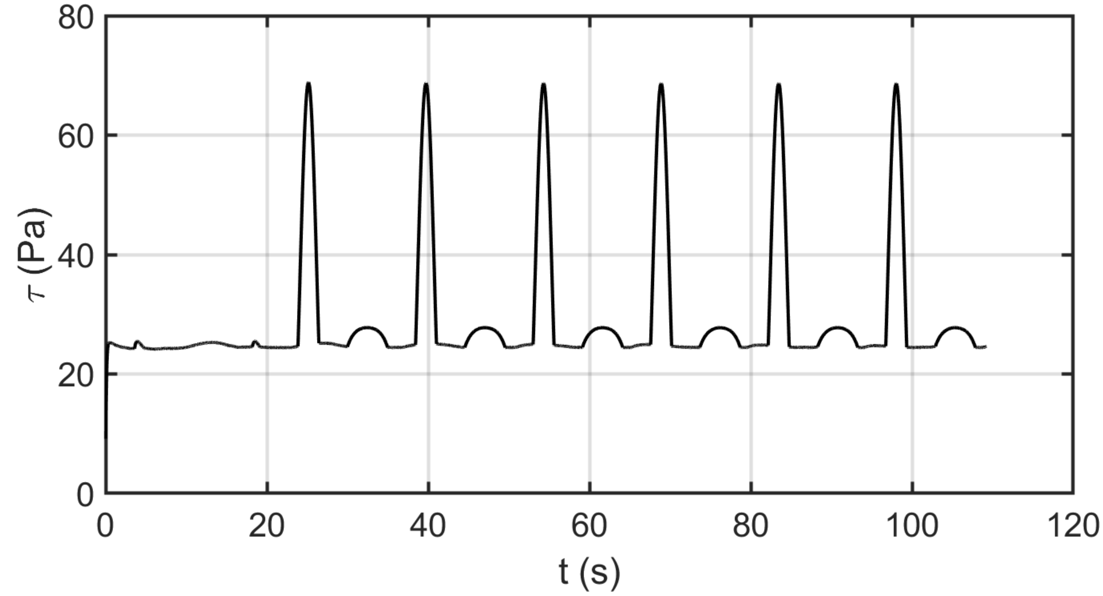

Figure 3-59. Large-scale amplified stress data from Run LS21

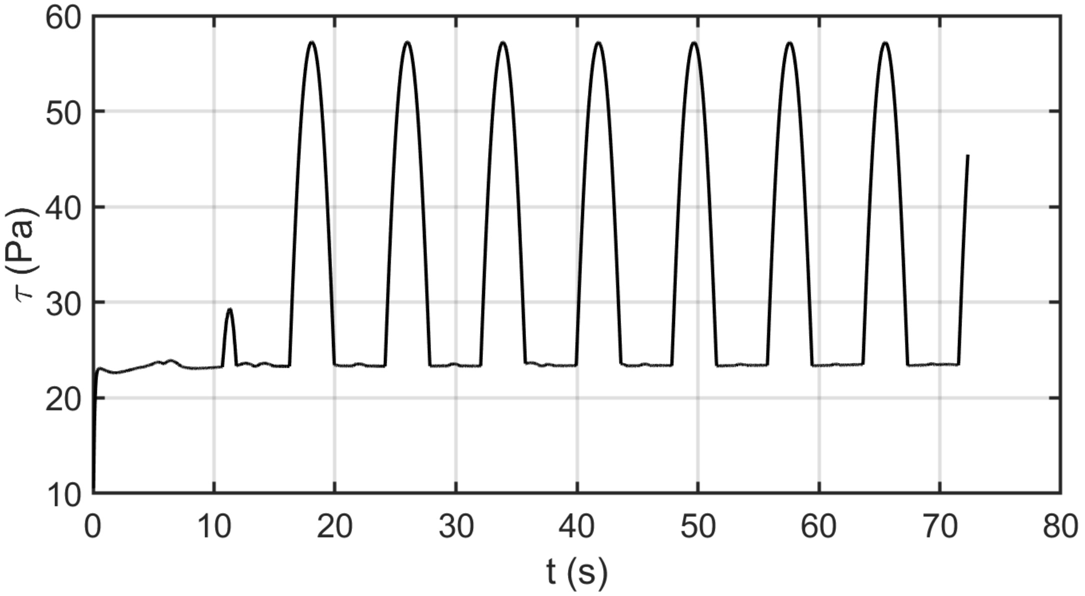

Figure 3-60. Large-scale amplified stress data from Run LS22

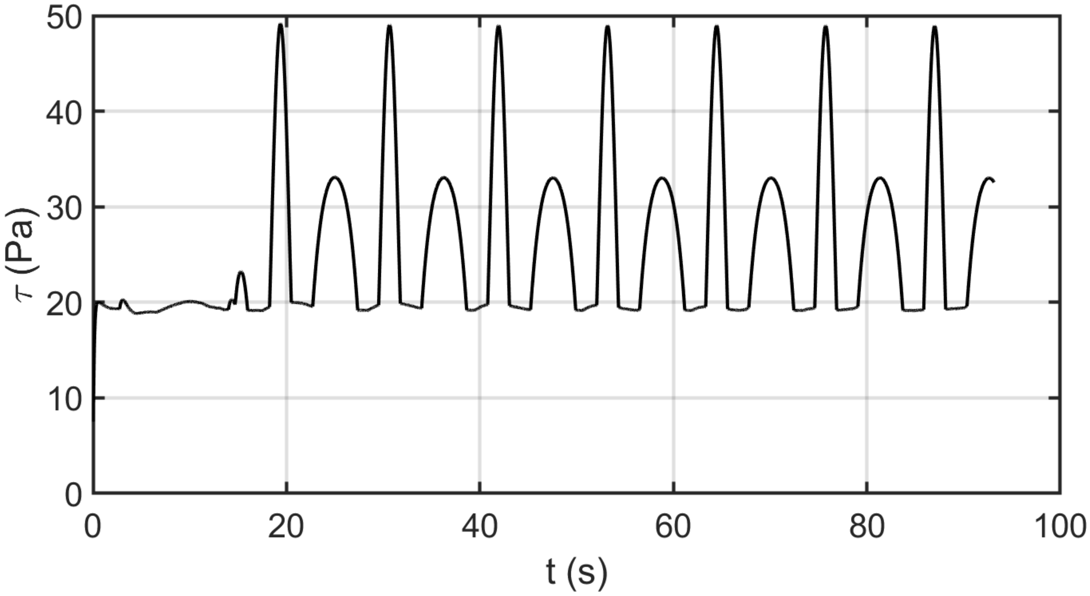

Figure 3-61. Large-scale amplified stress data from Run LS23

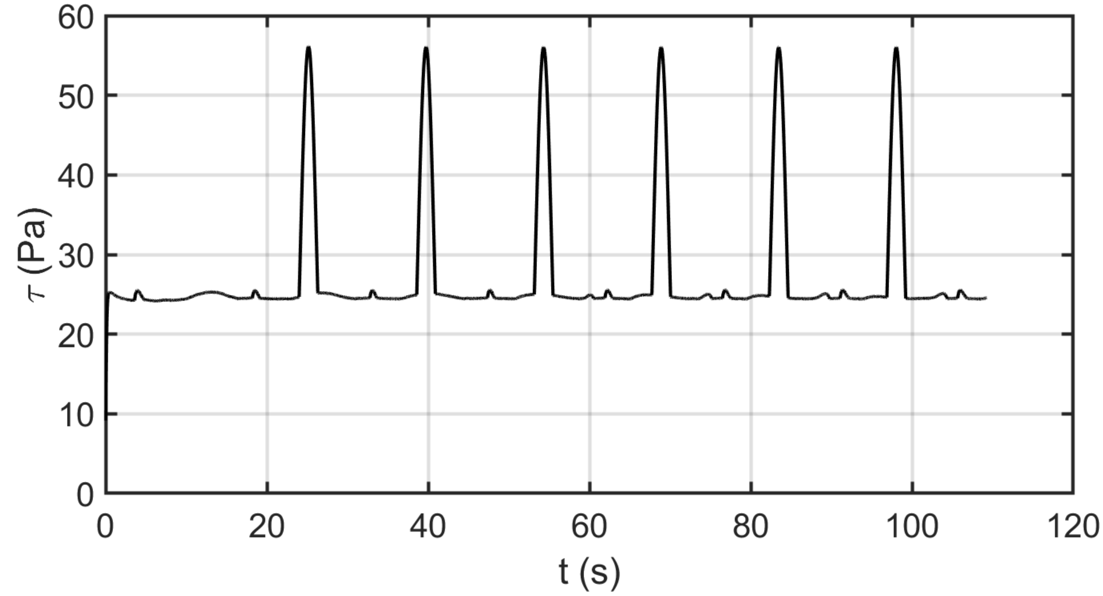

Figure 3-62. Large-scale amplified stress data from Run LS24

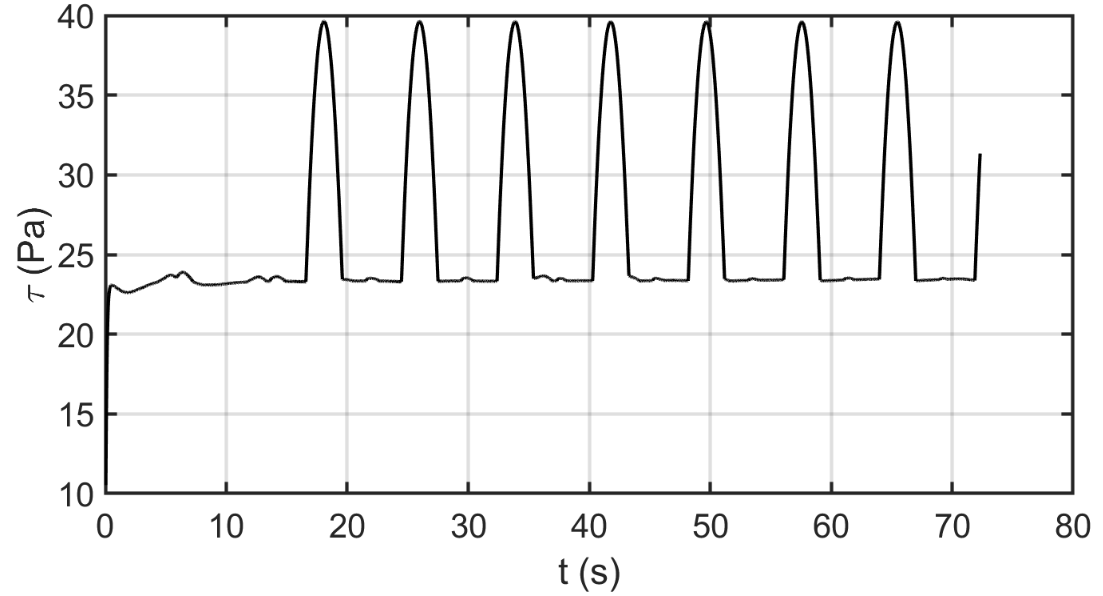

Figure 3-63. Large-scale amplified stress data from Run LS25

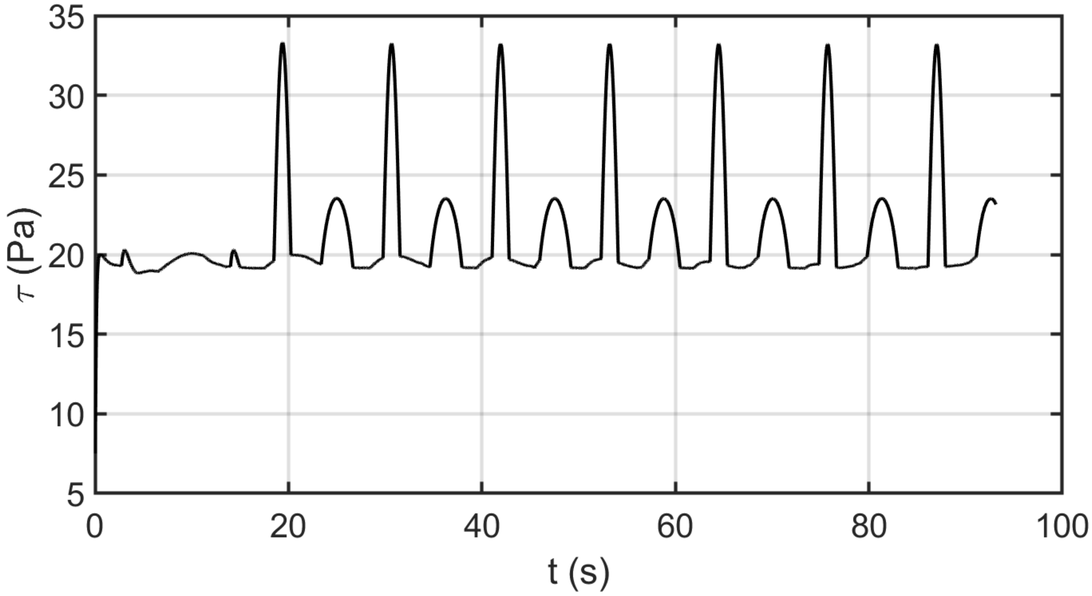

Figure 3-64. Large-scale amplified stress data from Run LS26

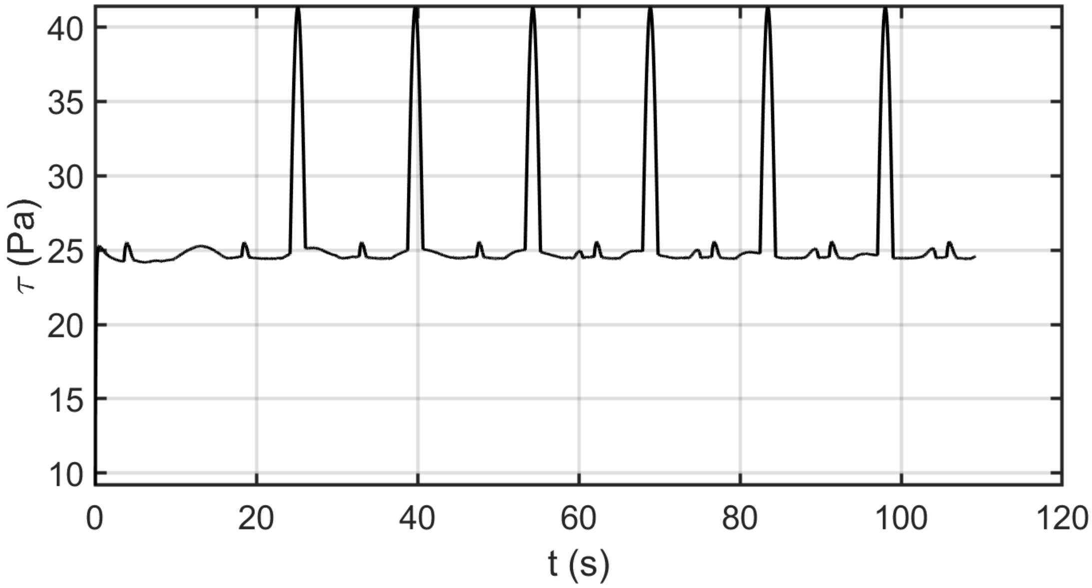

Figure 3-65. Large-scale amplified stress data from Run LS27

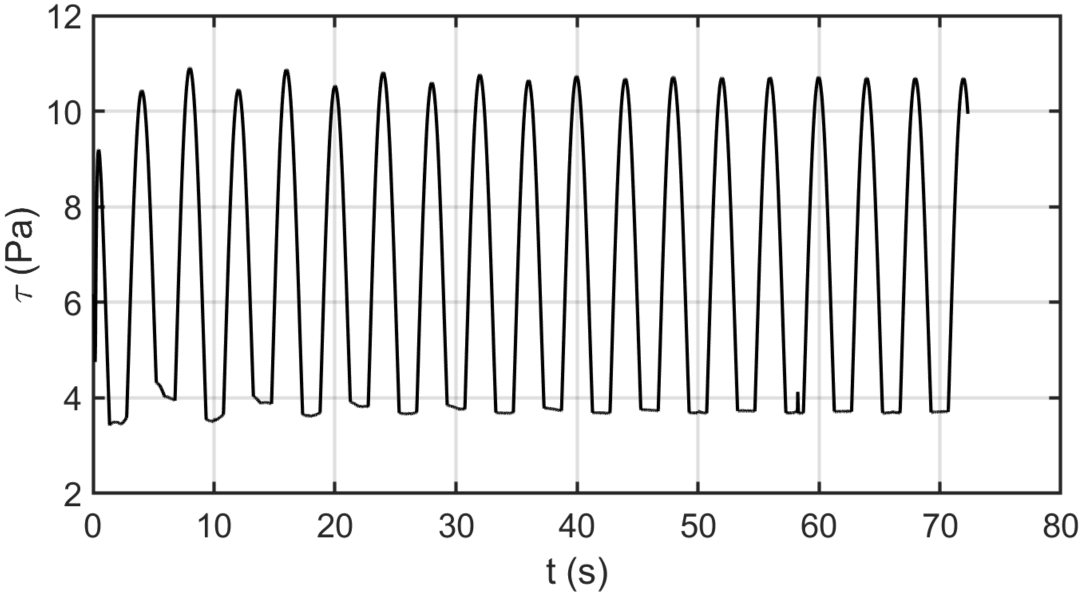

Figure 3-66. Large-scale amplified stress data from Run LS28

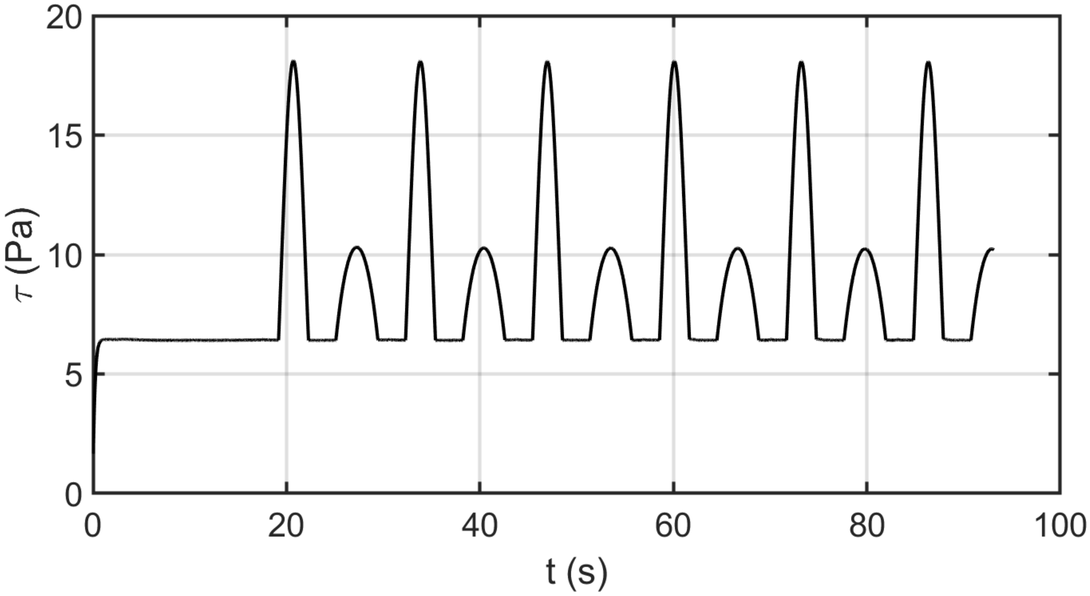

Figure 3-67. Large-scale amplified stress data from Run LS29

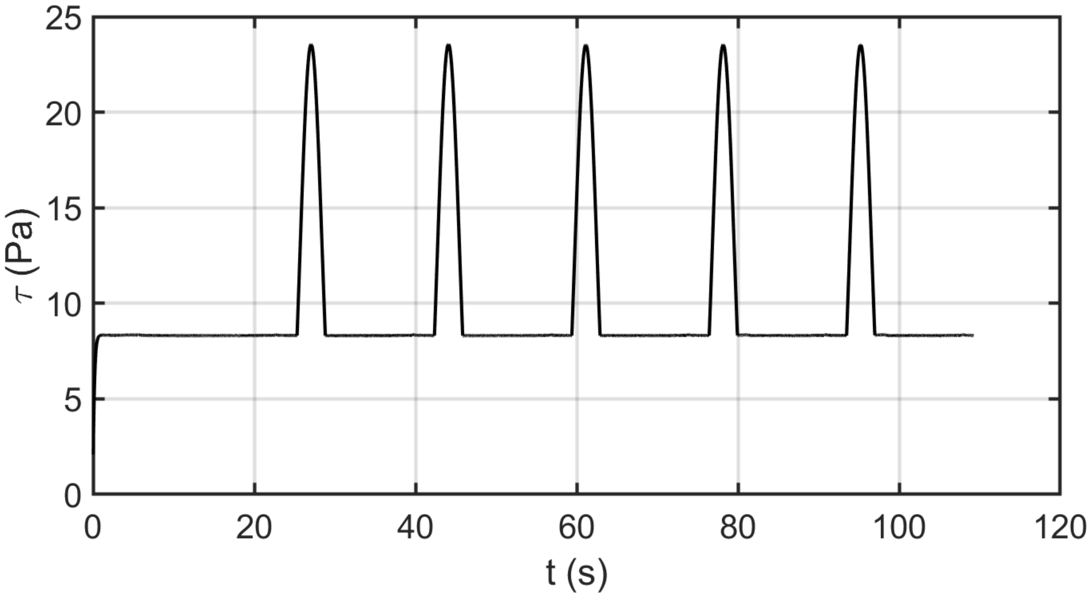

Figure 3-68. Large-scale amplified stress data from Run LS30

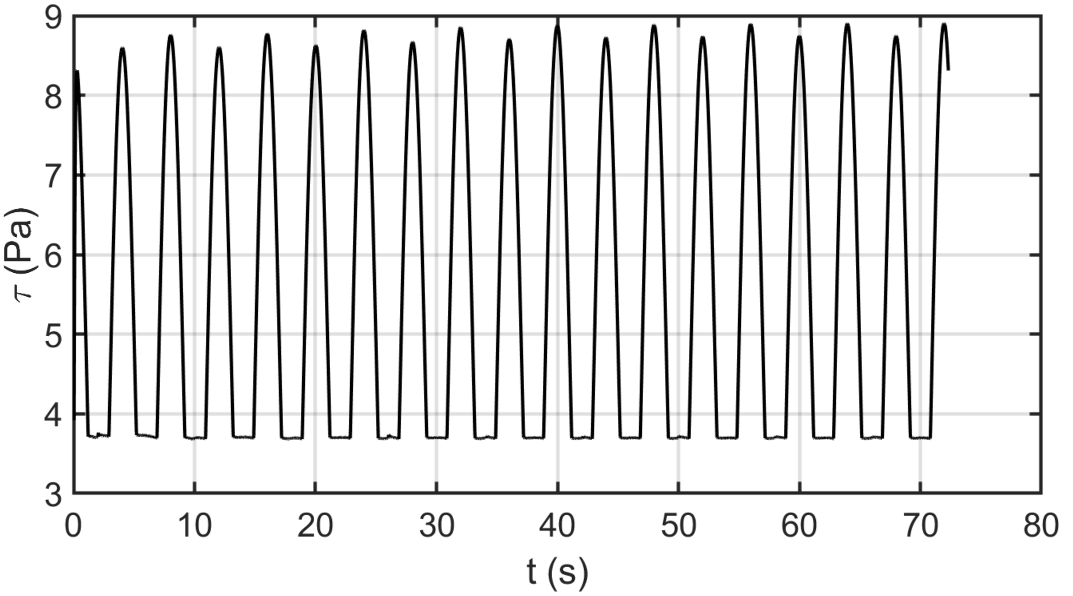

Figure 3-69. Large-scale amplified stress data from Run LS31

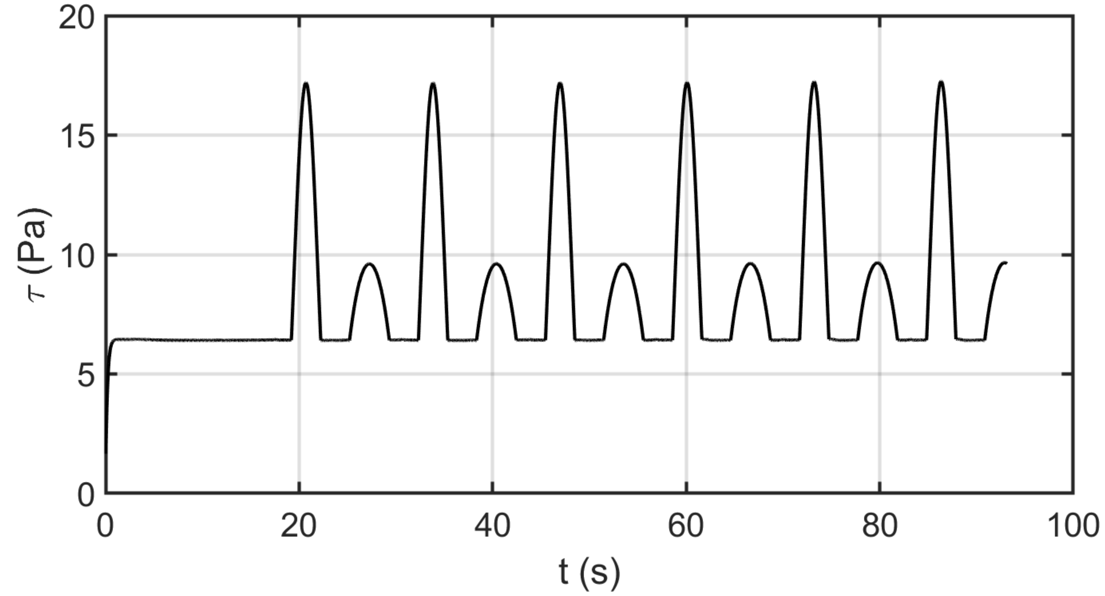

Figure 3-70. Large-scale amplified stress data from Run LS32

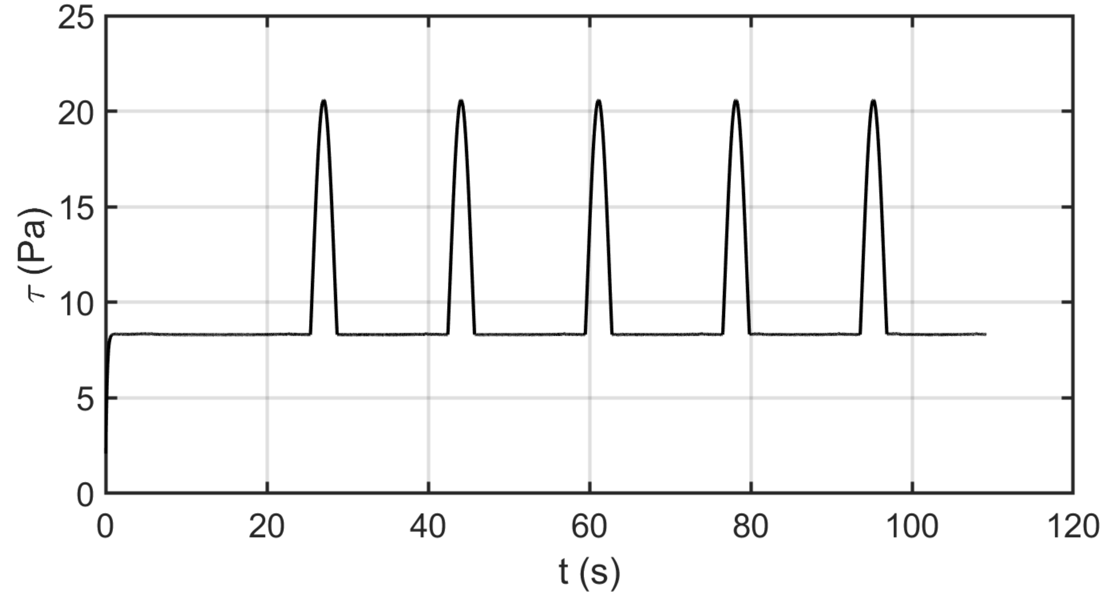

Figure 3-71. Large-scale amplified stress data from Run LS33

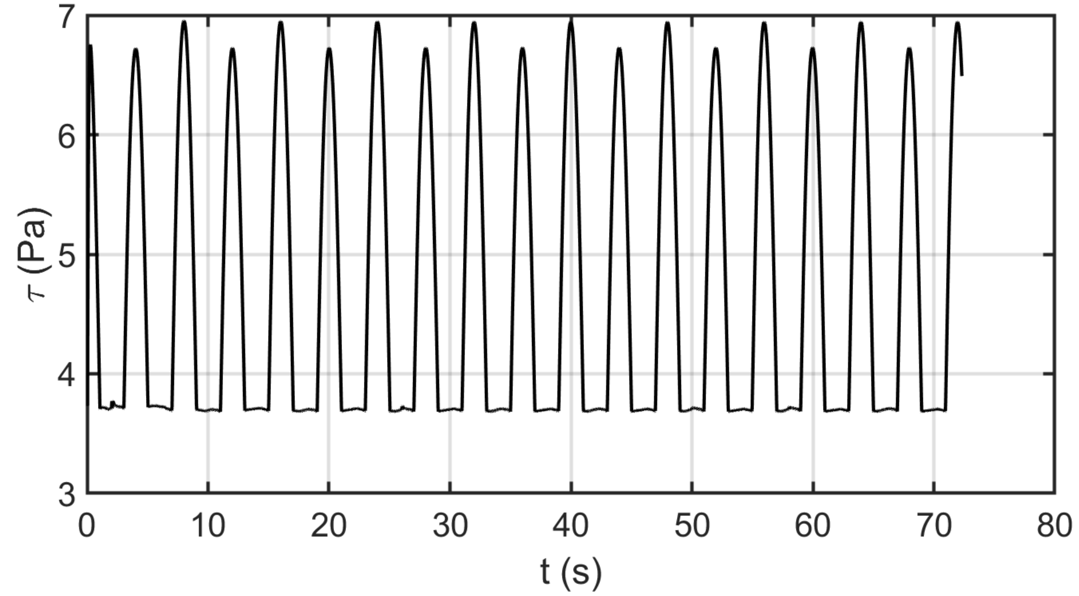

Figure 3-72. Large-scale amplified stress data from Run LS34

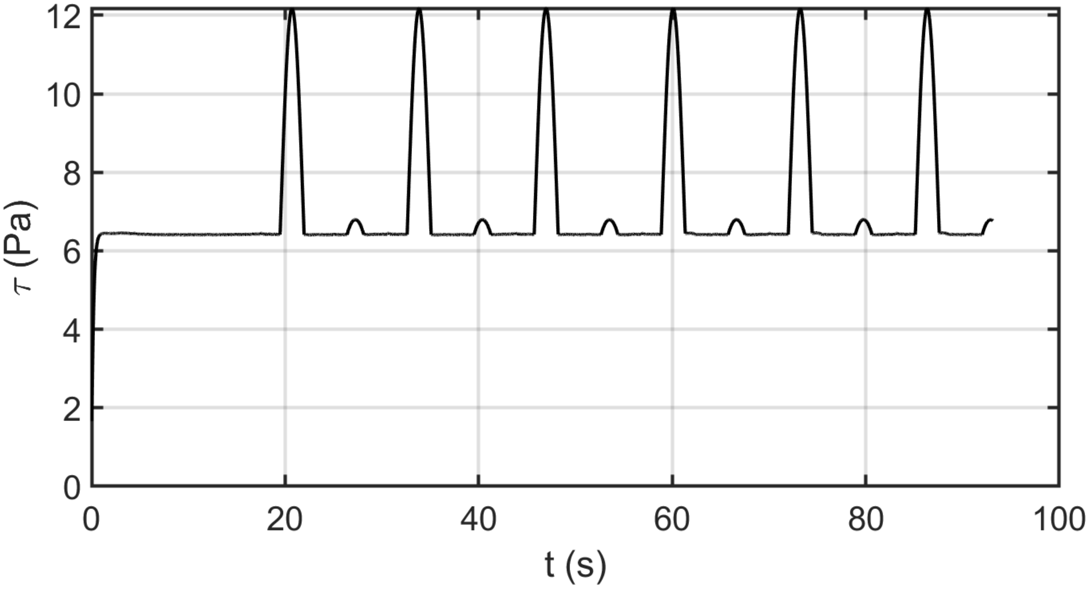

Figure 3-73. Large-scale amplified stress data from Run LS35

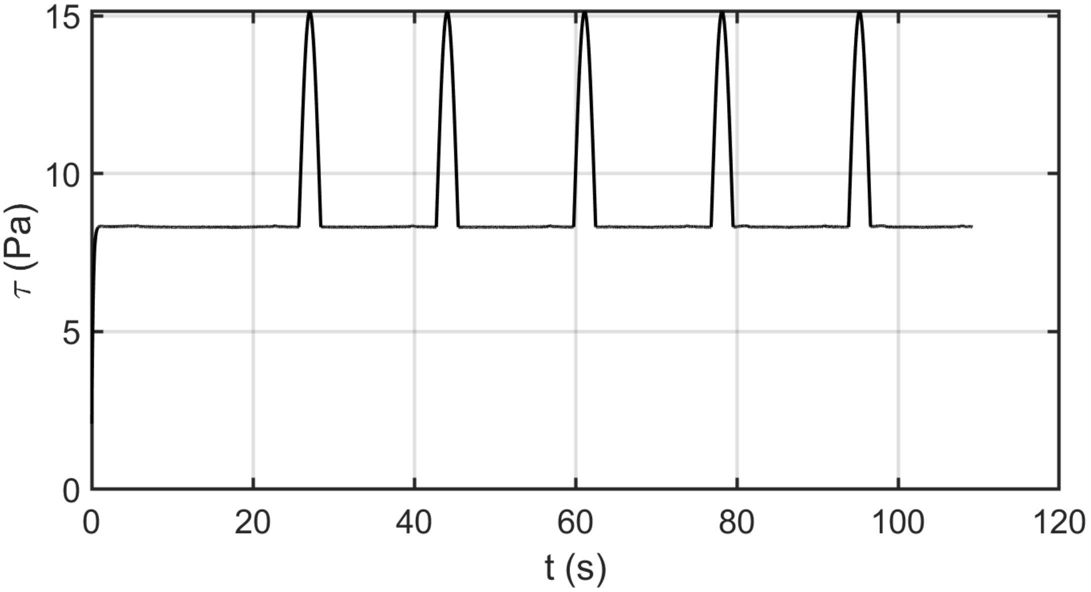

Figure 3-74. Large-scale amplified stress data from Run LS36

As shown in these figures, maximum stress values from wavelength to wavelength appear to be very stable.

CHAPTER 4
DATA ANALYSIS AND DEVELOPMENT OF PARAMETRIC MODEL

4.1 Location and Timing of Maximum Bottom Stress

Figure 4-1 below shows the location and timing associated with the maximum bottom stress. As shown, the maximum stress appeared to occur when the wave crests interacted with the pile. Its locus was at approximately the wake's separation point. This result was consistent from run to run. Maximum stress data from this time/location were extracted from each raw dataset presented in Chapter 3. These data were used to fit two parametric models – a simple model that physically appeared to be correct, and an apparently more accurate model that was more empirically based.

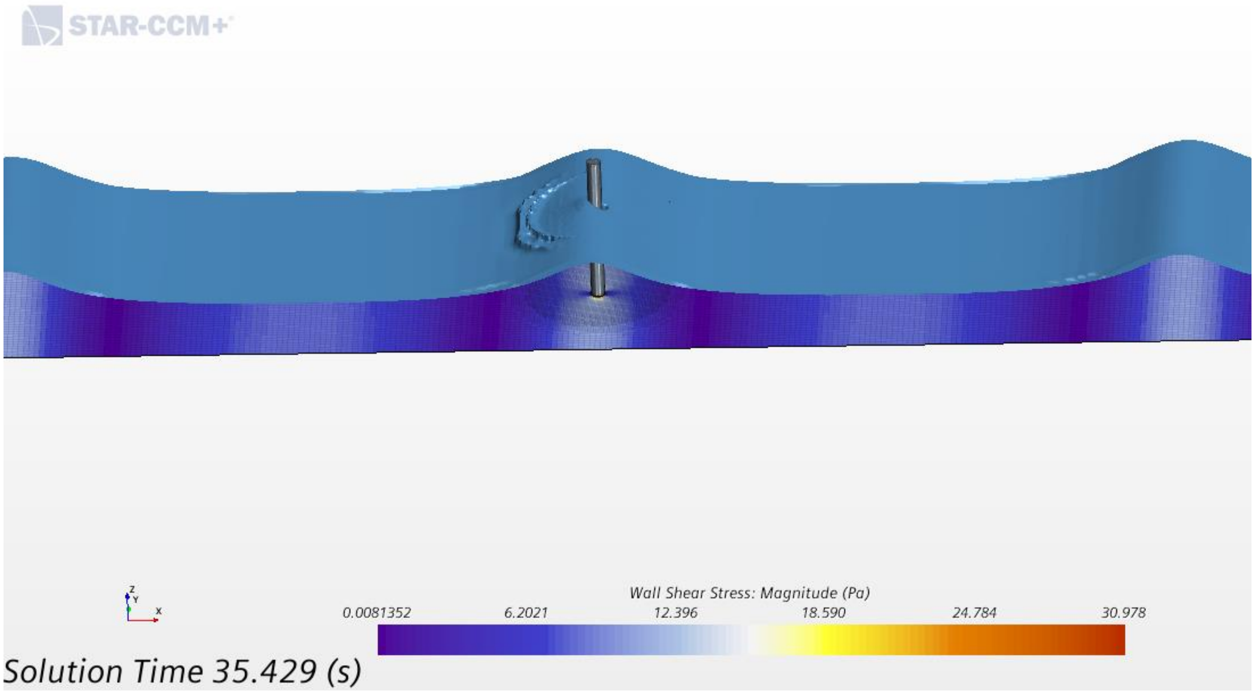

Figure 4-1. Example of moment when maximum bottom stress occurred (Run LS1 shown)

4.2 The Simple Parametric Model

4.2.1 Dimensional Analysis

Preliminary dimensional analysis indicated that maximum bottom shear stress during wave attack on a circular pile should be governed by the following nondimensional groups:

- The Keuligan Carpenter Number, *KC* (Equation 1-1).
- The Reynolds Number, *Re*

$$Re = \frac{U_m D}{\nu} \tag{4-2}$$

- The ratio between *D* and *L*.

Overall, then:

$$\tau_{max} = f\left(KC, Re, \frac{D}{L}\right) \tag{4-3}$$

U_m may be approximated using the linear wave equation at the bed (i.e., $z = -h$ where h is the water depth):

$$U_m = \frac{gHk}{2\omega} \tag{4-4}$$

where *k* is solved by inverting Equation 2-34:

$$k = \frac{2\pi}{L} \tag{4-5}$$

and ω is solved by inverting Equation 2-33:

$$\omega = \frac{2\pi}{T} \tag{4-6}$$

4.2.2 Unification with Steady Flow Equation

In addition, as discussed in Chapter 1, the maximum bottom stress around a pile under steady flow conditions is known and was presented in Equation 1-6. As noted in Chapter 1, steady flow implies that *KC* and *L* approach infinity because an infinite wavelength corresponds to an infinite wave period. As such, any nondimensional parametric design equation for bed stress due to waves should also approach Equation 1-6 when *KC* and *L* approach infinity.

4.2.3 Simple Parametric Model Development Procedure

To develop the parametric model, investigators isolated the maximum bed stresses from each of the raw datasets presented in Chapter 3. These maximum stresses were nondimensionalized:

$$\tau^* = \frac{\tau_{max}}{\rho U_m^2} \tag{4-7}$$

Next, the corresponding values for *Re* and *D/L* were computed. To ensure that the parametric model approached the steady flow expression, Equation 1-6 was rearranged, its correction coefficients were dropped, and U_m was substituted for *V*:

$$\frac{\tau}{0.094\rho U_m^2} = \frac{1}{\log(Re)} - \frac{1}{10} \tag{4-8}$$

Finally, a multidimensional curve fitting tool, nDCurveMaster, was used to develop a best-fit regression expression among τ^* and *KC, L/D,* and the right-hand side of Equation 4-8. This process involved significant trial-and-error to ensure that the resultant parametric model was correct physically in the sense that an infinite KC or L should cause the wave component terms to cancel. Likewise, investigators also ensured that a zero-flow condition would lead to a zero-stress condition. The resultant model from this process that appeared to fit the data the best was:

$$\frac{\tau_{max}}{\rho U_m^2} = a_1\left(\frac{D}{L}\right) + a_2\left(\frac{1}{\log_{10} Re} - \frac{1}{10}\right) + a_3\left(\frac{D}{L}\right)\left(\frac{1}{\log_{10} Re} - \frac{1}{10}\right) + a_4 KC^{-1} \tag{4-9}$$

where

- $a_1 = -0.4528$
- $a_2 = 0.1072$
- $a_3 = 5.1325$
- $a_4 = 0.00781$

Results showing data predicted by Equation 4-9 and raw data are presented below in Figure 4-2:

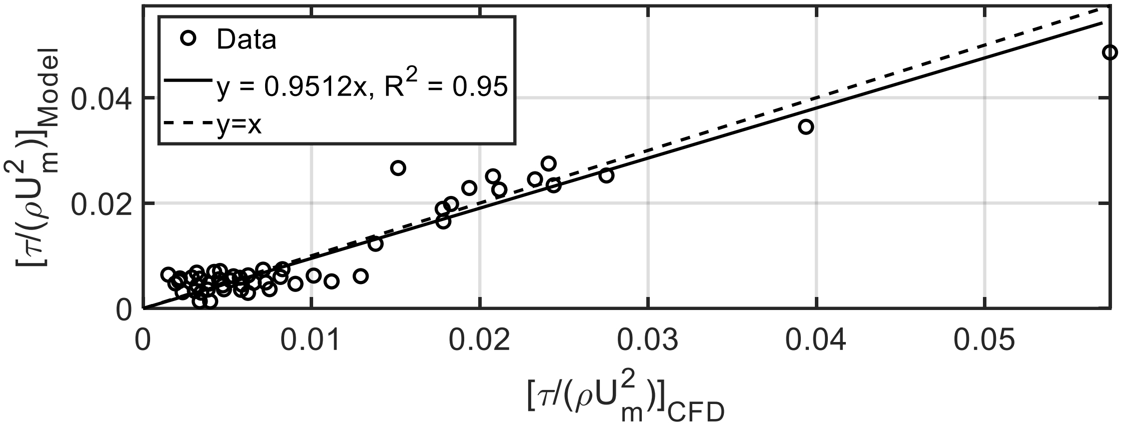

Figure 4-2. Results showing modeled results from Equation 4-9 as a function of raw data

As shown in Figure 4-2, Equation 4-9 is capable of reproducing CFD results with approximately 95% accuracy and an associated R^2 value of approximately 0.95. Further analysis of Equation 4-9 also appears to indicate that the model behaves correctly physically for both the infinite KC condition and the zero-flow condition. When flow equals zero, the U_m term on the left-hand side of Equation 4-9 causes τ_{max} to also equal zero. When KC and L approach infinity, the a_1, a_3, and a_4 terms from Equation 2-9 will approach zero leaving only the steady-flow equation for maximum bottom stress. Meanwhile, it is also interesting to note that the a_2 coefficient of 0.11 is very close to the reported value from Equation 1-6 (Equation 1-6 shows a coefficient of 0.094). Thus, this model appears to function correctly and appears to unify steady-flow bottom stress and associated scour with wave-induced bottom stress and associated scour.

4.4.4 Simple Parametric Model Example Problem

To illustrate how one might implement this parametric model for scour design, consider the following example: A 2-foot diameter pile is subjected to water wave attack. The wave period is 15 seconds, the water depth is 5 feet, and the expected maximum wave height is 10 feet under hurricane conditions. Find the maximum bottom stress around the pile under these conditions. The solution is:

1. Use the linear dispersion relationship to solve for the wave number, *k*. The dispersion relationship is:

$$\omega^2 = gk\tanh(kh) \tag{4-10}$$

Substituting:

$$\frac{2\pi}{(15\ s)^2} = \left(\frac{32.2ft}{s^2}\right)k\tanh[(5ft)(k)] \tag{4-11}$$

This is an implicit equation that must be solved using a numerical solver (i.e., Excel, MATLAB, etc.). Solving, one finds:

$$k = 0.033ft^{-1} \tag{4-12}$$

2. Using *k* from Step 1, determine the wavelength, *L*:

$$L = \frac{2\pi}{k} = \frac{2\pi}{0.033ft^{-1}} = 189\ ft \tag{4-13}$$

3. Compute U_m

$$U_m = \frac{gHk}{2\sigma} = \frac{\left(32.2\frac{ft}{s^2}\right)(10\ ft)\left(189ft^{-1}\right)}{\left[2\left(\frac{2\pi}{15s}\right)\right]} = 12.75\frac{ft}{s} \tag{4-14}$$

4. Compute *Re* and *KC*:

$$Re = \frac{U_m D}{\nu} = \frac{\left(25.5\frac{ft}{s}\right)(2\ ft)}{\left(1.08\frac{ft^2}{s}\right)} = 2.37 \times 10^6 \tag{4-15}$$

$$KC = \frac{U_m T}{D} = \frac{\left(25.5\frac{ft}{s}\right)(15\ s)}{2\ ft} = 95.6 \tag{4-16}$$

5. Substitute into Equation 4-9 to get maximum stress:

$$\tau_{max} = \rho U_m^2\left[a_1\left(\frac{D}{L}\right) + a_2\left(\frac{1}{\log_{10}Re} - \frac{1}{10}\right) + a_3\left(\frac{D}{L}\right)\left(\frac{1}{\log_{10}Re} - \frac{1}{10}\right) + a_4KC^{-1}\right] \tag{4-17}$$

$$= \left(1.94\frac{slugs}{ft^3}\right)\left(12.75\frac{ft}{s}\right)^2\left\{-0.4528\left(\frac{2ft}{189ft}\right) + 0.1072\left[\frac{1}{\log_{10}(2.37\times10^6)} - \frac{1}{10}\right] + 5.1325\left(\frac{2ft}{189ft}\right)\left[\frac{1}{\log_{10}(2.37\times10^6)} - \frac{1}{10}\right] + \frac{0.00781}{95.6}\right\} = 1.41\ psf$$

6. If necessary, convert from English units to SI (scour design is usually conducted in SI):

$$1.41\, psf \left(\frac{47.88 Pa}{psf}\right) = 67.58\, Pa \qquad (4\text{-}18)$$

4.4.5 Parametric Design Equation Automation

Equations 4-10 through 4-18 can be automated using a computer program. Calculators were prepared using the parametric model in both MATLAB and Microsoft Excel. These calculators are submitted with this report.

4.4.5.1 Simple Model Excel Maximum Stress Calculator

The automated parametric model calculator in Excel is presented here:

Table 4-1. Excel Maximum Stress Calculator

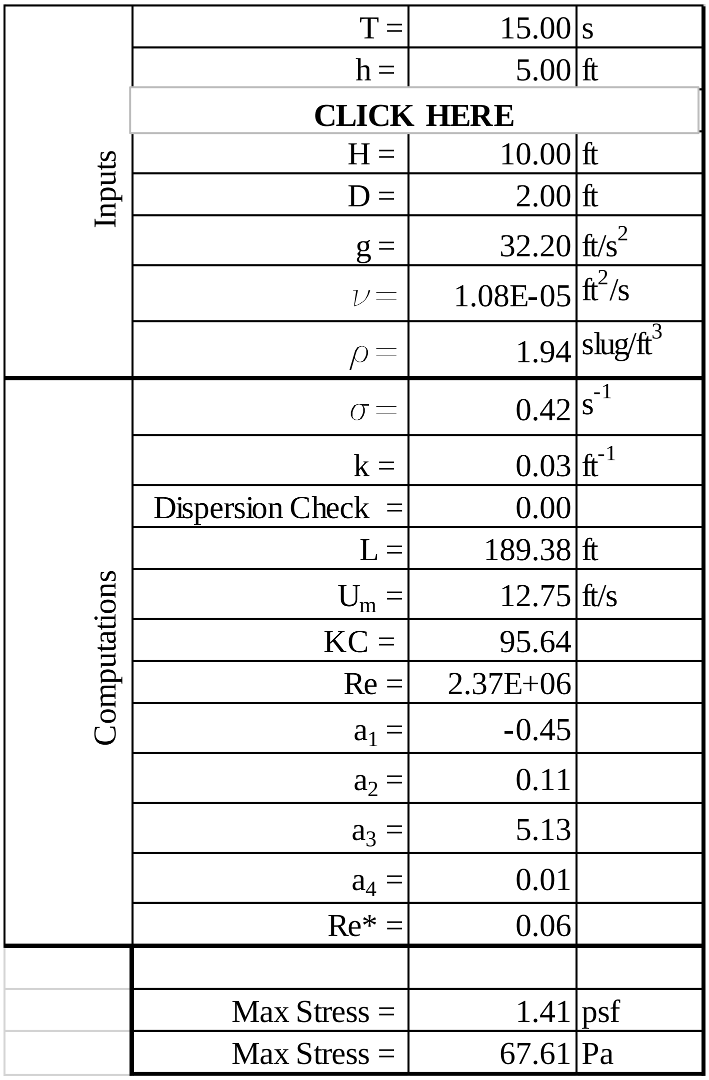

Inputs	T =	15.00	s
	h =	5.00	ft
	CLICK HERE		
	H =	10.00	ft
	D =	2.00	ft
	g =	32.20	ft/s^2
	$\nu =$	1.08E-05	ft^2/s
	$\rho =$	1.94	slug/ft^3
Computations	$\sigma =$	0.42	s^{-1}
	k =	0.03	ft^{-1}
	Dispersion Check =	0.00	
	L =	189.38	ft
	U_m =	12.75	ft/s
	KC =	95.64	
	Re =	2.37E+06	
	a_1 =	-0.45	
	a_2 =	0.11	
	a_3 =	5.13	
	a_4 =	0.01	
	Re* =	0.06	
	Max Stress =	1.41	psf
	Max Stress =	67.61	Pa

To use this calculator, first enter the wave period, *T* and water depth, *h*. Then, click the CLICK HERE button shown on the second line. This will run a Goal Seek macro that will solve the dispersion relationship for *k*. The dispersion relationship was given previously in Equation 2-35 as a function of *L*. As a function of *k*, the dispersion relationship is:

$$\left(\frac{2\pi}{T}\right)^2 = gk \tanh{(kh)} \tag{4-19}$$

If cell C12 approaches zero (cell labeled Dispersion Check), the user should have confidence that the macro functioned as designed. After this, continue entering data including wave height, *H* and pile diameter, *D*. The acceleration due to gravity, g should remain the same as should the kinematic viscosity and water density, ν and ρ respectively. Computations for $\sigma = \frac{2\pi}{T}$, $L = \frac{2\pi}{k}$, and $U_m = \frac{gHk}{2\sigma}$; $KC = \frac{U_m T}{D}$; and $Re = \frac{U_m D}{\nu}$ should not be changed nor should the fit coefficients, a_1, a_2, a_3, and a_4. The resultant output should be maximum bed stress near the pile in either psf or Pa.

4.4.5.2 Simple Model MATLAB Maximum Stress Calculator

The automated parametric model calculator in MATLAB is presented below. To use this model, simply enter values for *T*, *h*, *H*, *D*, *g*, *nu* (i.e., ν), and *rho* (i.e., ρ). Set the variable "answer_flag" to zero for output in Pascals or any other number for output in psf. Then, run the script. The advantage to the MATLAB calculator is that a separate button press is not required to initiate its numerical solver. The output will be maximum bed shear stress near the pile in either Pascals or psf.

```
clc; clear; close all;
%% ------------------------------------------------------------------------
% wavestress_calc.m
% Maximum shear stress calculator for circular vertical pile under wave
% attack
%
% Version 1.1
%
% Prepared by: University of North Florida
%
% Prepared for: Florida Department of Transportation
%
% Inputs
% T - wave period (in seconds)
% h - water depth (in feet)
% H - wave height (crest-to-trough distance; in feet)
% D - pile diameter (in feet)
% g - acceleration due to gravity (in feet/second^2)
% nu - kinematic viscosity of water (in feet^2/second)
% rho - density of water (in slug/ft^3)
% answer_flag - set to 1 for English output or any other number for SI
% output
%
% Outputs
% tau_max - maximum bed stress in Pascals or psf
%
%--------------------------------------------------------------------------
%% Inputs go here
T = 15;             % Wave period (in seconds)
h = 5;              % Water depth (in feet)
H = 10;             % Wave height (in feet)
D = 2;              % Pile diameter (in feet)
g = 32.2;           % Acceleration due to gravity (in feet/second^2)
nu = 1.07639e-5;    % Kinematic viscosity of water (in feet^2/second)
rho = 1.94;         % Density of water (in slug/ft^3)
answer_flag = 0;    % Answer flag - set == 1 for English units or any other
number for Pascals
%% Computations
sigma = 2*pi/T;
syms x
k = vpasolve(sigma^2 == g*x*tanh(x*h),x,0.5); k = eval(k);
L = 2*pi/k;
Um = g*H*k/(2*sigma);
KC = Um*T/D;
Re = Um*D/nu;
a1 = -4.5281e-1;
a2 = 0.10715109;
a3 = 5.13247395;
a4 = 0.00780855;
briaudRE = 1/log10(Re)-1/10;
tau_model = rho*Um^2*(a1*D./L + a2*briaudRE + a3*D./L.*briaudRE + a4*KC.^-1);
%% Outputs
if answer_flag == 1
    disp(['The maximum stress = ',num2str(tau_model),' psf'])
else
    tau_model = tau_model*47.8803;
    disp(['The maximum stress = ',num2str(tau_model),' Pa'])
end
```

4.3 The More Sophisticated Parametric Model

While results from the Simple Parametric Model were promising in the sense that data fitting appeared to unify steady flow and wave stresses, and the R-squared values associated with the model were relatively high, some inaccuracies were observed in Figure 4-2 – particularly for low and high nondimensionalized stress values. As such, investigators sought to improve the model.

4.3.1 Additional Dimensional Analysis and a More Sophisticated Model

Initially, investigators had assumed that wave height, *H*, was considered in their model via *KC*, which is computed using U_m that is a function of *H*. However, wave steepness (i.e., *H/L*) was not explicitly included in the original model. If one adds steepness to the dimensional analysis presented in Section 4.2:

$$\frac{\tau}{(\rho U_m^2)} = f\left(KC, Re, \frac{D}{L}, \frac{H}{L}\right) \tag{4-20}$$

The addition of the $\frac{H}{L}$ nondimensional group led to a parametric model of the following form:

$$\frac{\tau}{\rho U_m^2} = a_0 + a_1\left(\frac{H}{L}\right)^{1.05} + a_2\left(\frac{D}{L}\right)^{0.99} + a_3 KC^{-0.65} + a_4 \exp\left(\log_{10}\ (Re)\right)^3 + a_5\left(\frac{HD}{L^2}\right)^{1.2} + a_6\left(\frac{H}{L}\right)^{3.15} KC^{-1.3} + a_7\left(\frac{H}{L}\right)^{0.95}(\log_{10}(Re))^2 + a_8\left(\frac{D}{L}\right)^{1.55} KC^{1.05} + a_9\left(\frac{D}{L}\right)^{1.05}(\log_{10} Re)^{0.72} + a_{10} KC^{\frac{1}{15}}(\log_{10} Re)^{0.125} + a_{11}\left(\frac{H}{L}\right)^{2.1}\left(\frac{D}{L}\right)^{1.05}\ln(KC) + a_{12}\left(\frac{D}{L}\right)^{1.4} KC^{-0.9}(\log_{10} Re)^{-2.6} + a_{13}\left(\ln\left(\frac{H}{L}\right)\right)^5\left(\frac{D}{L}\right)^{1.05} KC^{0.81}(\log_{10}(Re))^2 \tag{4-21}$$

where

- $a_0 = -0.045678$
- $a_1 = 0.08110917$
- $a_2 = -4.2112$
- $a_3 = 0.15463676$
- $a_4 = -12883$
- $a_5 = 1.2790872$
- $a_6 = -0.025252$
- $a_7 = -0.0031414$
- $a_8 = 0.5468853$
- $a_9 = 0.87930766$
- $a_{10} = 0.0367309$
- $a_{11} = -0.031927$
- $a_{12} = -11.107$
- $a_{13} = -0.017212$

4.3.2 More Sophisticated Model Analysis

The advantage to this more sophisticated model is that it was able to reproduce the data much more accurately than the relatively simple model. As shown below in Figure 4-3, data were reproduced with 99% accuracy:

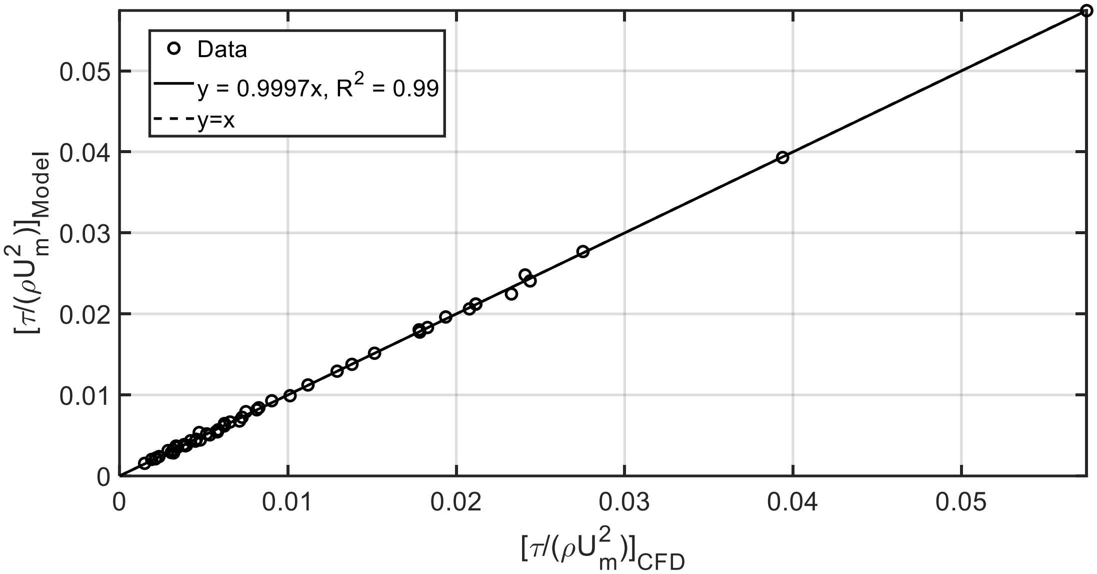

Figure 4-3. Results showing modeled results from Equation 4-20 as a function of raw data

Also as shown in Figure 4-3, the relatively large errors associated with smaller relative stresses and larger relative stresses are eliminated when this new model is used. However, the disadvantage of this model is that it does not converge toward the steady flow solution (i.e., Equation 4-8) for very large values of *KC*. Rather, as *KC* approaches infinity, Equation 4-20 also approaches infinity as shown below in Figure 4-4:

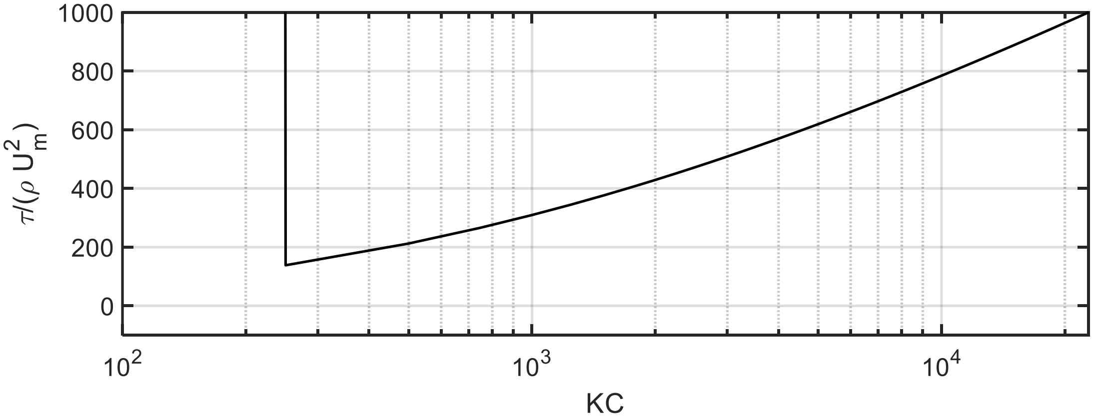

Figure 4-4. Behavior of Equation 4-20 as a function of *KC*

Physically, this is incorrect. Figure 1-1 shows that as KC approaches infinity, maximum scour depth (and by extension, maximum near-pile shear stress) should approach a steady value for a given U_m. However, at the same time, Equation 4-20 reproduces modeled data almost perfectly. In the context of scour design, it is believed that Equation 4-20 should give more accurate results than the simpler model even though physically, this equation does not behave as it should. In future work, one could model higher frequency waves and examine their bottom stresses to improve Equation 4-20 so it performs as it should under steady flow conditions. In the interim, however, Equation 4-20 appears to accurately reproduce stress data in typical design ranges associated with field-scale and small-scale waves. Please note however that Equation 4-20 should only be considered valid for wave heights, water depths, and wavelengths within the ranges discussed throughout this report.

4.3.3 More Sophisticated Model Calculators

Implementation of Equation 4-21 would be difficult by hand since there are many variables, exponents, terms, and places where one could make a typographical or calculation error. As such, an example problem will not be presented here. However, implementation is almost the same as the simple example problem previously presented in the sense that Equations 4-10 through 4-16 are used to compute nondimensional parameters. Then, the nondimensional parameters are used as inputs for Equation 4-20. The MATLAB and Microsoft Excel calculators were updated to reflect the new model and are presented below. In addition, these calculators were submitted with this report.

Similar to the simple calculator presented in Section 4.4.5.1, the more sophisticated Excel calculator requires the user to enter the wave period and water depth. Then, the CLICK HERE button must be pressed to solve the dispersion relationship for the wave number. If cell E12 approaches zero, the user may be confident that the Goal Seek macro functioned as designed. Then, the user may enter data for the wave height and pile diameter. Since the more sophisticated model contained so many fit coefficients, these are hidden in Column A and should not be touched. Similarly, g, ν, ρ and all of the computation cells should also not be modified. The output should be maximum stress in Pascals or psf.

The more sophisticated MATLAB calculator works similarly to the calculator presented in Section 4.4.5.2 in the sense that once the inputs are defined, the numerical solver is automated, and output should immediately follow after running the script. These calculators are presented below.

4.3.3.1 Sophisticated Model Excel Calculator

Table 4-2. Enhanced Parametric Model Excel Calculator

Inputs	T =	15.00	s
	h =	32.81	ft
	CLICK HERE		
	H =	32.81	ft
	D =	3.28	ft
	g =	32.20	ft/s^2
	$\nu =$	1.08E-05	ft^2/s
	$\rho =$	1.94	slug/ft^3
Computations	$\sigma =$	0.42	s^{-1}
	k =	0.01	ft^{-1}
	Dispersion Check =	0.00	
	L =	471.81	ft
	U_m =	16.79	ft/s
	KC =	76.78	
	Re =	5.12E+06	
	Max Stress =	5.084109531	psf
	Max Stress =	243.43	Pa

4.3.3.2 Sophisticated Model MATLAB Maximum Stress Calculator

```
clc; clear; close all;
%% ------------------------------------------------------------------------
% wavestress_calc.m
% Maximum shear stress calculator for circular vertical pile under wave
% attack - complicated model
% % Version 1.2
% % Prepared by: University of North Florida
% % Prepared for: Florida Department of Transportation
%
% Inputs
% T - wave period (in seconds)
% h - water depth (in feet)
% H - wave height (crest-to-trough distance; in feet)
% D - pile diameter (in feet)
% g - acceleration due to gravity (in feet/second^2)
% nu - kinematic viscosity of water (in feet^2/second)
% rho - density of water (in slug/ft^3)
% answer_flag - set to 1 for English output or any other number for SI
% output
%
% Outputs
% tau_max - maximum bed stress in Pascals or psf
%%--------------------------------------------------------------------------
%% Inputs go here
T = 15;             % Wave period (in seconds)
h = 32.8084;           % Water depth (in feet)
H = 32.8084;           % Wave height (in feet)
D = 3.28084;           % Pile diameter (in feet)
g = 32.2;           % Acceleration due to gravity (in feet/second^2)
nu = 1.07639e-5;    % Kinematic viscosity of water (in feet^2/second)
rho = 1.94;         % Density of water (in slug/ft^3)
answer_flag = 0;    % Answer flag - set == 1 for English units or any other number for
Pascals
%% Computations
sigma = 2*pi/T;
syms x
k = vpasolve(sigma^2 == g*x*tanh(x*h),x,0.5); k = eval(k);
L = 2*pi/k;
Um = g*H*k/(2*sigma);
KC = Um*T/D;
Re = Um*D/nu;
a0=-0.04567800;a1=0.08110917;a2=-4.21120000;a3=0.15463676;a4=-12283.00000000;
a5=1.22790872;a6=-0.02525200;a7=-0.00314140;a8=0.54688530;a9=0.87930766;
a10=0.03673090;a11=-0.03192700;a12=-11.10700000;
a13=-0.01721200;
tau_model = (a0  + a1 .* (H./L).^1.05 + a2 .* (D./L).^0.99 + a3 .* KC.^-0.65 + a4 .*
exp(log10(Re)).^-3 + a5 .* (H./L).^1.2 .* (D./L).^1.2 + a6 .* (H./L).^3.15 .* KC.^-1.3
+ a7 .* (H./L).^0.95 .* log10(Re).^2 + a8 .* (D./L).^1.55 .* KC.^1.05 + a9 .*
(D./L).^1.05 .* log10(Re).^0.72 + a10 .* KC.^(1/15) .* log10(Re).^(-1/8) + a11 .*
(H./L).^2.1 .* (D./L).^1.05 .* log(KC) + a12 .* (D./L).^1.4 .* KC.^-0.9 .*
log10(Re).^-2.6 + a13 .* (log((H./L))).^5 .* (D./L).^1.05 .* KC.^0.81 .* log10(Re).^-
2.9)*rho*Um^2;
%% Outputs
if answer_flag == 1
    disp(['The maximum stress = ',num2str(tau_model),' psf'])
else
    tau_model = tau_model*47.8803;
    disp(['The maximum stress = ',num2str(tau_model),' Pa'])
end
```

CHAPTER 5
SUMMARY, CONCLUSIONS, AND RECOMMENDED FUTURE WORK

5.1 Summary

To summarize:

- Several CFD models were prepared using Star-CCM+. These models were used to simulate small-scale piles under wave attack. Bottom stress analysis appeared to indicate that the models accurately reproduced experimental data.

- Since experimental data were relatively accurately reproduced, maximum stress data were obtained from each of the small-scale models.

- The small-scale models were upscaled, and maximum shear stress results were obtained.

- Maximum shear stress data were used to create two parametric models for maximum stress around a single vertical pile under wave attack. The first model was relatively simple and behaved as it should physically in the sense that as KC approached infinity, predicted stress approached a steady value for a given U_m. Despite this, at low stresses and very high stresses, some inaccuracies were observed. Another parametric model was developed that was able to reproduce the data almost perfectly. The downside to this new model is that it does not behave as it should physically in the sense that as KC approaches infinity, stresses continually increase for a given value of U_m. This is likely because extreme conditions (i.e., very short or high frequency waves) were not modeled.

5.2 Conclusions

From this study, one can conclude that it should be possible to parameterize bottom stress around a pile under wave attack using a relatively simple model. In addition, using a more complex model, typical field-scale data may be recreated nearly perfectly. However, the methods developed here should only be used for a single pile case and may not be appropriate for more complex bridge pier geometries.

Finally, examination of the data presented here shows that bottom stresses due to wave action may be extremely high. Examination of the model results and example problems presented in Chapter 4 shows that stresses from wave action alone could lead to stresses on the order of hundreds of Pascals. These stress magnitudes are high enough to significantly erode sand, cohesive soils, and some rock (although most Florida limestone would likely erode minimally under these stress conditions). Note that the stresses found in this report are from wave action only. Under wave and current conditions, the stresses would likely be even higher than the stresses presented here.

5.3 Recommendations for Future Work

This study was meant to be a first step toward developing a universal approach for scour design that utilizes erosion functions. From that perspective, this project was successful in the sense that wave stress parametric equations were developed, and these equations may be implemented in conjunction with SERF and RETA testing. However, the results presented here are only for a very simple bridge pier – a single pile under wave attack. In actuality, most (if not all) FDOT bridges use a standard pile group/pile cap/pier foundation configuration. As such, it would be beneficial to extend the work presented here to take these complex bridge geometries into account. Correction factors similar to those presented in Equation 1-9 should be developed before the scour design approach described in this report is fully implemented. Finally, in future work, it may be possible to develop a better, more sophisticated parametric model that is more accurate than the simple model presented here by modeling and capturing the behavior of higher frequency waves. However, it is important to point out that even without this, the tools that were developed during this project should be sufficient for design purposes for the simple one-pile case.

LIST OF REFERENCES

Arneson, L.A., Zevenburgen, L.W., Lagasse, P.F., Clopper, P.E., 2012. Evaluating Scour at Bridges Fifth Edition, Federal Highway Administration, Washington, D.C.

Bloomquist, D., Crowley, R., 2010. Enhancement of FDOT's SERF Device and a Study of Erosion Rates of Rock, Sand, and Clay Mixtures Using FDOT's RETA and SERF Equipment, Florida Department of Transportation, Tallahassee, FL.

Bloomquist, D., Sheppard, D.M., Schofield, S., Crowley, R.W., 2012. The Rotating Erosion Testing Apparatus (RETA): A Laboratory Device for Measuring Erosion Rates versus Shear Stresses of Rock and Cohesive Materials. Geotechnical Testing Journal, 35(4): 641-648.

Bloomquist, D.G., Sheppard, D.M., Schofield, S., 2007. Apparatus for Estimating the Rate of Erosion and Methods of the Same, United States Patent, Washington, DC.

Briaud, J.-L., Ting, F., Chen, H.C., Cao, Y., Han, S.-W., Kwak, K., 2001. Erosion Function Apparatus for Scour Rate Predictions. Journal of Geotechnical and Geoenvironmental Engineering, 127(2): 105-113.

Briaud, J.-L.C., H.-C.; Li, Y., Nurtjahyo, P., 2004. SRICOS-EFA Method for Complex Piers in Fine-Grained Soils. Journal of Geotechnical and Geoenvironmental Engineering, 130(11): 1180-1191. DOI:10.1061/(ASCE)1090-0241(2004)130:11(1180).

Briaud, J.-L.C., H.-C.; Li, Y.; Nurtjahyo, P.; Wang, J., 2006. SRICOS-EFA Method for Contraction Scour in Fine-Grained Soils. Journal of Geotechnical and Geoenvironmental Engineering, 131(10): 1283-1294. DOI:10.1061//ASCE/1090-0241/2005/131:10/1283.

Crowley, R., Bloomquist, D., Robeck, C., 2012a. Description of Erosion Rate Testing Devices and Correlations between Rock Erosion Rate and Cohesion, 6th International Conference on Scour and Erosion, Paris, France.

Crowley, R., Bloomquist, D., Shah, F.D., Holst, C.M., 2012b. The Sediment Erosion Rate Flume (SERF): A New Testing Device for Measuring Soil Erosion Rate and Shear Stress. Geotechincal Testing Journal, 35(4): 649-659.

Crowley, R.W., Bloomquist, D., Hayne, J.R., Holst, C.M., Shah, F.D., 2012c. Estimation and Measurement of Bed Material Shear Stresses in Erosion Rate Testing Devices. Journal of Hydraulic Engineering, 138(11): 990-994. DOI:10.1061/(asce)hy.1943-7900.0000608

Crowley, R.W., Bloomquist, D.G., Sheppard, D.M., 2014a. Investigation of Erosion Rates of Field Samples Using FDOT's Enhanced Sediment Erosion Rate Flume (SERF), Florida Department of Transportation, Tallahassee, FL.

Crowley, R.W., Robeck, C., Thieke, R.J., 2014b. Computational Modeling of Bed Material Shear Stresses in Piston-Type Erosion Rate Testing Devices. Journal of Hydraulic Engineering, 140(1): 24-34. DOI:10.1061/(ASCE)HY.1943-7900.0000797

FDOT, 2005. FDOT Bridge Scour Manual. Florida Department of Transportation (FDOT), Tallahassee, FL.

Fredsoe, J., 1984. Turbulent Boundary Layer in Wave-Current Motion. J. Hydraulic Engineering, 110(8): 1103-1120.

Le Méhauté, B., 1976. An Introduction to Hydrodynamics and Water Waves. Springer.

Oh, S., Briaud, J.-L., Chang, K., Chen, H., 2010. Maximum Abutment Scour Depth in Cohesive Soils, Fifth International Conference on Scour and Erosion. American Society of Civil Engineers, San Fransisco, CA.

Sheppard, D.M., 2004. An Overlooked Local Sediment Scour Mechanism, Transportation Research Record 1890. Transportation Research Board, Washington, DC.

Sheppard, D.M., Miller, B.W., 2006. Live Bed Local Pier Scour Experiments. Journal of Hydraulic Engineering, 132(7): 635-642. DOI:10.1061//ASCE/0733-9429/2006/132:7/635.

Sheppard, D.M., Odeh, M., Glasser, T., 2004. Large Scale Clear-Water Local Pier Scour Experiments. Journal of Hydraulic Engineering, 130(10): 957-963. DOI:10.1061/(ASCE)0733-9429(2004)130:10(957).

Shields, A.F., 1936. Application of Similarly Principles and Turbulence Research to Bed-Load Movement, CalTech, Pasadena, CA.

Siemens, 2020. Simcenter Star-CCM+. Version 15.02.009.

Sumer, B.M., Fredsoe, J., 1998. Wave Scour Around Group of Vertical Piles. Journal of Wateray, Ports, Coastal, and Ocean Engineering, 124(5): 248-256.

Sumer, B.M., Fredsoe, J., 2001. Wave Scour Around a Large Vertical Circular Cylinder. Journal of Waterway, Port, Coastal, and Ocean Engineering, 127: 125-134.

Sumer, B.M., Fredsoe, J., Christiansen, N., 1990. Scour Around Vertical Piles in Waves. Journal of Waterway, Port, Coastal, and Ocean Engineering, 118(1): 15-31.

Sumer, B.M., Fredsoe, J., Christiansen, N., 1992. Scour Around Vertical Pile in Waves. Journal of Waterway, Ports, Coastal, and Ocean Engineering, 118(1): 15-31.

Sumer, B.M. et al., 2013. Backfilling of a Scour Hole around a Pile in Waves and Current. Journal of Waterway, Port, Coastal, and Ocean Engineering, 139: 9-23.